DESIGN FOR HIGH EFFICIENCY OF LOW-PRESSURE AXIAL FANS:
USE OF BLADE SWEEP AND VORTEX DISTRIBUTION

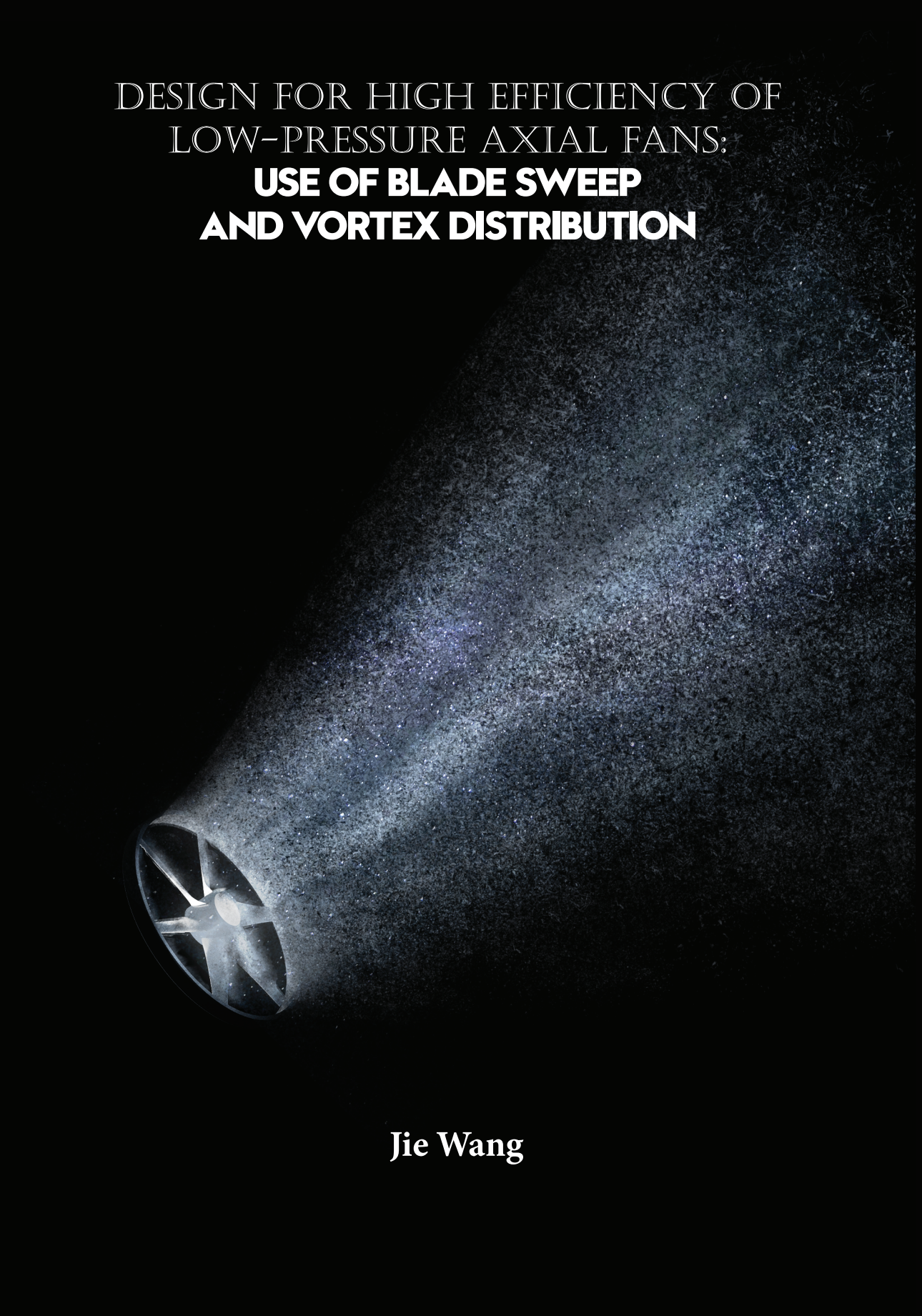

Jie Wang

Design for high efficiency of low-pressure axial fans: Use of blade sweep and vortex distribution

Jie Wang

Design for high efficiency of low-pressure axial fans: Use of blade sweep and vortex distribution

DISSERTATION

to obtain
the degree of doctor at the University of Twente,
on the authority of the rector magnificus,
Prof. dr. ir. A. Veldkamp,
on account of the decision of the Doctorate Board
to be publicly defended
on Wednesday 15 December 2021 at 14.45 hours

by

Jie Wang

born on 7th of August 1993
in Hubei, China

This dissertation has been approved by:

Supervisors:
Prof. dr. ir. C.H. Venner
Dr. ir. N.P. Kruyt

The presented research is carried out in the Engineering Fluid Dynamics group, Faculty of Engineering Technology, University of Twente, The Netherlands.

The research has been financed by the China Scholarship Council (CSC) and Howden Netherlands. The work is supported by NUMECA International.

UNIVERSITY OF TWENTE. Howden

Cover design	:	Chaoying Li
Printed by	:	IPSKAMP Printing
ISBN	:	978-90-365-5299-8
DOI	:	10.3990/1.9789036552998

Graduation Committee

Chair/secretary:	Prof.dr.ir. H.F.J.M. Koopman
Supervisors:	Prof. dr. ir. C.H. Venner Dr. ir. N.P. Kruyt
Committee members:	Prof. dr. A.R. Thornton Prof. Dr.-Ing. Dr. rer. pol. W. Rohlfs Prof. dr. ir. B.J. Boersma J. Vad, Dr. Sc., Dr. habil

Your perceived mediocrity stops you from being excellent.
Never kill another "you" who can make it much better.

To Myself

知行合一

王守仁

Abstract

Rotor-only low-pressure axial fans with small hub-to-tip diameter ratio (*HTR* in short) are widely used in many branches of industry, especially for cooling and ventilation purposes. As energy-related products that account for a significant proportion of the consumption of natural resources and energy, optimization of their aerodynamic performance for high efficiency is important to reduce environmental impact. Differently from low-pressure axial fans with medium to high *HTR*, extensive regions of backflow near the hub are often present downstream of fans with small *HTR*.

In studies of low-pressure axial fans, Computational Fluid Dynamics (CFD) simulations have been frequently employed to analyze in detail the aerodynamic performance and the flow fields inside these machines. For optimization, according to investigations on axial fans with medium to high *HTR*, sweep, dihedral and skew of the blades' stacking line as well as different vortex distribution designs form important methods. However, for fans with small *HTR*, only few studies have been reported in the scientific literature on appropriate CFD simulation strategy, three-dimensional stacking and vortex distribution design method.

The objective of this thesis is to investigate the effects of sweep, dihedral and skew on the aerodynamic performance of low-pressure axial fans with small *HTR* and develop an optimal vortex distribution design method for high efficiency of such fans. CFD simulations are extensively used in these investigations.

Computational Fluid Dynamics Simulation Strategy

Firstly, in order to develop guidelines for obtaining accurate CFD predictions for such fans, validation simulations of a baseline axial fan with small *HTR* have been performed. The experimental and computed aerodynamic performance characteristics have been compared.

These CFD guidelines pay special attention to the trailing edge shape, presence of non-aerodynamically shaped blade sections, tip gap, and employed turbulence model. The results for the fan studied here show that the actual (rounded) trailing edge is necessary; the main blade (without non-aerodynamically shaped blade sections) well represents the aerodynamic performance of the whole fan

blade; it is recommended not to take the tip gap into consideration (in an industrial context) due to the inadequate predictions of its influence on the aerodynamic performance. The use of the Spalart–Allmaras turbulence model is advised for giving better agreement with measurements.

Effects of Sweep, Dihedral and Skew on Aerodynamic Performance

Secondly, investigations on axial fans with medium to high *HTR* have shown that forward sweep of blades can give improved aerodynamic performance, especially for the total-to-total efficiency. Effects of sweep, dihedral and skew in axial and circumferential directions (in forward and backward direction) on the aerodynamic performance of small *HTR* fans are investigated, with a linear stacking line.

The CFD results show that forward sweep and circumferential skew are beneficial for higher total-to-total efficiency and that higher total-to-static efficiency can be obtained by forward dihedral and axial skew. The backward shape variety generally gives negative aerodynamic effects. Forward sweep and circumferential skew shorten the radial migration path, but more flow separation is present near the hub. With forward dihedral and axial skew, the backflow region is reduced in radial size and axial extent, but a more significant hub corner stall region is found. The pressure reduction due to sweep and dihedral is more limited than what could be expected from wing aerodynamics.

Optimal Vortex Distribution Design Method

Finally, the vortex distribution (polynomial in spanwise coordinate) and the *HTR* have been determined by maximizing the total-to-static efficiency of a baseline axial fan with small *HTR*. For free vortex designs, analytical expressions for the maximum total-to-static efficiency and the optimal *HTR* have been formulated. By combining the vortex distribution with a suitable choice for the spanwise lift coefficient distribution, fan blade designs have been established.

The CFD results for these designs show that the free and the polynomial vortex distribution designs satisfy the desired pressure rise, with significantly improved total-to-static and total-to-total efficiency (maximum improvement by 3.9% and 4.6%, respectively).

Flow field analyses show that no flow separation is present in the blade-to-blade plane, except near the hub region. For designs with small *HTR*, some backflow is present downstream of the rotor which affects the flow separation near the hub blade section.

Overall, the investigations in this thesis contribute to better understanding of small *HTR* axial fan aerodynamics. The results can be applied to the design of low-pressure axial fans with high efficiency.

Samenvatting

Lagedruk axiaalventilatoren met uitsluitend een rotor en met een kleine naaftip diameterverhouding (in het Engels afgekort als *HTR*) worden veel gebruikt in diverse industriële sectoren, vooral voor koeling en ventilatie. Als energiegerelateerde producten die veel natuurlijke hulpbronnen en energie vereisen, is optimalisatie van hun aërodynamische prestaties (voor een hoog rendement) belangrijk om de impact op het milieu te verminderen. In tegenstelling tot lagedruk axiaalventilatoren met middelhoge tot hoge *HTR*, zijn bij ventilatoren met kleine *HTR* stroomafwaarts van de ventilator uitgebreide gebieden met terugstroming vaak aanwezig nabij de naaf.

In studies van lagedruk axiale ventilatoren worden“Computational Fluid Dynamics" (CFD) simulaties vaak gebruikt om de aërodynamische prestaties en de stromingsvelden in zulke machines in detail te analyseren. Voor optimalisatie zijn, volgens onderzoeken naar axiaalventilatoren met gemiddelde tot hoge *HTR*, “sweep", “dihedral" en “skew" van de “stacking line" van de bladen en verschillende vortexverdelingen belangrijke methoden. Voor ventilatoren met een kleine *HTR* zijn er echter slechts enkele studies gerapporteerd in de wetenschappelijke literatuur over geschikte CFD-simulatiestrategie, driedimensionale “stacking" van de ventilator bladsecties en de ontwerpmethode gebaseerd op de vortexverdeling.

Het doel van dit proefschrift is om de effecten van “sweep", “dihedral" en “skew" op de aërodynamische prestaties van lagedruk axiaalventilatoren met kleine *HTR* te onderzoeken en om een optimale vortexverdeling ontwerpmethode te ontwikkelen voor een hoog rendement van dergelijke ventilatoren. Bij deze onderzoeken worden CFD-simulaties veelvuldig gebruikt.

Computational Fluid Dynamics-simulatiestrategie

Ten eerste, om richtlijnen te ontwikkelen voor het verkrijgen van nauwkeurige CFD-voorspellingen voor zulke ventilatoren, zijn er validatiesimulaties van een ventilator met kleine *HTR* uitgevoerd. Hierbij zijn de experimentele en met CFD berekende aërodynamische prestaties vergeleken.

Deze richtlijnen besteden speciale aandacht aan de vorm van de achterrand

van het ventilatorblad, de aanwezigheid van niet-aerodynamisch gevormde bladsecties, tipspleet en gebruikt turbulentiemodel. De resultaten voor de hier bestudeerde waaier laten zien dat de daadwerkelijke (afgeronde) achterrand noodzakelijk is; het hoofdblad (zonder niet-aërodynamisch gevormde bladsecties) geeft de aerodynamische prestaties van het gehele ventilatorblad goed weer; het wordt (in een industriële context) aanbevolen om geen rekening te houden met de tipspleet aangezien de invloed daarvan op de aërodynamisch nog niet adequaat wordt voorspeld. Het gebruik van het Spalart-Allmaras-turbulentiemodel wordt aanbevolen om een betere overeenstemming met metingen te krijgen.

Effecten van “sweep", “dihedral" en “skew" op prestaties

Ten tweede hebben onderzoeken aan axiale ventilatoren met gemiddelde tot hoge *HTR* aangetoond dat voorwaartse “sweep" van bladen kan zorgen voor verbeterde aërodynamische prestaties, met name het totaal-naar-totaal rendement. Effecten van “sweep", “dihedral" en “skew" in axiale en omtreksrichtingen (in voorwaartse alswel in achterwaartse richting) op de aërodynamische prestaties van ventilatoren met kleine *HTR* zijn onderzocht, met een lineaire “stacking" lijn voor de bladsecties.

De CFD resultaten laten zien dat voorwaartse “sweep" en “skew" in omtreksrichting gunstig zijn voor een hoger totaal-naar-totaal rendement en dat een hoger totaal-naar-statisch rendement kan worden verkregen met voorwaartse “dihedral" en “skew" in axiale richting. De achterwaartse “skew" variaties geven over het algemeen negatieve aërodynamische effecten. Voorwaartse “sweep" en “skew" in omtreksrichting verkorten het radiale migratiepad van de stroming, maar er is meer stromingsloslating nabij de naaf. Met voorwaartse “dihedral" en axiale “skew" wordt het terugstroomgebied kleiner qua radiale en axiale afmeting, maar er wordt een significanter loslatingsgebied gevonden bij de naaf. De drukvermindering als gevolg van “sweep" en “dihedral" is kleiner dan wat wordt verwacht op basis van vleugelaërodynamica.

Optimale Vortexverdeling Ontwerpmethode

Ten slotte zijn de vortexverdeling (als polynoom in de coordinaat in de spanrichting) en de *HTR* bepaald door het totaal-naar-statisch rendement van een referentie axiaalventilator met kleine *HTR* te maximaliseren. Voor vrije-vortex ontwerpen zijn analytische uitdrukkingen geformuleerd voor het maximale totaal-naar-statisch rendement en de optimale *HTR*. Door de vortexverdeling te combineren met een geschikte keuze voor de verdeling (in spanrichting) van de liftcoëfficiënt zijn ventilatorblad ontwerpen verkregen.

De CFD-resultaten voor deze ontwerpen laten zien dat de ontwerpen gebaseerd op vrije en polynoom vortexverdelingen voldoen aan de gewenste drukstijging, met aanzienlijk verbeterde totaal-naar-statisch en totaal-naar-totaal rendementen (maximale verbetering met respectievelijk 3.9% en 4.6%).

Analyses van de stromingsvelden laten zien dat er geen stromingsloslating aanwezig is in het blad-naar-blad vlak, behalve in de buurt van de naaf. Voor ontwerpen met een kleine *HTR* is er enige terugstroming stroomafwaarts van de rotor die de stromingsloslating nabij de naaf beïnvloedt.

In het algemeen draagt het onderzoek in dit proefschrift bij aan een beter begrip van de aërodynamica van axiaalventilatoren met kleine *HTR*. De resultaten kunnen worden toegepast voor het ontwerpen van lagedruk axiaalventilatoren met een hoog rendement.

Contents

Chapter 1

Introduction

In this chapter, the research background of the current study is introduced in Sec. 1.1. Parameters for evaluating the aerodynamic performance of axial fans are described in Sec. 1.2. The research objectives and outline of this thesis are introduced in Sec. 1.3 and 1.4.

1.1 Research Background

All investigations in this research focus on low pressure axial fans, a type of turbomachine that is widely used in many industrial and domestic application. Turbomachines are devices in which energy is transferred either to, or from, a continuously flowing fluid by the dynamic action of moving blade rows. Examples are (water or wind) turbines for power generation, and pumps and compressors for increasing pressure of water or gases for different purposes.

Among the turbomachine family, fans are probably most familiar, since they are widely applied in many parts of modern life. For example, table or floor fans for personal thermal comfort, ducted fans for HVAC (Heating, Ventilation, and Air Conditioning) systems and cooling fans in various industrial applications.

Fans are used to generate fluid (air in general) flow with pressure rise. The main types are centrifugal and axial fans. Two single-stage fans are shown in Fig. 1.1(a) and (b). Centrifugal fans force fluid to flow in the axial direction (parallel to rotating shaft) at inlet and flow out in radial direction, while in axial fans, fluid moves in and out parallel to the rotating shaft. Compared with axial fans, centrifugal fans in general have a smaller inlet area and a higher rotational speed and are able to generate a high pressure rise at a low flow rate. As for axial fans, the inlet and outlet area are generally the same, so axial fans are usually used for low pressure rise at large flow rates.

Axial fans that rotate in an unrestricted air space are called *free fans* (Fig. 1.2(a)). In domestic uses or industrial applications, an enclosing duct constrains the fluid

1

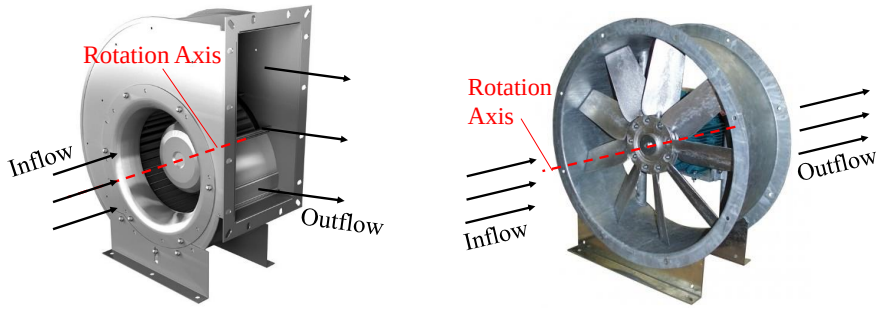

(a) (b)

Figure 1.1: Examples of (a) Centrifugal fan [1] and (b) Axial fan [2]

to enter and leave the fan unit in axial direction. Such fans are called *ducted fans* (Fig. 1.2(b)).

(a) (b)

Figure 1.2: Examples of (a) Free Fan [3] and (b) Ducted Fan [4]

In view of the pressure rise, a single stage axial fan can be classified into low-pressure and high-pressure group. It should be noted that the boundary between the low and the high pressure axial fans is rather vague. In general, the pressure rise from a low-pressure axial fan is smaller than 490Pa and for a high-pressure axial fan the upper limit is 4900Pa. Compressors or multistage axial fans are applied to obtain higher pressure rises. For low-pressure axial fans, the pressure rise is generated with large flow rates, therefore it is often applied in domestic ventilation and air cooling systems.

Regarded as energy-related products, turbomachines account for a large proportion of the consumption of natural resources and energy. Improving efficiency and saving energy are always important research topics. In 2009 [5], the European Commission has published directives to establish a framework for the setting of eco-design requirements for energy-related products. These form a strong incentive for innovation in the design of turbomachines to meet the challenge of obtaining machines with high efficiency. In 2011 [6], the requirements for eco-design were converted into specific requirements for fans.

The company Howden is an internationally leading manufacturer of many types of industrial systems. Howden Netherlands (located in Hengelo, The Netherlands) is worldwide supplier of industrial cooling fans for cooling towers, air-cooled steam condensers, and air-cooled heat exchangers used in a wide range of industrial applications. Produced by Howden, the low-pressure axial fan (shown in Fig. 1.3 (a)) is typically used in air cooling systems (shown in Fig. 1.3 (b)) and has been chosen as a baseline fan in the investigations for higher efficiency in this study.

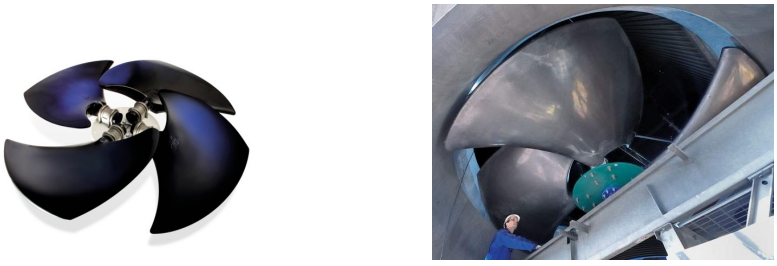

(a) (b)

Figure 1.3: Examples: (a) Howden Fan and (b) Fan in Cooling System [7]

1.2 Aerodynamic Performance of Axial Fan

During the working process of axial fans, the fluid medium is usually air with density ρ (in kg/m^3) and volumetric flowrate Q (in m^3/s) being constant for effectively incompressible flow through the fan. In the required working state, blades rotate at rotational speed Ω (in rad/s). The torque T (in $N \cdot m$) is transferred from the shaft to the fan blades, with input shaft power $P_{\text{shaft}} = \Omega \cdot T$. With energy being transferred to the flow, the velocity, the static and the total pressure will change from inlet to outlet. The total-to-static pressure rise (also called Fan Static

Pressure) p_{fs} and the total-to-total pressure rise (also called Fan Pressure) p_{f} are defined by:

$$p_{\mathrm{fs}} = p_2 - p_{01} \qquad p_{\mathrm{f}} = p_{02} - p_{01} \tag{1.1}$$

where p_{02} and p_2 are the average total and static pressure at the outlet of the fan respectively, and p_{01} is the average total pressure at the inlet of the fan. The total pressure can be calculated by $p_0 = p + \frac{1}{2}\rho v^2$, where v is the magnitude of the absolute velocity vector.

The shaft transfers torque from the motor to the rotor blades and energy is transferred to the fluid by the interaction between the blade surface and the fluid. The efficiency is evaluated by the ratio between power transferred to the fluid and the input power. The total-to-static and the total-to-total efficiency η_{ts} and η_{tt} are defined by:

$$\eta_{\mathrm{ts}} = \frac{Q \cdot p_{\mathrm{fs}}}{P_{\mathrm{shaft}}} \qquad \eta_{\mathrm{tt}} = \frac{Q \cdot p_{\mathrm{f}}}{P_{\mathrm{shaft}}} \tag{1.2}$$

Similitude considerations of flow in turbomachine make it possible to apply independent dimensionless coefficients for design, comparison and assessment of axial fans [8]. The dimensionless performance parameters are

$$\varphi = \frac{Q}{\frac{\pi}{8}\Omega D_{\mathrm{fan}}^3} \qquad \psi = \frac{p_{\mathrm{fs}}}{\frac{1}{8}\rho\Omega^2 D_{\mathrm{fan}}^2} \qquad \psi_{\mathrm{tt}} = \frac{p_{\mathrm{f}}}{\frac{1}{8}\rho\Omega^2 D_{\mathrm{fan}}^2} \qquad \lambda = \frac{P_{\mathrm{shaft}}}{\frac{1}{32}\rho\Omega^3 D_{\mathrm{fan}}^5} \tag{1.3}$$

Here φ is the flow coefficient, ψ is the pressure coefficient, ψ_{tt} is the total pressure coefficient and λ is the power coefficient. D_{fan} is the fan outer diameter (i.e. the tip diameter of the fan blades).

The Reynolds number Re and Mach number Ma based on tip velocity are given by:

$$\mathrm{Re} = \frac{\Omega D_{\mathrm{fan}}^2}{4\nu} \qquad \mathrm{Ma} = \frac{\Omega D_{\mathrm{fan}}}{2a} \tag{1.4}$$

where ν and a are the kinematic viscosity and the speed of sound of the gas, respectively. The Reynolds number physically represents the ratio between the inertial forces and viscous forces within fluid flows. It has been found that when $\mathrm{Re} > 2 \times 10^5$, the influence of Re on the performance of turbomachine is small [9]. When the Mach number $\mathrm{Ma} < 0.3$, fluid flow can be treated as effectively incompressible flow with constant density. In the current study, Re is larger than 2×10^5 and Ma is smaller than 0.3, thus the influences of Re and Ma are considered to be secondary.

The hub-to-tip diameter ratio κ is defined by

$$\kappa = \frac{D_{\mathrm{hub}}}{D_{\mathrm{fan}}} \tag{1.5}$$

where D_{hub} is the hub diameter.

The fan aerodynamic performance is typically presented as performance curves: $Q-p_{\text{fs}}$, $Q-\eta_{\text{ts}}$ and $Q-\eta_{\text{tt}}$ in dimensional form; or $\varphi-\psi$, $\varphi-\eta_{\text{ts}}$ and $\varphi-\eta_{\text{tt}}$ in dimensionless form, so that these can be used to predict fan performance at different scales and operating conditions. In the current study, the dimensionless form is mostly used. Examples of fan performance curves are shown in Fig. 1.4(a), (b) and (c).

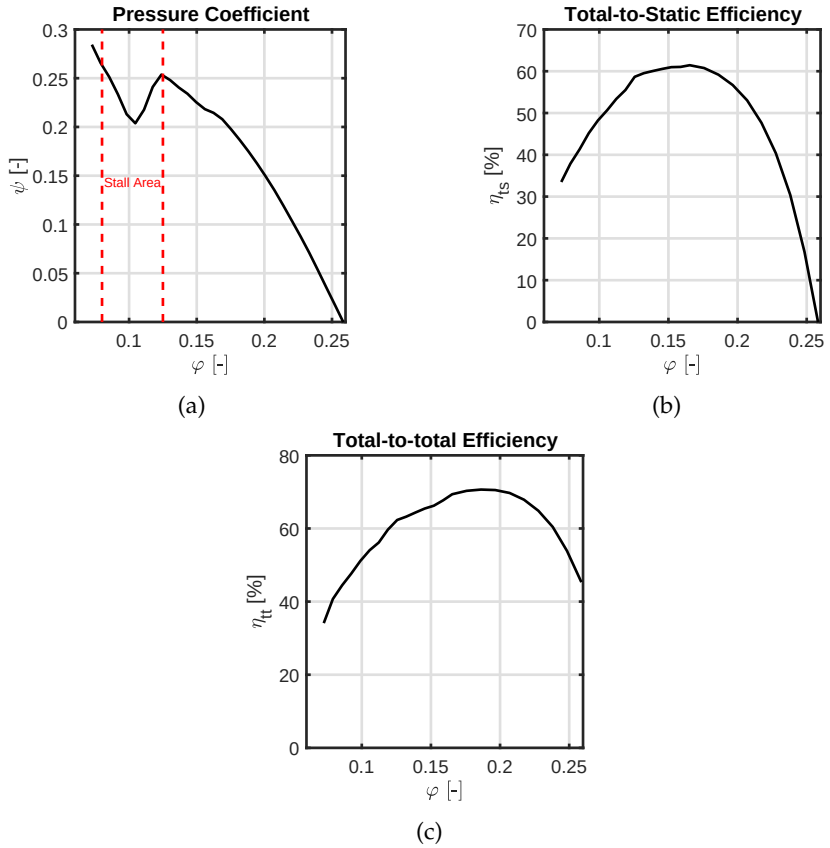

Figure 1.4: Example of Fan Performance Curve: (a) φ - ψ (Stall area is indicated between red dash lines), (b) φ - η_{ts} and (c) φ - η_{tt}.

In Fig. 1.4(a), the stall area is indicated between the red dash lines, during which the fan static pressure firstly drops, and then increases due to the flow

separations on the suction side of blade surface at low flow rates.

Comparing Fig. 1.4(b) and (c), the total-to-static efficiency η_{ts} drops earlier than the total-to-total efficiency η_{tt} and η_{tt} has a higher peak value and wider steady range. The differences between η_{ts} and η_{tt} originate from the kinetic energy of the absolute velocity downstream of fan blades. According to specific configurations, when outlet guide vanes are present or the fan unit is connected with a long outlet duct, η_{tt} is often considered; when there are no outlet guide vanes (rotor-only case) and the fan exhausts air to the open atmosphere, the kinetic energy of the absolute velocity is considered as losses, and η_{ts} is used.

1.3 Research Objectives

The design of an axial fan should generate the required pressure rise at a certain flow rate. Its working process naturally involves the interaction between the rotating solid machine and the fluid flow with complicated three-dimensional flow phenomena and forces acting on blade rows, which makes the research area of axial fans very extensive. Among all research besides mechanical aspects, the aerodynamic design is very important.

In the design stage, flows are often treated based on two-dimensional cascade theory. However, in reality the flows are three-dimensional and separation related with stall, re-circulation and vortices occur, which are causes of possible noise and losses, also causing deviations between the realized performance and design expectation.

With respect to the fan blades, high-speed rotation and pressure change or fluctuation on the blade surface may cause vibrations despite the manufacturing process, which definitely affect the stability of the rotor blades and other related equipment. Therefore, with good manufacturing quality, avoiding high magnitude pressure changes and fluctuations on the blade surface is important.

An aerodynamic design can be evaluated by the total-to-total or total-to-static pressure rise and efficiency. Once the required pressure rise is satisfied, a higher efficiency becomes the objective. The improvement of efficiency for a given axial fan can be obtained by variation of the configuration or by an optimized vortex distribution (also called “blade loading") design.

For the configuration, using a rotor-only fan as example, inlet and outlet guide vanes are usually considered when there is no constraint in cost and spatial requirements; when the budget or space is limited, local blade variations, for example sweep, dihedral or skew, can be considered in baseline blades for possible advantages.

For an optimized design, modifying the vortex distributions along the spanwise locations with fixed configurations to obtain improved aerodynamic design can contribute to higher efficiency.

In order to contribute to the further advancement of engineering science, the current research project studies methods for designing low-pressure axial fan for high efficiency. The project is as cooperation between the Engineering Fluid Dynamic Group at the University of Twente and Howden Netherlands. According to recent developments in axial fan design, swept blade and spanwise vortex distribution are studied parametrically to investigate methods to obtain high efficiency of a low-pressure axial fan.

In order to avoid unnecessary costs of measurements during the trial-and-error design phase, Computational Fluid Dynamics (CFD in short) simulations are carried out to predict the performance of axial fans with new blade shapes and vortex distributions. FineTurbo from NUMECA International is used as (commercial) software for CFD simulations.

It should be noted that the hub-to-tip diameter ratio of the investigated baseline fan is much smaller than for other axial fans reported in scientific literature and the literature studying the axial fans with such small hub-to-tip diameter ratio is quite limited. Hence, the current study can contribute to a better understanding of the aerodynamic performance of axial fans with small hub-to-tip diameter ratio.

Specifically, the objectives of this thesis on the aerodynamics of the low-pressure axial fans with small hub-to-tip diameter ratio are:

- Study on validation of a CFD simulation strategy.
- Study the effects of sweep, dihedral and skew on the aerodynamic performance.
- Study of the optimal vortex distribution design method for high efficiency.

1.4 Outline

The ultimate objective of this dissertation is to present research processes and results for improving the efficiency of low pressure axial fans with small hub-to-tip diameter ratio. The fundamental theory of axial fan design and methodology are given in Chapter 2. The literature review about design of axial fans is given in Chapter 3. Detailed geometrical information and measurements of the investigated baseline fan are described in Chapter 4. The background for CFD simulations is introduced in Chapter 5. The main results of the validation research, sweep research and vortex distribution research are given in Chapters 6, 7 and 8 respectively. Finally, conclusions and recommendations are described in Chapter 9.

1

Chapter 2

Axial Fan Design Theory

In this chapter, the design theory of axial fans is introduced. The design theory of axial fans has experienced a long history of development, since they are widely used for many purposes. During the development, good designs have been collected and reported in the so-called Cordier diagram [10] as introduced in Sec. 2.1, which is still an important reference for a pump and fan designer in the preliminary design phase. The explicit design theory of axial fans is usually following from aerodynamic theory. A historical overview of aerodynamic design of axial fans is reported in Ref. [11]. In chronological order, Euler's pump and turbine equation, actuator-disk (or axial momentum) theory, blade element theory and vortex distribution design theory form milestones in the design theory development. These are introduced in Sec. 2.2 to 2.7. It should be noted that the design theories of axial fans are based on two-dimensional consideration, the radial velocity is assumed to be neglected. The development of aircraft has introduced the concept of "sweep" into the design of axial fans. Details of sweep design are described in Sec. 2.8.

It should be noted that the introduced design theories in this chapter are based on ideal case. In the design phase, the hydraulic efficiency η_h should be considered and the details are reported in Chapter 7 and 8.

2.1 Diagram for Optimum Design

In 1953, Cordier [10] presented a diagram showing the performance of "optimum" designed fans, pumps and turbines in terms of specific speed σ and specific diameter δ defined by:

$$\sigma = \frac{n}{(2\pi^2)^{-1/4}\left(\frac{p_\mathrm{f}}{\rho}\right)Q^{-1/2}} \qquad \delta = \frac{D_\mathrm{fan}}{\left(\frac{8}{\pi^2}\right)^{1/4}\left(\frac{p_\mathrm{f}}{\rho}\right)^{-1/4}Q^{1/2}}. \tag{2.1}$$

Where n is the fan rotation speed (in rps), Q and p_f are the volumetric flow rate and the total-to-total pressure rise at the duty point (normally the best efficiency point).

In terms of the flow coefficient φ and the total pressure coefficient ψ_{tt} (given in Eq. (1.3)), σ and δ can be expressed by

$$\sigma = \varphi^{1/2}\psi_{tt}^{-3/4} \qquad \delta = \varphi^{-1/2}\psi_{tt}^{1/4} \tag{2.2}$$

For σ defined at the duty point of a turbomachine, it is of great importance to the selection of the machine type suitable for a specific duty point (expressed in term of σ), as shown in Fig. 2.1.

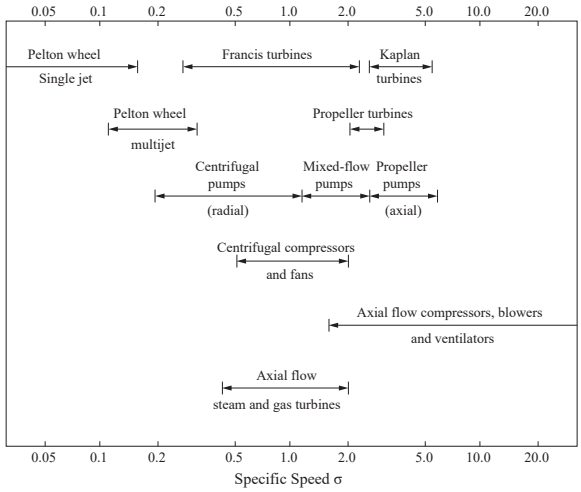

Figure 2.1: Range of Specific Speeds for Various Types of Turbomachine [12]

The original Cordier Diagram is shown in Fig. 2.2, where fans are located at high σ and low δ. As a milestone in turbomachine design, this diagram was primarily used for identifying the optimum operation range and the type of machine. With design requirements like flow-rate and pressure rise and other geometry information, φ and ψ_{tt} can be calculated to give the values of σ and δ. The latter two can be located in the Cordier Diagram to determine a preliminary design plan for high efficiency.

Nowdays, a practical use of this diagram is based on a curve that interpolates the data in the diagram, the so-called Cordier Curve, as shown in Fig. 2.3. The Cordier Curve means that for given design requirements (flow-rate and pressure rise), there is an optimum relation between diameter and rotation speed to satisfy

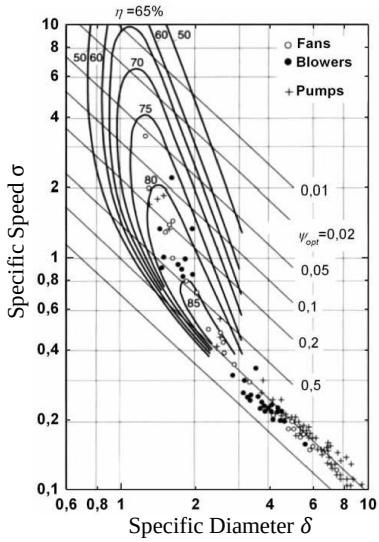

Figure 2.2: Original Cordier Diagram (adapted from Ref. [10])

the required design duty with high efficiency with respect to all other possible designs [11]. Therefore, it should be noted that the curve represents a mean curve of scattered data shown in the Cordier Diagram. It represents a fairly broad range on either side of the line [9].

As Bamberger and Carolus [13] reported, Pelz and Metzler [14] in 2012 derived an approximation to the Cordier Curve:

$$\sigma_{\text{opt}} = \frac{1}{2\bar{\varphi}\delta_{\text{opt}}^3} + \sqrt{\left(\frac{1}{2\bar{\varphi}\delta_{\text{opt}}^3}\right)^2 + \frac{1}{2\overline{\psi_{\text{tt}}}\delta_{\text{opt}}^2}} \tag{2.3}$$

Pelz recommended $\bar{\varphi} = 0.25$ and $\overline{\psi_{\text{tt}}} = 1$ as adequate choices [13, 14].

For fans with small hub-to-tip diameter ratio, backflow behind the fan may occur near the hub. The Strscheletzky criteria [8] (shown in Fig. 2.4) give relations between the hub-to-tip diameter ratio κ and the ideal design point $\varphi/\psi_{\text{tt.th}}$ such that regions with backflow (or “dead flow regions") may occur.

By investigating the Strscheletzky conditions, Marcinowski related the optimum hub-to-tip ratio κ and the ideal design point by [11, 15]:

$$\frac{\varphi}{\psi_{\text{tt.th}}} = \frac{1-\kappa^2}{2\kappa} \tag{2.4}$$

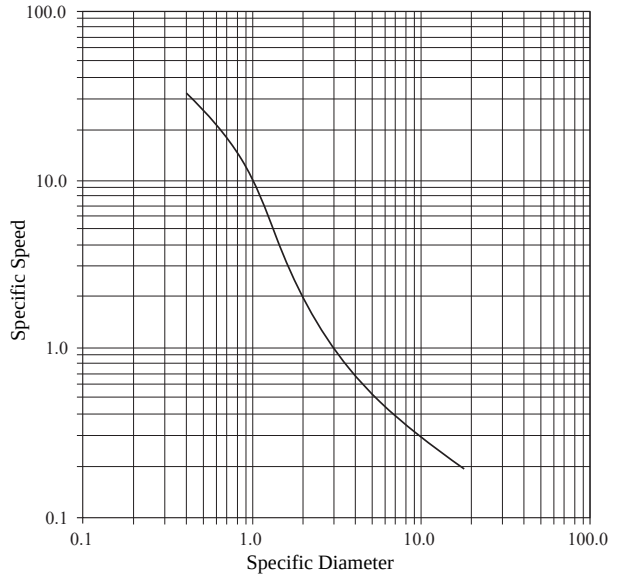

Figure 2.3: Cordier Curve (adapted from Ref. [9])

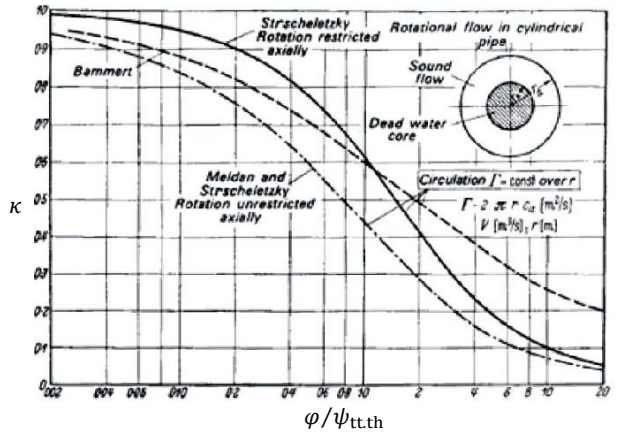

Figure 2.4: Strscheletzky Boundary Layer Conditions Criteria for the Hub Dead Space (adapted from Ref. [8])

$$\frac{\varphi}{\psi_{\text{tt.th}}} = \frac{1}{2}\sqrt{\frac{1}{2\kappa^2}(1-\kappa^2)^2 - (1-\kappa^2)\ln(\kappa^{-1})} \tag{2.5}$$

Eq. (2.4) is for axially restricted cases (like an axial fan with outlet guide vanes) and Eq. (2.5) is for axially unrestricted cases (for example the rotor-only axial fan). These two equations are of importance; Castegnaro states in Ref. [11]: *"According to the author's best knowledge, Marcinowski's approach is still the only analytic method that allows a computation of the hub-to-tip ratio"*.

For the baseline Howden fan in the current research, the hub-to-tip diameter ratio $\kappa = 0.14$ and the operation point is $\varphi/\psi_{\text{tt}} = 1.11$. Based on Eq. (2.5), the ideal design point $\varphi/\psi_{\text{tt}} = 2.38$, according to the Strscheletzky condition for axially unrestricted cases, backflow is expected for baseline fan.

2.2 Velocity Triangle

In axial fans, the blades rotate around the axis of rotation with angular speed $\vec{\Omega}$. This is a rotating system with axially-symmetric hub and casing. Hence, a cylindrical coordinate system is convenient to use with components in radial, circumferential and axial direction, represented by r, θ and z.

The meridional plane is the $r-z$ view, an example of meridional plane is shown in Fig. 2.5, where spanwise blade sections are indicated by red dotted lines. A three-dimensional axial fan blade can be regarded as "stacking" of blade sections at different radial (spanwise) locations. Each of such sections is a blade element and has a shape of an airfoil.

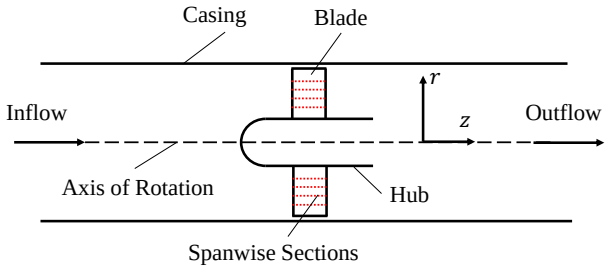

Figure 2.5: Example of the Meridional Plane: Red dotted lines indicate the blade sections in spanwise direction.

The blade-to-blade plane is the cylindrical surface in the $r \cdot \theta - z$ view and in this view, the velocities considered are the absolute flow velocity $\vec{v}$, the blade velocity $\vec{u} = \vec{\Omega} \times \vec{r}$ and the relative flow velocity $\vec{w}$. The relationship between the

absolute and the relative velocity is obtained geometrically from the so-called “velocity triangle", this is a fundamental concept in turbomachine.

An example of the inlet velocity triangle in the blade to blade view and one corresponding blade element of a rotor-only axial fan blade is shown in Fig. 2.6.

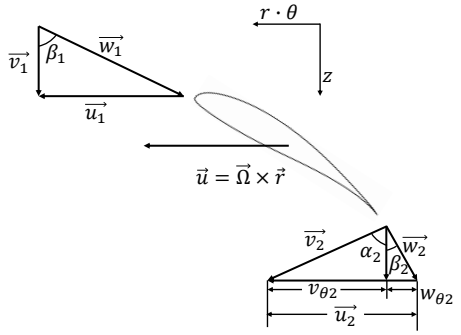

Figure 2.6: Velocity Triangle for a Rotating Airfoil; $\vec{v}$,$\vec{u}$,$\vec{w}$ denote the absolute, blade and relative velocities, β and α denote the relative and absolute flow angles (relative to the axial, z-direction), v_θ and w_θ denote the circumferential component of absolute and relative velocities, “1" and “2" denote the inlet and outlet.

2.3 Euler’s Pump and Turbine Equation

As the most fundamental equation in the turbomachine field, the Euler pump and turbine equation has been formulated in the middle of 18th century. It gives a relationship between the torque T of the rotating shaft transmitted to (or from) the rotor and the angular momentum change of the fluid passing through the rotor [9]:

For pumps/fans:

$$T = \rho \cdot Q(r_2 v_{\theta 2} - r_1 v_{\theta 1}) \tag{2.6}$$

For turbines:

$$T = \rho \cdot Q(r_1 v_{\theta 1} - r_2 v_{\theta 2}) \tag{2.7}$$

Here ρ is the density of fluid, Q is the volumetric flow-rate, r is the radius, v_θ is the circumferential component of the absolute velocity; “1" and “2" indicate the inlet and outlet of the rotor, respectively.

Axial fans transfer energy to fluid flows, and hence Euler’s pump equation is employed. The power transferred by the rotor is:

$$P_{\text{shaft}} = \Omega T = \Omega\rho \cdot Q(r_2 v_{\theta 2} - r_1 v_{\theta 1}) \tag{2.8}$$

with $\Omega r = u$, the specific work W, defined by $P_{\text{shaft}} = \dot{m}W$ ($\dot{m}$ is the mass-flow rate), is given by

$$W = u_2 v_{\theta 2} - u_1 v_{\theta 1} \tag{2.9}$$

In the ideal case, a frictionless flow is considered, and the ideal total pressure rise $p_{\text{f.th}}$ of a fan is given as

$$p_{\text{f.th}} = \frac{\Omega T}{Q} = \rho(u_2 v_{\theta 2} - u_1 v_{\theta 1}) \tag{2.10}$$

When additionally there is no pre-swirl at the inlet ($v_{\theta 1} = 0$), the total pressure rise can be expressed by:

$$p_{\text{f.th}} = \rho u_2 v_{\theta 2} \tag{2.11}$$

Eq. (2.11) is fundamental equation for the design of (single-stage) axial fans.

With $u_2 = \Omega r_2$, $p_{\text{f.th}} = \rho\Omega(r_2 v_{\theta 2})$, here $r_2 v_{\theta 2}$ is called the “vortex distribution" (or “swirl distribution", “blade loading") and is important in design methods.

2.4 Actuator-disk Theory

The actuator-disk theory is also called axial momentum theory and possibly forms the first aerodynamic theory that can guide the design of axial fans [11]. This one-dimensional model has originally been applied to propeller design. As shown in Fig. 2.7, the propeller is modelled as an actuator disk that accelerates the flow with velocity increment Δv at the outlet of the disk and $2\Delta v$ downstream in axial direction; a pressure rise Δp is also created.

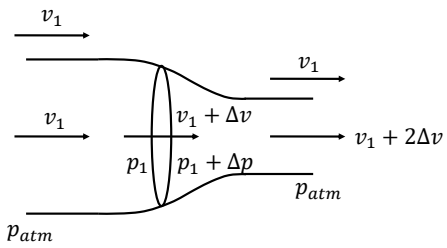

Figure 2.7: Actuator Disk Theory

According to the continuity equation, the flow rate is the same at inlet and outlet, and equals $\rho\pi R^2(v_1+\Delta v)$ with R the radius of the actuator disk. The axial thrust F_a is the change in momentum per unit time and the torque T can be calculated with the known rotational speed [16]:

$$\begin{aligned} F_a &= \rho\pi R^2(v_1+\Delta v)\cdot 2\Delta v \\ \Omega T &= F_a(v_1+\Delta v) \end{aligned} \tag{2.12}$$

This theory provides a way to estimate the overall performance of a propeller for given working conditions, but it is too crude for rotor geometry design, since no information about the blades is provided [11, 17]. Therefore, in order to obtain the blade geometry, blade element theory is quite important for axial fan design.

2.5 Blade Element Theory

The blade element theory was firstly introduced by Drzewiecki in 1892 to consider the blade as a combination of many small adjacent elements [11, 18]. On the cylindrical surface inside an axial fan rotor, the basic element of a rotor blade at different spanwise location is present as an airfoil. An example of an airfoil is shown in Fig. 2.8.

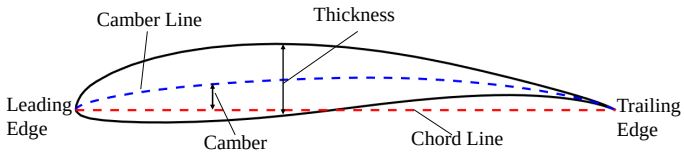

Figure 2.8: Airfoil Example and Basic Parameters

Basic parameters of an airfoil are:

1. Leading edge: The front of airfoil.
2. Trailing edge: The back of airfoil.
3. Chord line: The straight line connecting leading and trailing edge (Red dashed line in Fig. 2.8).
4. Chord length: The length of chord line.
5. Thickness: The distance between upper and lower surfaces.
6. Camber line: The curve connecting the points that lie halfway between the upper and lower surfaces. (Blue dashed line in Fig. 2.8)

7. Camber: The distance between camber line and chord line.

When a fluid flow passes the airfoil, a force is exerted on the surface. With known relative inflow direction, lift and drag are the resultant forces which are of high importance. The lift force is the component of the force that is perpendicular to the incoming flow direction, the drag force is the component of the force parallel to the flow direction.

An example of an isolated airfoil in a flow is shown in Fig. 2.9. The angle of attack α is the angle between the chord line and the vector representing the relative inflow. In airfoil theory, the lift L and drag D force per unit span length

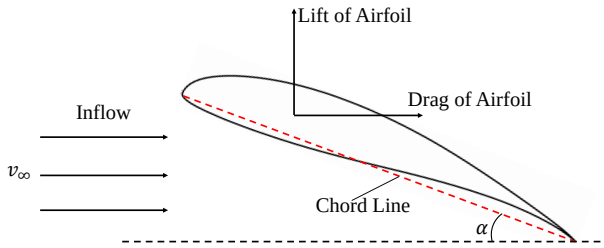

Figure 2.9: Airfoil in Flow Stream: Lift and drag direction and angle of attack α; v_∞ is velocity far upstream.

are expressed by:

$$L = C_l \frac{\rho}{2} v_\infty^2 l \qquad D = C_d \frac{\rho}{2} v_\infty^2 l \tag{2.13}$$

Here C_l and C_d are the lift and drag coefficients obtained, mainly from experiments or numerical calculation (like XFoil [19]). These are functions of the attack angle α (and of the Reynolds number, to a lesser extent). v_∞ is the inflow velocity far upstream, l is the chord length.

2.6 Cascade Analysis Theory

The axial fan blades at each spanwise location are generally not isolated airfoils, but work together. Based on such a consideration, the cascade analysis has been developed.

On a two-dimensional stream surface of axial fans, an isolated airfoil is a part of cascade [9] with identical blade sections nearby, the analysis and design are based on the cascade theory with assumption that the flow fields in adjacent channel are identical. An example of a cascade is shown in Fig. 2.10.

X and Y are forces in axial and circumferential direction exerted (per unit length) by the blade on the fluid; equal but opposite to the force exerted by the

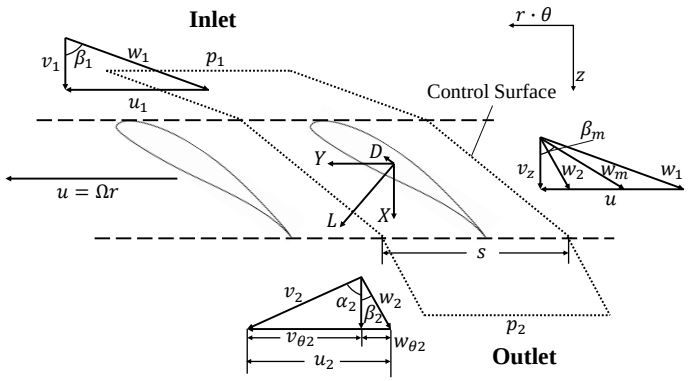

Figure 2.10: Example of Velocity Trangles and Forces in a Blade Cascade

fluid on the blade. The velocity and force calculation are done for the control surface surrounded by the short dashed line, including the blade section and its upstream and downstream boundaries. The static pressure at inlet and outlet of the control surface are denoted by p_1 and p_2. The pitch of the control surface is $s = 2\pi r/Z$, with Z as blade number. It should be noted that no pre-swirl is assumed at the inlet and that the fluid flow in a rotor-only axial fan is assumed to be steady and uniform at the inlet and outlet. Due to the low Mach number, the flow is considered to be incompressible.

The continuity equation gives:

$$v_1 = v_{z1} = v_{z2} = v_2 \cos \alpha_2 \tag{2.14}$$

Here v_z is the constant axial velocity, α_2 is the angle between the absolute velocity and the axial velocity at the outlet. The momentum equation applied in the axial and circumferential directions give:

$$X = (p_2 - p_1)s \qquad Y = \rho v_z s v_{\theta 2} \tag{2.15}$$

The relative mean flow angle β_m is defined by

$$\tan \beta_m = \frac{1}{2}(\tan \beta_1 + \tan \beta_2) \tag{2.16}$$

The angle β_m indicates the direction that the drag force D acts in and that the lift force L acts perpendicular to, so that:

$$Y = D \sin \beta_m + L \cos \beta_m \tag{2.17}$$

Together with Eq. (2.13), the relationship between lift, drag coefficients and flow angles is established [9]:

$$C_l = 2\frac{s}{l}\cos\beta_m(\tan\beta_1 - \tan\beta_2) - C_d\tan\beta_m \tag{2.18}$$

It should be noted that, Turner [20] suggested in 1966 to use cascade data rather than the isolated airfoil data in cascade analysis, with the consideration of multiblade interference, although most axial fans are designed based on isolated airfoil data.

When airfoils are set quite close to each other in the cascade plane, there is mutual interaction of the flow fields around them. This may result in a different slope of the lift curve than in a single airfoil and decrease the maximum lift coefficient [21]. Therefore, use of isolated blade element theory only is not sufficient for axial fans' design.

Blade solidity, considered to determine the choice of the appropriate design method, is defined by the ratio of blade chord to the pitch between adjacent blade sections at the same spanwise location: l/s. When the solidity is larger than 1, aerodynamic interference within the cascade section occurs and usually results in a marked reduction in lift for a given blade angle of attack [21],.

Attempts have been made to extend the applicability of isolated blade element theory by including an interference factor to the lift curve, however, these methods fail to produce consistent results [21]. The cascade data can be obtained experimentally from two-dimensional cascade wind tunnels or CFD simulations like MISES [22, 23]. However, compared with isolated airfoil data, the amount of cascade database data is limited.

With respect to the choice of the appropriate design method, some suggestions are given by Wallis [21]. i. For the application of isolated blade element method, the maximum solidity is recommended as 0.8; ii. When the solidity is larger than 1, the cascade method rather than the isolated blade element method should be considered; iii. The cascade method can not be used for a solidity smaller than 0.6. Besides these recommendations, the product of the lift coefficient and solidity can also be employed for choosing the design method. Some favorable solidity values related with explicit flow angles have been discussed by Zweifel as reference for axial fan designs [8]. More detailed introductions of cascade test facility, cascade performances of turbine and compressor and their correlations have also been reported in book by Dixon [9].

For the baseline rotor-only axial fan in the current study, the maximum solidity is 0.88 at the hub, therefore, the blade element method is sufficient and the cascade data are not employed. However, for optimal designs in the current study, due to small hub-to-tip diameter ratio κ, the solidity near the hub may exceed unit, the interference effects are discussed in detail in Chapter 8.

2.7 Radial Equilibrium Theory and Vortex Distribution

With no radial velocity being considered, both blade element theory and cascade theory are based on two-dimensional assumption. Such an assumption is reasonable for axial fans with large hub-to-tip ratio ($\kappa \geq 0.8$), while for smaller hub-to-tip ratios, radial flow may be appreciable and result in redistribution of the velocity profile (and the flow angle). The imbalance between centrifugal forces exerted on the fluid and radial pressure distribution is responsible for the radial flow [9]. However, after sufficient fluid is transported radially, a restored balance results in equilibrium without radial flow; axisymmetric streamlines lie in cylindrical annular surfaces again, such a flow is called a radial equilibrium flow.

The radial equilibrium theory assumes that all possible radial flow is completed within the blade rows, and that the flow outside the row is in radial equilibrium, this means that the flows upstream and downstream of the axial fan rotor can still be described by two-dimensional methods when satisfying radial equilibrium theory.

With the idea that pressure forces balance centrifugal forces, the equation of radial equilibrium theory is expressed by [9]:

$$\frac{1}{\rho}\frac{dp}{dr} = \frac{v_\theta^2}{r} \tag{2.19}$$

Once the circumferential velocity v_θ and density ρ are known as function of the radius, the static pressure distribution in spanwise direction can be obtained.

In rotor-only axial fans, the flow downstream of the blade conforms to radial equilibrium and is incompressible.

Differentiation of $p_{02} = p_2 + \frac{1}{2}\rho(v_{z2}^2 + v_{\theta 2}^2)$ with respect to radial position r in combination with Eq. (2.19) gives:

$$\frac{1}{\rho}\frac{dp_{02}}{dr} = v_{z2}\frac{dv_{z2}}{dr} + \frac{v_{\theta 2}}{r}\frac{d}{dr}(r\,v_{\theta 2}) \tag{2.20}$$

Combining Eq. (2.11) and (2.20), following the assumption that the flow is frictionless and the inflow is uniform and without pre-swirl (p_{01} is constant), a relationship between $v_{z2}(r)$ and $v_{\theta 2}(r)$ can be established by:

$$v_{z2}\frac{dv_{z2}}{dr} = \left(\Omega - \frac{v_{\theta 2}}{r}\right)\frac{d}{dr}(r\,v_{\theta 2}) \tag{2.21}$$

Once the distribution of $v_{\theta 2}(r)$ has been specified, information on $v_{z2}(r)$ can be obtained. Together with known $v_{z1}(r)$ (uniform and no pre-swirl assumption), the velocity triangles upstream and downstream can be solved numerically. With

known flow angles, the required lift coefficient $C_l(r)$ (Eq. (2.18)) can be obtained for the design of the blade elements at each spanwise location.

The method starting from the distribution of $r v_{\theta 2}(r)$, following the above process towards the final blade geometry, is named *vortex distribution design method*.

Three types of vortex distribution are mainly discussed [9]:

1. Free-vortex: $r v_{\theta 2}$ is constant along the blade span.
2. Forced-vortex (also called “solid-body"): $v_{\theta 2}$ increases along the blade span, for example $r v_{\theta 2} = ar^2$.
3. Power law-vortex: $r v_{\theta 2} = ar^n + b$.

Except the three types above, it is more general to define the vortex distribution by a polynomial function (used in the current study in Chapter 8), or by a spline function:

$$r v_{\theta 2}(r) = \sum_{i=0}^{M} a_i r^i \tag{2.22}$$

where a_i are constants ($i = 1 \dots M$).

2.8 Non-radial Stacking Design

The aerodynamic development of aircraft has inspired the design of axial fans. For example, the use of a winglet at the fan blade tip for tip leakage control [24], serrated leading or trailing edges on fan blades for noise reduction [25, 26], etc. Among all these inspirations, the non-radial stacking design is the most acknowledged one. Such designs usually result in sweep, dihedral and skew.

In classical design methods for axial fans [8, 9, 11, 21, 27], the three-dimensional blade geometry is obtained by stacking the two-dimensional airfoil sections along a specific line, the so-called stacking line.

In preliminary design of axial fans, the stacking line is usually in the radial direction (two-dimensional), as shown in the sketch of a fan blade in Fig. 2.11 (together with leading and trailing edge). By applying a three-dimensional stacking line, the non-radial stacking (NRS in short) design can be achieved. Sweep, dihedral and skew are typical examples of NRS.

The sweep concept was initially introduced by Busemann [28] in 1935 to enhance drag reduction of wings at transonic speed [29]. It means that the airfoil sections are shifted in the chord direction as shown in Fig. 2.12. Here v_∞ is velocity far upstream and also the velocity “seen" by the airfoil sections of an unswept wing; under the same far upstream velocity with sweep, v_n is the velocity “seen" by the airfoil sections of a swept wing; the relationship is $v_n = v_\infty \cos\gamma$, which

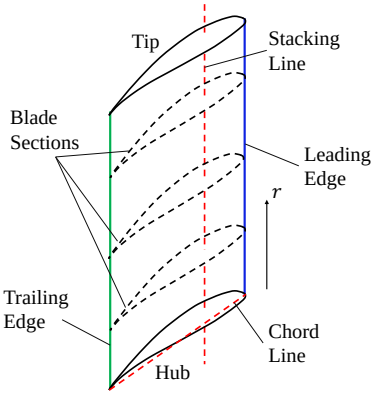

Figure 2.11: Sketch of a Fan Blade, with Blade Sections, Stacking Line and Chord Line (in Red), Leading and Trailing Edges (in Blue and Green, respectively); r denotes the radial direction.

means the velocity seen by the airfoil sections can be decreased by the use of swept wing, hence the attainment of the critical Mach number is delayed. Dihedral means the airfoil sections are shifted in the direction perpendicular to the chord direction and skew is a more general term, encompassing sweep as well as dihedral.

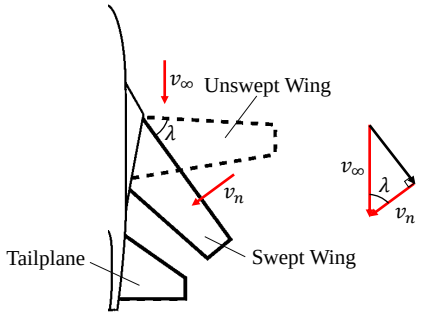

Figure 2.12: Example of Wing Sweep with the Velocity Relationship: the unswept wing is indicated by the dashed line; the swept wing by the solid line [30]; v_∞ and v_n are velocities seen by the unswept and swept wing, γ is sweep angle.

In axial fans, the chord direction dictates sweep and dihedral, while the absolute inflow and blade rotation directions dictate axial and circumferential skew, respectively [31–33]. Forward and backward sweep mean that the blade section

is shifted upstream and downstream, respectively, in the relative flow field. Forward and backward dihedral and axial skew mean that the blade section is shifted upstream or downstream, respectively, of the baseline blade section in the absolute flow field. Forward or backward circumferential skew mean that the blade section is shifted in the direction of rotation or opposite, respectively.

The blade section shifts of sweep, dihedral and skew in the Blade-to-blade view are shown in Fig. 2.13.

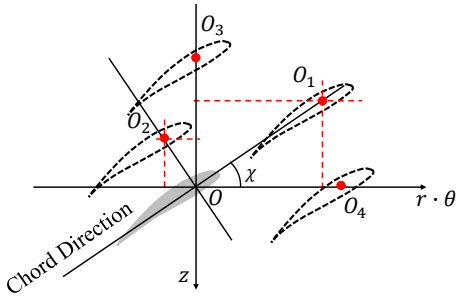

Figure 2.13: Geometrical Description of Blade Section Shift: O, O_1, O_2, O_3 and O_4 represent stacking points of original blade, and blades with (forward) sweep and dihedral, axial and circumferential skew, respectively. Inflow is in the positive z-direction

Examples of straight, forward sweep and backward sweep blades are shown in Fig. 2.14(a), (b) and (c) [34].

(a) (b) (c)

Figure 2.14: Examples of (a) Straight Fan Blades, (b) Fan Blades with Forward Sweep and (c) Fan Blades with Backward Sweep; in front view; adapted from Ref. [34].

The application of sweep, dihedral and skew in the design of axial fans has been found to be beneficial for better aerodynamic performance. However, there

is no universal conclusion on how these blade shapes can influence the aerodynamic performance for all axial fan blades, for example, forward sweep gave an increased η_{tt} in Ref. [35], unchanged η_{ts} in Ref. [33] and decreased η_{tt} in Ref. [36] and backward sweep also gave increased η_{tt} in Ref. [37] as well as decreased η_{tt} in Ref. [36]. Therefore, it seems that the application of *NRS* should depend on both the blade design and the operation duty point of the baseline unswept fan.

Chapter 3

Literature Review

For the design of axial fans, the current approach for preliminary design relies on the design theory introduced in Chapter 2 and related empirical design methodologies as introduced in Refs. [8, 9, 21, 27, 38].

The development of Computational Fluid Dynamics (CFD) simulations can make the cost of design evaluation much lower compared with standardized measurements [39] during the trial-and-error design phase.

During the optimization of preliminary designs, CFD also provides powerful tools. The evaluation of optimized blade shapes with sweep, dihedral and skew can be achieved by CFD simulations; CFD has also been coupled with optimization algorithms like artificial neural networks [40], to help searching for better designs of axial fans.

Inverse-design methods provide designs starting from the desired duty point, thus shortening the trial-and-error design phase.

The method employed in the current study is using CFD simulations to evaluate the aerodynamic performance of optimized axial fan blades designed by applying sweep, dihedral and skew, or the vortex distribution design method (a specific inverse-design method). As the foundation of further research, the appropriate CFD simulation strategy should firstly be formulated and validated, therefore the literature review of CFD simulations applied to low-pressure axial fans is reviewed in Sec. 3.1. Using sweep, dihedral and skew is the main optimization method for the blade shape variation. Meanwhile optimization algorithms coupled with CFD simulations or in design methods also contribute to improved aerodynamic performance of fan blades. The literature review of optimization methods which are applied specifically in blade shape variation and design method, is described in Sec. 3.2. The vortex distribution design method of axial fans is a specific inverse design method which has widely been used in turbomachinery design. A general review of inverse design methods for turbomachinery design and a focused review of the application of the vortex distribution design method for axial fan designs are reported in Sec. 3.3.

3.1 CFD Methods

Since the last part of 20th century, Computational Fluid Dynamics (CFD) has been applied in turbomachine (fans included) design. Details of CFD employed in the current study are introduced in Chapter 5. Commerical CFD codes, like ANSYS CFX, Fluent, NUMECA and STAR-CCM are popular, while for open-source codes, OpenFOAM is mainly used.

To compute turbulent flows with CFD simulations, different approaches can be followed, in order of increasing computational costs: Reynolds Averaged Navier-Stokes simulation (*RANS*), Large Eddy Simulation (*LES*) [41, 42] (for fans), Direct Numerical Simulation (*DNS*) [43]. RANS simulations require a turbulence model (such as $k-\epsilon$, $k-\omega$, Shear Stress Transport and Spalart-Allmaras models; *SST* and *SA* for short, respectively; see Ref. [43] for details) to describe the turbulent Reynolds stresses. An overview of turbulence models for turbomachinery applications is given in Refs. [44, 45], a review of computational methods applied in industrial fan design is given in Ref. [46].

As pointed out by the EU Commission Regulation and the US Department of Energy [6, 47], research and design for better aerodynamic performance of axial fans have been strongly motivated. During the trial-and-error design phase, the application of CFD simulations provides tools for designers and researchers to account for three-dimensional effects in the flow. Results of these simulations help to obtain details of flow fields that are difficult to obtain experimentally.

For the approaches of turbulence simulations, Direct Numerical Simulations of the Navier-Stokes equations requires very fine grids and the cost increases as Re^3 [43]. In turbomachine applications, the Reynolds number Re is usually of the order of magnitude of 10^5, which makes the computation cost of DNS beyond the available capacity of common fan designers and researchers. Similar requirements of computational cost apply for LES, since it solves the Navier-Stokes equations for large turbulent length scales. Consequently, RANS simulations are applied mostly considering their low computational costs [46].

The reliability of RANS predictions depends on the appropriate choice of turbulence model, the calculation domain, the mesh refinement and the applied boundary conditions, etc. Appropriate choices form the simulation strategy for each investigation and is closely related to specific and explicit axial fan cases. Therefore, there is no universal standard for RANS simulations of axial fans. Yet, one can refer to others' experience and achievements.

3.1.1 Turbulence Model

For the turbulence model applied in RANS simulations, the Spalart-Allmaras' (*SA*) one equation model [48] is included in many commercial CFD codes [46] and

has been successfully employed in studies of axial fans [49, 50]. The *SA* model employed in the study of linear cascade flows [51] proves that it is capable of predicting on cascade blades' pressure distribution, the lift and drag coefficients, which confirms the reliable application in simulations of axial fans. Two-equation models can be represented by the $k-\epsilon$ model [52] and the $k-\omega$ model [53, 54]. The $k-\epsilon$ model predicts better within the main flow while the $k-\omega$ model performs better near the wall [55]. The model that combines advantages of the $k-\epsilon$ and the $k-\omega$ turbulence models is the Shear Stress Transport (*SST*) model [56].

Although two-equation models naturally increase computational cost, they have been successfully applied in axial fan research.

For instance, the $k-\epsilon$ model has been employed by Vad et al. [57, 58] to investigate the aerodynamic performance of skewed blades. Fairly good agreement has been found between measured and predicted aerodynamic performance. Beiler and Carolus [33] has applied the $k-\epsilon$ model to verify a design methodology for skewed blades. Although the aerodynamic performance has not been compared directly, the velocity distribution downstream of fan rotor has been well predicted by CFD simulations. In Wilkinson's research [59], the CFD predictions based on $k-\epsilon$ model correlate well with measurements for ψ and η_{ts}.

Similarly, the $k-\omega$ model employed by Masi et al. [60] and the *SST* model applied in Refs. [61, 62] have proven their reliability in CFD simulations of axial fans.

The *SA*, $k-\epsilon$, $k-\omega$ and *SST* turbulence models are all linear eddy viscosity turbulence models where the turbulent Reynolds stress tensor is related to the mean strain tensor in a linear way. For complex fluid flows, the accuracy of linear eddy viscosity turbulence models in predicting of some turbulence features like the anisotropy in the normal stresses is limited. The accuracy of modeling the turbulence features can be improved by applying nonlinear eddy viscosity turbulence models (*NLEVM*) [46, 63], like the cubic $k-\epsilon$ model [64] and the Explicit Algebraic Reynolds stress models (*EARSM*) [65].

Nonlinear eddy viscosity turbulence models have been applied successfully in both the simulations of a compressor cascade with high load [66] and an axial fan with high-pressure [67], and the fan's performance has been accurately predicted within the uncertainty measured during experiments. The advantage of *NLEVM* is the increased accuracy of modeling complex flow fields in turbomachinery like cascade flows [68] and tip leakage flows [69], but the increased number of transport equations results in additional computational cost and numerical uncertainty that may lead to solver's nonconvergence. Such drawbacks make the choice of *NLEVM* in the study of axial fans quite limited. In the current study, the linear eddy viscosity turbulence models are selected.

3.1.2 Calculation Domain

In the determination of the calculation domain, both axial and radial extent should be considered. With a different test rig, the shape of domain may be different. For example, according to the international standard IS0 5801 [39, 70], open-flow or ducted-flow test facility are both possible [71]. The tested fan may exhaust air into open atmosphere or pipeline. Therefore outlet calculation domains with a larger radial range (in shape of cylinder or sphere) or duct with the same diameter of fan casing are both possible. For instance, a radially extended calculation domain has been employed in Refs. [24, 34, 72] and an extended duct domain has been employed in Refs. [33, 49, 57, 73].

The details of inflow characteristics may influence the choices. In the investigation of Corsini and Rispoli [74] for a high-pressure ventilation axial fan, the inflow details are well-conditioned, and the calculation domain extends only one chord length upstream and downstream of the leading and trailing edge. In the research of an axial fan for air cooled condensers [75], the calculation domain extends 1.0 and 1.5 chord of blade leading and trailing edge in upstream and downstream direction, respectively.

In most cases of axial fan designs and simulations, the no pre-swirl assumption and uniform inlet conditions have been applied. Under such considerations, only one chord length may not be sufficient. For example, Masi and Lazzaretto [76] have investigated four different calculation domains for the same rotor-only axial fan. The differences include tip gap, shape of the electric motor and bell-mouth entry and other elements in the system of the test rig which gives different extents in radial direction. In this investigation, the inlet is set four chord length upstream and the outlet is set to six chord length downstream of the rotor, which is much larger than the values in Refs. [74, 75]. The results show that the calculation domain with tip gap and without radial extension gives precise predictions of the fan performance. However, for rotor-only axial fans with small hub-to-tip diameter ratio, the tip gap is not recommended to be considered within the calculation domain [50] to obtain good agreement between CFD predictions and experiments.

3.1.3 Boundary Conditions and Grid Refinement

With respect to the boundary conditions at the inlet and outlet in the CFD simulations of axial fans, two main types are employed as listed in Table 3.1. For instance, type 1 boundary condition is prescribed in Refs. [34, 57, 76, 77] and type 2 is prescribed in Refs. [49, 50, 72, 73, 76].

Both type 1 and 2 provide fairly accurate predictions in their corresponding studies. Therefore, when setting the boundary conditions, they should be based

Table 3.1: Main Types of Inlet and Outlet Boundary Conditions

	Inlet	Outlet
1	Mass Flow Rate [kg/s]	Averaged Static Pressure [Pa]
2	Total Pressure [Pa] and Temperature [K]	Mass Flow Rate [kg/s]

on the explicit data obtained by researchers during the measurements and as close to physical reality as possible.

The grid refinement plays an important role to ensure the accuracy of RANS simulations. One of the objectives is to make the first grid node away from walls lie in the viscous sublayer ($1 < y^+ < 5$), therefore the grid near solid boundaries is required to be very fine. Except for the wall distance of the first grid node, the expansion ratio and the aspect ratio of the cells should also be as small as possible to avoid undesired distorted cells [78]. For structured meshes, the skewness angle is expected to be as close to 90 degree as possible for good mesh quality. A larger number of grids can give better mesh quality, but it is impossible to infinitely increase the number of grids, which would increase the computational cost simultaneously. Therefore, a grid convergence study is necessary to formulate a standard for mesh generation with good quality for reliable prediction and acceptable computation cost. Guidelines for assessing the accuracy of CFD solutions are reported in Ref. [79]. In the current study, grid convergence study is done by following these guidelines.

3.1.4 Validation

The simulation strategy can be formulated based on considerations of the factors discussed above, the validation of the strategy mostly depends on the comparison with experimental data. It is important to determine what is to be compared.

During measurement, although only the stable data will be collected with uncertainty analysis, the obtained data are still instantaneous parameters. The RANS simulation predicts the time-averaging value of each physical parameter, which means that the RANS model does not adequately predict the momentary flow physics [46] in all aspects. Therefore, overall performance or local turbulent flows can be selected as reference parameters to compare measured and predicted results. The choice should also depend on the focus in research and the kind of data obtained during the measurements. For example, both local velocity distributions and overall aerodynamic performance at the design point are compared in the study of an axial fan with skewed blades [57, 58]. In the study of an axial fan with medium hub-to-tip diameter ratio [80], only the overall aerodynamic performance is compared for results of RANS CFD simulations and experiments; while

in the study of another axial fan with skewed blades with medium hub-to-tip diameter ratio [33], only local velocity distributions at some distance downstream of rotor are compared. The RANS CFD simulation results are all reported to be successfully validated in these studies.

Represented by the examples described above, in different studies, the selected reference parameters for the validations of RANS CFD simulations may be different. The selection of reference parameters relies highly on the measured variables. It can be concluded that the measured variables determine the parameters that can be compared for validation of RANS CFD simulation strategy.

Based on the reviews above, the choice and validation of a simulation strategy should consider many aspects like the applied turbulence model, the calculation domain, the refinement of grids and the measured data. For the current research, it is necessary to formulate a validated simulation strategy that is appropriate for the study of low-pressure axial fans with small hub-to-tip diameter ratio.

3.2 Optimization

Optimization always aims for better performance (in some aspects) compared to the baseline reference case. With respect to the design of turbomachines (axial fans included), optimization can be employed directly in explicit blade shape design (based on existing blades) or in the design methodology without referring to the baseline blade shape.

For the optimized blade shape design, sweep, dihedral and skew have contributed to the improvement in overall performance. As for the optimization during the design, methodologies such as stochastic methods (like an evolutionary algorithms), gradient-based methods (like adjoint method) and data mining can be applied. Under these three broad categories, many specific methods can be found and utilized. Since the focus of the current study is not on optimization methods, the methods and algorithms employed in the design and research of axial fans are mainly discussed. More information about optimization methods for turbomachinery aerodynamics is given in Ref. [81].

3.2.1 Sweep, Dihedral and Skew

The concepts of sweep, dihedral and skew are described in Sec. 2.8. After being introduced from aircraft research, starting from Godwin's [82] research on compressor blades and Mohammed and Raj's [83] study on axial fans, the sweep, dihedral and skew effects have been studied for more than 50 years. Two remarkable overviews are given by Vad [84, 85] in 2008 and 2012, where global and local effects of forward sweep and skew have been discussed in detail. Up till now, it has been well acknowledged that forward types of sweep, dihedral and skew

are able to contribute to better performance of axial fans like higher total-to-total efficiency η_{tt} [31, 35, 86] and lower sound power level [33]. The improvement of the global overall performance originates from local effects.

With respect to the effects of forward skew variation on the velocity distribution, a general explanation is as follows. Forward blades at higher spanwise location protrude into the upstream flow and are able to perform work on the fluid in advance. Considerations of radial equilibrium theory show that local axial velocities are increased at higher span and decreased at the lower span. The increased axial velocities result in a larger flow incidence angle (or angle of attack), resulting in a higher lift coefficient. This idea is in agreement with Ref. [33] and it has also been pointed out that such effects are revealed in the vicinity of the hub and shroud rather than near the mid spanwise location where the two-dimensional airfoil theory is the most appropriate.

The change of axial velocity upstream and downstream also affects the distribution of other velocity components, especially the circumferential velocity downstream of the fan blades $v_{\theta 2}$. Based on mass and energy conservation considerations, $v_{\theta 2}$ is decreased with increased axial velocity and the blade load represented by the vortex distribution $r v_{\theta 2}$ is decreased. Therefore, the forward blade variation near the wall results in blade unloading. Such effects have been confirmed in Refs. [31, 57, 87, 88]. Another effect on the flow fields downstream of the rotor blades is that the secondary flow is found to be reduced (increased) by forward (backward) blade sweep, respectively [34].

The reduction of the radial outward flow path is an important effect of forward skew variation. Such shortened flow paths contribute to decreased accumulation of low-momentum fluid in boundary layers at the blade suction side [35, 89–91] and surface friction losses. In Refs. [57, 85, 92], the shortened flow path has been illustrated. The measured pressure distribution in Refs. [83, 90] and the streamlines from CFD simulations in Refs. [89, 91, 93] near the blade suction side surface also confirmed this. Therefore, the accumulation of low-momentum fluid near the tip is reduced. The associated reduction of end-wall and the tip losses both contribute to the improvement of efficiency [35].

An analogous reasoning that explains the benefits of forward skew variation shows that backward type are less favourable for improvement of aerodynamic performance [89].

Besides the benefits discussed above that can be observed in forward skew variation, the suppressed secondary flow and delayed corner stall have been reported in blades with forward dihedral [94] and the opposite effects from backward dihedral have also been reported [95]. An extreme case with 45° forward dihedral is able to eliminate stall in an axial fan with medium hub-to-tip diameter ratio [96]. Although beneficial stall elimination can be obtained, dihedral with

such a large angle may not be recommended due to the consideration of stability of the rotor structure. The suppressed secondary flow means loss reduction, but it is also suggested by Refs. [31, 32, 84, 97] that the loss reduction obtained from forward dihedral near the hub or shroud may increase the loss near mid spanwise locations.

The sweep, dihedral and skew applied to the baseline rotor blades represent the shift of blade sections at corresponding spanwise location. This shift can be decomposed into two mutually perpendicular directions, which makes the benefits have common origins. This explains why sweep and circumferential skew are often investigated together as shown in Refs. [33, 84]. However, the associated discussion of dihedral and axial skew is not that common. The investigation of forward axial skew is only found in Ref. [91] and discussion about backward axial skew can hardly be found.

It should be noted that the benefits of sweep, dihedral and skew are not universal. All the advantages discussed above are reported with different blades under different flow coefficients φ. For example, forward sweep is able to give increased and decreased η_{tt} in Ref. [35] and [36], the same η_{ts} in Ref. [33], while backward sweep is also able to increase η_{tt} in Ref. [37].

Therefore, just like the CFD simulation strategy, it is necessary to investigate the effects of sweep, dihedral and skew on the aerodynamic performance for a specific baseline rotor and it is recommended that not only the overall performance, but also the local effects of sweep, dihedral and skew should be investigated.

3.2.2 Optimization in Design Method

The aerodynamic optimization of axial fans is still under development [98]. Many methods can lead to some optimized results validated by CFD simulations. Thévenin and Janiga [40] reported some CFD-based optimization algorithms, ranging from the simplex method [99] to gradient-based and evolutionary algorithms.

The evolutionary algorithms like artificial-neural networks, differential evolution methods and others for finding a target value of a constrained nonlinear multivariable function have been applied in direct optimization of turbomachinery.

CFD simulations (mainly RANS methods) can be utilized to evaluate the optimization results of turbomachinery. More applications provide the possibility to obtain large databases to “train" meta-models in artificial neural network (ANN) methods for improved designs.

The optimization process is similar with trial-and-error design, the performance of most blade designs from optimization methods is mostly validated by CFD simulations. Li et al. [100] have applied a single objective genetic algorithm

and a gradient algorithm to search for optimized curvature of a blade section camber line for better performance of a high-loaded axial fan. Within the optimization system, NUMECA Fine/Turbo is coupled as CFD solver for analysis of performance and flow fields from optimized fan blades in each iteration step. A multi-objective optimization technique has been developed and utilized by Kim et al. [101] to enhance performance of an axial fan in total-to-total efficiency η_{tt} and input power P_{shaft}. Six design variables relating to blade angles and profile were selected within the design space. The response surface approximation model that had been employed in Refs. [102, 103], was constructed for each objective function based on the CFD simulation results at design points. The genetic algorithm was used for multi-objective optimization search. The results showed that higher η_{tt} and lower P_{shaft} can be obtained.

Key parameters in the design of axial fans are the choices of airfoil and the angle of attack of blade sections. Carolus and Starzmann [104] has coupled XFOIL which has been developed for design and analysis of isolated airfoils [19], with a design method to assist in the determination of airfoil performance and the choice of optimal angle of attack for optimized blade section design.

Lin et al. [105] in 2002 coupled CFD simulation and artificial neural network to improve the blade design of a rotor-only axial fan with large hub-to-tip diameter ratio. As reported recently in Refs. [106, 107], RANS simulations of axial fans with different geometry parameters have been performed with the *SST* turbulence model. Around 13,000 fan performance curves have been obtained for further artificial neural network training. The meta-models from these ANNs are able to derive rules for the choices of optimal geometrical parameters at certain duty points, so that the CFD simulations for new duty points are no longer needed. By comparing the results from the meta-models and CFD predictions, good agreement has been found in the sense that the desired duty points are achieved. However, it should be noted that, there are certain ranges of selected geometry parameters that researchers should pay attention to. These optimization methods also result in the study on ideally achievable η_{ts} of axial fans with duty point located within the Cordier band as reported in Ref. [13].

The meta-model method is faced with the problems regarding the selected geometrical parameters. More parameters requiring more CFD simulations, the computation cost would be expensive. The adjoint method is able to overcome such restrictions by determining the gradient of the objective function from a single additional computation [98]. The details of the adjoint method can be found in Ref. [81] and are not discussed here. Following the successful application of the adjoint method on fan rotor blade optimization [108], this method had been applied in both RANS equations and boundary conditions for optimization of a

baseline fan by using the existing OpenFOAM solver “adjointShapeOptimizationFoam" and the results showed increased maximum pressure and total-to-static efficiency by 3.6% and 0.1%, respectively [98].

It should be noted that the discussed optimization methods may only occupy a small portion of available and developing methods for optimization design in axial fans. However, it can be shown that CFD simulations are of great importance for designers and researchers during the design. By coupling with other optimization algorithms, more advanced designs may be found. The appropriate choice should refer to both algorithm development and corresponding application.

3.3 Inverse Design Method

Inverse design is a concept different from direct design. In the design of turbomachinery, the direct design is classically based on empirical approaches to determine the parameters of the blade geometry, while inverse design methods prescribe the pressure distributions along spanwise locations as boundary conditions for the blade section profile calculation or selection [109], so the internal flow fields of turbomachinery are controlled by geometrical parameters in direct design and aerodynamic or hydraulic parameters in inverse design [110]. Such a difference determines the advantages of inverse design: the design results have the desired performance characteristics.

The development of inverse design has progressed from two-dimensional to quasi three-dimensional and finally to fully three-dimensional. A good classification with corresponding references can be found in Ref. [109]. The application of quasi three-dimensional method has been reported in Refs. [111, 112]. As mentioned by Westra [113], the first applications of three-dimensional method in turbomachinery design were reported in Refs. [114, 115] and extended by Zangeneh [116] in the design method for radial and mixed flow turbomachinery. This method had also been successfully applied in design of compressor diffusers [117], a mixed-flow pump impeller [118] and a centrifugal compressor [119].

In the meantime, the development of inverse design methods contribute to the inverse airfoil design tool like XFOIL [19].

Apart from the applied inverse design methods in radial and mixed flow turbomachinery, the mature and well-acknowledged design method of axial flow turbomachinery, which is based on vortex distribution, is naturally an inverse design method. As has been reported from Patterson’s original work [120] in Wallis’s book [21], the early design method of axial fans is based on the spanwise load distribution represented by the swirl coefficient (ratio between circumferential velocity and axial velocity component). With a specified configuration of

fan structure, the known swirl coefficient provides the velocity components upstream and downstream of rotor, and subsequently the shape of blade section can be determined based on the blade element theory introduced in Sec. 2.5.

A practical inverse-design approach of axial fans was reported in detail in 1993 by Downie et al. [121] for design with an arbitrary vortex distribution, where the design philosophy and method were described step by step. The experimental set-up and procedures were also described. Following the inverse-design method idea, forward blade sweep is incorporated in the preliminary design to utilize the benefits of sweep in reducing the losses on the suction side away from endwalls [122]. With application of CFD simulations. Fairly good agreement was found between predictions and design expectations. Masi and Lazzaretto [123] in 2019 described design approach, integrating design ideas reported by Wallis et al. [21, 121] and Vad [122] for design of axial fans with high total-to-total efficiency η_{tt}, where a mean-line model, described in Ref. [124], was applied to estimate the η_{tt} of axial fans having constant swirl blade loading. The results showed that the design method permits to obtain increased performance with respect to η_{tt}, but the low Reynolds number due to the fan's small size limited the improvement.

With the known design ideas, the key point during the utilization of the inverse design method is the determination of the type and value of the blade loading distribution, explicitly the pressure distribution or vortex distribution. For example, in a low-speed radial-inflow turbine, a suitable mean-swirl distribution is recommended [117] and in a low-pressure rotor-only axial fan, a free-vortex (constant vortex distribution) is recommended for the highest total-to-total efficiency η_{tt} [125]. However, the value of each distribution is mostly from experience of the researcher or designer before the application of the optimization method.

Combination of inverse design methods and an optimization method usually results in efficient design process [126, 127]. Most of the optimization methods discussed in Sec. 3.2.2 can be combined with an inverse design method. For example, the differential evolution method has been applied in the inverse design method of centrifugal pump [113] and axial fan [128]. The ideas of achievable total-to-static efficiency η_{ts} analysis [13] also provide a good method to obtain optimized vortex distribution in the rotor-only axial fan design.

It should be noted that, the inverse design methods discussed above are based on inviscid flow. In the recent research of Liu et al. [110], the loading distribution is obtained based on boundary vorticity flux diagnosis to improve the accuracy of the inverse design method.

In summary, the inverse design method of turbomanchinery has experienced a long term development, the application of optimization method and further consideration of viscous effects can result in more efficient design method.

3

Chapter 4

Baseline Fans

In this chapter, the geometrical information of baseline fan blades is described in Sec. 4.1, the test facility in Howden Netherlands is introduced in Sec. 4.2, the measurement procedures and results for the Howden baseline fan are given in Sec. 4.3. The US17 fan, which is employed to verify the validated CFD simulation strategy reported in Chapter 6, is introduced in Sec. 4.4.

It should be noted that all the measurements reported in this thesis have not been performed by the author. For the baseline Howden fan, all measured data is obtained by personal communication. For the US17 fan, details of measurements have been described in Ref. [80] and the author, Prof. Thomas Carolus, is thanked for sharing the measured data.

4.1 Configuration of Baseline Howden Fan

The structure of axial fans mainly consist of motor, shaft, rotor and other supporting mechanical parts. According to explicit design requirements, based on comprehensive considerations like low cost and space limitations, inlet and outlet guide vanes can be applied to obtain desired pre-swirl upstream and higher static pressure downstream, respectively. When the guide vanes are absent, the fan is called a rotor-only axial fan.

The baseline Howden fan is a rotor-only axial fan and its structure is shown in Fig. 4.1. The casing, hub and fan diameters are indicated by D_{casing}, D_{hub} and D_{fan} respectively.

The ratio between D_{hub} and D_{fan} is called the hub-to-tip ratio κ (Eq. (1.5)).

Due to the presence of a small gap between the tip of the rotating blades and the stationary casing, D_{fan} is smaller than D_{casing}. The gap between blade tip and outer casing is called tip-gap and the tip-gap ratio ϵ is defined by:

$$\epsilon = \frac{D_{\text{casing}} - D_{\text{fan}}}{2D_{\text{fan}}} \tag{4.1}$$

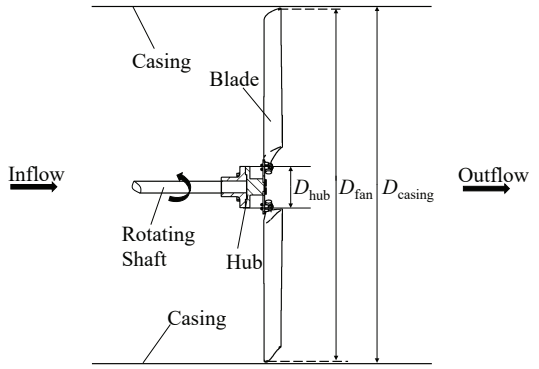

Figure 4.1: Example of the Structure of a Rotor-only Axial Fan: showing casing, blade, rotating shaft and hub.

The details of the fan blades used in the current study are shown in Fig. 4.2. Each of the six identical blades is divided into two parts (for the geometrical description), the “main blade" and the “non-airfoil part", as indicated in Fig. 4.2 (a); the starting location of the main blade is at $0.18R_{\text{fan}}$.

For the main blade, the airfoil sections correspond to the Wortmann profile [129], with chord length of 0.15m, see also Fig. 4.2 (b) and (c). The sections are slightly twisted by an angle of 4° between the sections at positions A and B, indicated in Fig. 4.2 (a), in anticlockwise direction. The centre of rotation for the sections (to account for the twist) is located at the point of maximum thickness, represented by position O in Fig. 4.2 (b). The blade is straight from the section at position B to the blade tip. The stagger angles (as defined in Fig. 4.2 (c)) for this fan are measured at the tip of blade and can be adjusted from 5° to 30°; here the considered stagger angle equals 15°. The line that determines the stagger angle as shown in Fig. 4.2 (c) is called the *stagger line*.

The main geometrical and design parameters of the baseline fan are summarised in Table 4.1.

4.2 Test Facility

Accurate data of aerodynamic performance of axial fan have been experimentally determined in a test facility built according to an international standard [39]. The measured values are vital to evaluate the accuracy of numerical simulations.

The measurements of the baseline Howden fan have been performed in the Howden test facility built according to the international standards AMCA 210

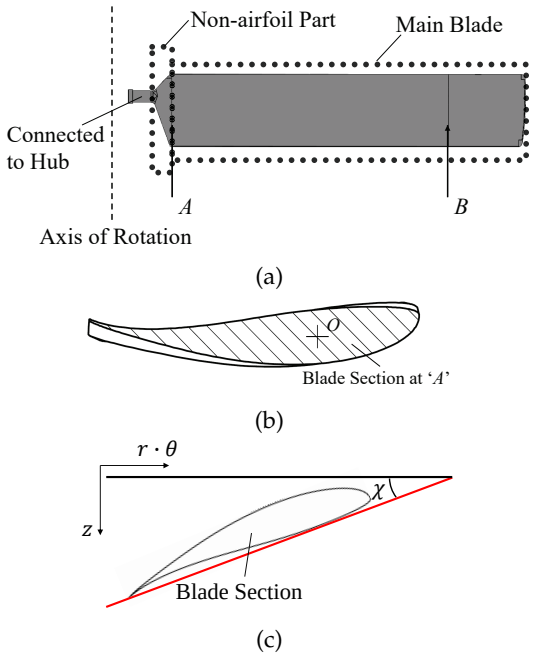

Figure 4.2: Geometrical Description of the Howden Fan with Small Hub-to-tip Ratio: (a) Fan Blade: main blade and non-airfoil part, (b) Wortmann Profile (filled with section line) and Blade Twist: view from position A, (c) Stagger Angle χ and Stagger Line (in Red)

.

Table 4.1: Geometrical and Design Parameters of the Baseline Howden Fan.

Rotational Speed [rpm]	497
D_{casing} [m]	1.845
D_{fan} [m]	1.829
κ [-]	0.14
ϵ	0.43%
Number of Blades	6
Stagger Angle [deg]	15
Chord Length of Main Blade [m]	0.15
Solidity at Tip [-]	0.157
Solidity at Blade Section A [-]	0.844

and ISO5801 [39], which ensures the high-quality of the measured aerodynamic performance characteristics. The test facility is shown schematically in Fig. 4.3.

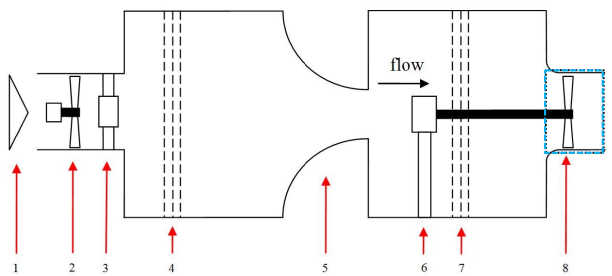

1. Tuneable Inlet Valve 2. Booster Fan 3. Outlet Guide Vanes of Booster Fan 4. Settling Screens 5. Nozzle 6. Electric Motor 7. Settling Screen 8. Test Fan.

Figure 4.3: Schematic Overview of the Howden Cooling Fan Test Facility [39].

The tested fan part is indicated in the blue dotted rectangle on the right of Fig. 4.3 (item 8). The inner diameter of the casing, D_{casing}, of the test part is 1.845m. The variable inlet valve and the booster fan help to adjust and overcome the system resistance, so the whole aerodynamic performance curve of the fan is obtained, from free delivery (zero pressure rise) to shut-off (zero flow rate).

The volumetric flow rate Q through the fan is determined from the static pressure drop over the nozzle measured by a digital differential pressure transducer. An array of three Pitot tubes assembled at the inlet of the tested fan is used

to measure the total pressure (relative to the atmospheric pressure p_2), which gives the Fan Static Pressure p_{fs} in Eq. (1.1). The fan shaft power P_{shaft} is determined from the shaft torque and the fan rotational speed, which are measured by a torque meter and an induction sensor, respectively. The gas (air) density is determined by measuring the ambient temperature, relative humidity and atmospheric pressure. The measured variables, corresponding sensors and their accuracy are given in Table 4.2.

Table 4.2: Measured Variables, Corresponding Sensors and their Accuracy [39].

Measured Variable	Sensor	Sensor Accuracy
Pressure Difference Over Nozzle	Differential Pressure Transducer	±1%
Total Pressure Inlet Chamber	Differential Pressure Transducer	±1%
Fan Speed	Induction Sensor	±0.5%
Fan Shaft Torque	Torquemeter	±2%
Ambient Temperature	Temperature Sensor	$\pm 0.5^{\circ}C$
Relative Humidity	Humidity Sensor	±2%
Atmospheric Pressure	Barometric pressure sensor	$\pm 170Pa$

4.3 Measurement Results

The measurements start near free-delivery conditions. Subsequently, the system resistance is increased in small steps until the fan reaches stall condition. One or two measurements above the stall condition are made in order to construct the fan curve. The system resistance is then lowered in small steps until the fan reaches free-delivery again. Hence, each performance condition is measured twice. These measurement procedures guarantee the high quality of the measured aerodynamic performance, so meaningful comparisons between measurements and numerical prediction are possible. Based on all measured and derived variables, the fan performance curves represented by the dimensionless coefficients φ, ψ, λ and η_{ts} (defined in Eqs. (1.1) and (1.3)) are obtained.

The measured fan performance curves for the baseline fan with $\chi = 15^{\circ}$ are shown in Fig. 4.4.

Based on the experimental data at the peak of the $\varphi - \eta_{ts}$ curve, the Reynolds number $\mathrm{Re} = 4.6 \times 10^5$ and the Mach number $\mathrm{Ma} = 0.14$, therefore the flow in current research is treated as incompressible turbulent flow.

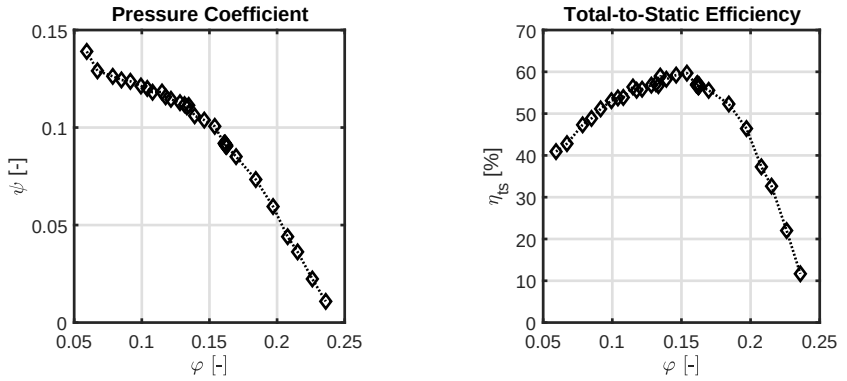

(a) (b)

Figure 4.4: Measured Baseline Fan Performance Curve (a) φ - ψ; (b) φ - η_{ts}

4.4 US17 Fan

The US17 fan is a medium hub-to-tip ratio fan, its configurations and measurements have been fully described in Ref. [80]. In order to verify that the investigated CFD simulation strategy is also adequate for medium hub-to-tip ratio fans, CFD simulations of the US17 fan have been performed and reported in Chapter 6.

The 3D model of the US17 fan adapted from Ref. [80] is shown in Fig. 4.5 and its detailed configuration is given in Table 4.3.

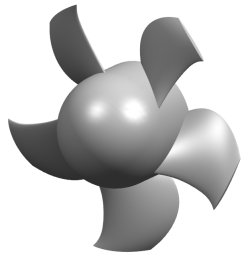

Figure 4.5: 3D Model of US17 Fan

The measurements on the US17 Fan have been done in the test rigs at the University of Siegen built according to the German standard DIN 24163 [80], as shown in Fig. 4.6.

Table 4.3: Geometrical and Design Parameters of the US17 Fan.

Rotational Speed [rpm]	3000
D_{casing} [m]	0.3
κ [-]	0.45
ϵ	0.1% or 1%
Number of Blades	5
Chord Length at Hub [m]	0.086
Chord Length at Tip [m]	0.068

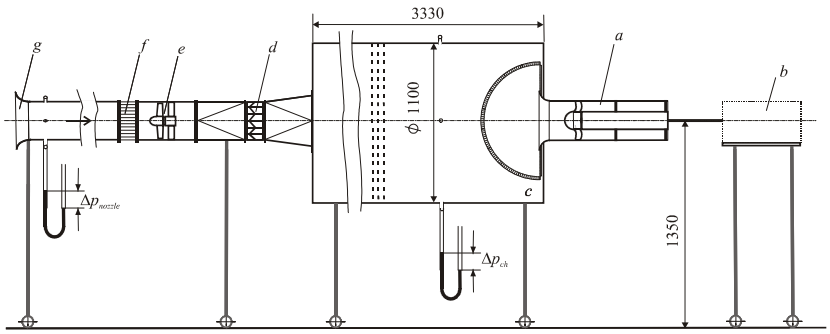

a. Fan Assembly; b. Electric Motor with Integrated Torque Meter; c. Settling Chamber with Internal Screens; d. Adjustable Throttle; e. Auxiliary Fan; f. Flow Straightener; g. Volume Flow Rate Metering Nozzle.

Figure 4.6: Schematic Overview of the Test Rig for the US17 Fan (adapted from Ref. [80])

The measured pressure rise ψ and total-to-static efficiency η_{ts} are shown in Fig. 4.7 (a) and (b) and will be compared with prediction results to verify the CFD simulation strategy developed in the current study.

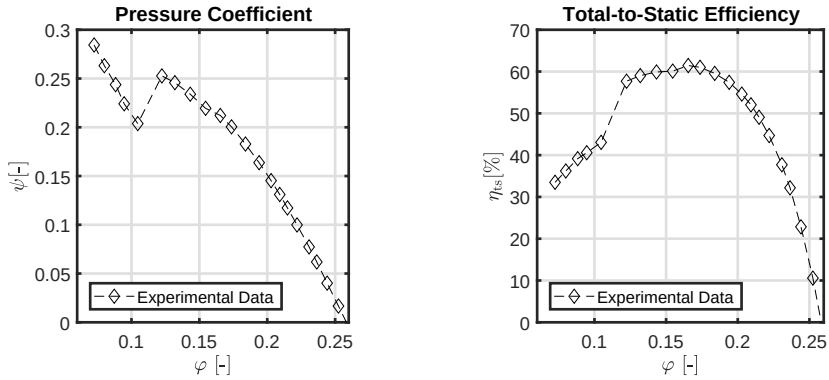

(a) (b)

Figure 4.7: Measured US17 Fan Performance Curve (a) φ - ψ; (b) φ - η_{ts}

Chapter 5

Numerical Method

In the current study, Computational Fluid Dynamics (CFD) is mainly used to perform simulations of low-pressure axial fans, so it is necessary to obtain reliable CFD methods. The main types of CFD methods are Direct Numerical Simulation (DNS), Large-Eddy Simulation (LES) and Reynolds-averaged Navier Stokes Simulation (RANS) [43]. DNS and LES are computationally expensive, RANS is usually applied, with the benefit of limited computational costs.

In this chapter, the fundamental mathematical models (mass and momentum conservation) of fluid motion are introduced first in Sec. 5.1. The Reynolds-averaged Navier-Stokes equations and employed turbulence models are described in Sec. 5.2. The calculation domain for the simulations, the mesh generation and the grid convergence study are mentioned in Sec. 5.3 and 5.4. The validation of the developed CFD simulation strategy is described in Chapter 6.

5.1 Flow Equations

When establishing mathematical models, it is common to assume that the fluid is a continuous medium, the so-called continuum. Based on this assumption, the fluid flow has to satisfy the conservation laws of mass, momentum and energy [130].

The continuity equation, describing mass conversation, is

$$\frac{\partial \rho}{\partial t} + \frac{\partial}{\partial x_i}(\rho v_i) = 0 \tag{5.1}$$

where v_i is ith component of absolute velocity vector, x_i denotes the ith spatial coordinate, ρ is the fluid density. The Einstein summation convention has been employed, implying a summation over repeated subscripts.

For incompressible flow this becomes

$$\frac{\partial v_i}{\partial x_i} = 0 \qquad \text{or} \qquad \nabla \cdot \mathbf{v} = 0 \tag{5.2}$$

Based on Newton's second law, the momentum equation relates the fluid particle acceleration (material derivative of velocity) to the surface forces and body forces experienced by the fluid [43]. The surface forces are described by the stress tensor and body forces are from gravity or centrifugal force.

The Navier-Stokes equations for incompressible flow of a Newtonian fluid are

$$\rho\left(\frac{\partial v_i}{\partial t} + v_j \frac{\partial v_i}{\partial x_j}\right) = -\frac{\partial p}{\partial x_i} + \mu \frac{\partial^2 v_i}{\partial x_j \partial x_j} + \rho g_i \tag{5.3}$$

Here p is pressure, μ is dynamic viscosity, ρg_i denotes body force.

5

5.2 RANS Equations and Turbulence Model

The essential characteristic of turbulent flows is that the fluid velocity varies significantly and irregularly in both position and time [43], therefore the velocity can be denoted by $\mathbf{v}(\mathbf{x}, t)$, where $\mathbf{x}$ is the position and t is the time.

In DNS, the Navier-Stokes equations are solved to determine the $\mathbf{v}(\mathbf{x}, t)$. The computational costs are very high and increase as Re^3 since all lengthscales and timescales need to be solved, so it is generally limited to relative low Reynolds numbers. LES solves the Navier-Stokes equations for large turbulent length scales and the smaller scales are modeled by a turbulence model, very fine meshes and small steps are required. As for RANS, the mean velocity field $\overline{\mathbf{v}}(\mathbf{x})$ is determined by the Reynolds-averaged equations, the Reynolds stresses are described by a turbulence model [43]. The computational costs are much lower than for DNS and LES. Considering $\mathrm{Re} = 4.6 \times 10^5$ and that the need to carry out many CFD simulations in the current study, RANS simulations are chosen.

NUMECA FineTurbo is the software used in the current study, as a compressible solver for compressible flows, Favre averaging (density weighted averaging) is applied in the derivation of the RANS equations [63]. However, the flows in the current research are effectively incompressible with low Mach number, and hence the density is nearly constant, so the process of Favre averaging is for simplicity not shown. Details can be found in Ref. [131]. Here, the main ideas of the time averaging in the derivation of the RANS equations are explained.

The decomposition of the instantaneous velocity $\mathbf{v}(\mathbf{x}, t)$ into its time-mean $\overline{\mathbf{v}}(\mathbf{x})$ and fluctuation $\mathbf{v}'(\mathbf{x}, t)$ is referred to as Reynolds decomposition [43]:

$$\mathbf{v}(\mathbf{x}, t) = \overline{\mathbf{v}}(\mathbf{x}) + \mathbf{v}'(\mathbf{x}, t) \tag{5.4}$$

Considering the absence of a stator in rotor-only axial fans, the flow field can be treated as a statistically steady flow, the time-mean $\overline{\mathbf{v}}(\mathbf{x})$ can be expressed by

$$\overline{\mathbf{v}}(\mathbf{x}) = \frac{1}{T}\int_0^T \mathbf{v}(\mathbf{x}, t)\, dt \tag{5.5}$$

and therefore

$$\frac{1}{T}\int_0^T \mathbf{v}'(\mathbf{x}, t)\, dt = 0 \tag{5.6}$$

Here T is the time interval used for averaging, which is required to be larger than the typical time scales of the fluctuations [132].

Substituting the Reynolds decomposition (Eq. (5.4)) into Eqs. (5.2) and (5.3), the RANS mass and momentum equations become

$$\frac{\partial \overline{v}_i}{\partial x_i} = 0 \qquad \rho\left(\frac{\partial \overline{v}_i}{\partial t} + \overline{v}_j \frac{\partial \overline{v}_i}{\partial x_j}\right) = -\frac{\partial \overline{p}}{\partial x_i} + \mu \frac{\partial^2 \overline{v}_i}{\partial x_j \partial x_j} - \rho \frac{\partial (\overline{v_i' v_j'})}{\partial x_j} + \rho g_i \tag{5.7}$$

with $-\rho\overline{v_i' v_j'}$ named as the Reynolds stress tensor.

For general statistically three-dimensional flow, the mean continuity equation and RANS equations in three components govern the mean velocity field. However, in addition to $\overline{v}_i$ and $\overline{p}$, there is also the unknown Reynolds stress $-\rho\overline{v_i' v_j'}$. Therefore, the number of equations is smaller than the number of unknown variables. This so-called closure problem is addressed by modeling the Reynolds stress tensor according to the Boussinesq eddy viscosity hypothesis:

$$-\overline{v_i' v_j'} = \nu_t \left(\frac{\partial \overline{v_i'}}{\partial x_j} + \frac{\partial \overline{v_j'}}{\partial x_i}\right) - \frac{2}{3} k \delta_{ij} \qquad \text{with} \qquad k = \frac{1}{2}\overline{v_i' v_i'} \tag{5.8}$$

where ν_t is the so-called turbulent kinematic viscosity, δ_{ij} is the Kronecker delta symbol and k is the turbulent kinetic energy.

Many models for the turbulent viscosity ν_t and the turbulent kinetic energy k have been proposed [43], such as $k-\epsilon$, $k-\omega$, Shear Stress Transport (SST) and Spalart-Allmaras (SA) models; *SST* and *SA* for short, respectively. With respect to turbomachinery application, overviews of applied turbulence models are given in Refs. [44, 45]

Here the Shear Stress Transport turbulence model [56] and the one-equation Spalart-Allmaras turbulence model [48] are considered.

The Shear Stress Transport (SST) turbulence model is based on the $k-\epsilon$ and $k-\omega$ models [43]. A "blending function" F_1 is introduced to multiply the final term in the $\omega-$ equation to blend the model coefficients in boundary layer zones with the transformed $k-\epsilon$ model in free-shear layer and free-stream zones [63]. Therefore, the SST model combines advantages of the $k-\epsilon$ and the $k-\omega$ turbulence models. The SST model has also been applied successfully in axial fan investigations [61].

The details of this model are given in Ref. [56]. The key transport equations for the turbulent kinetic energy k and the dissipation rate ω are:

$$\begin{aligned} \frac{Dk}{Dt} &= P - \beta^* \omega k + \nabla((\nu + \sigma_k \nu_t)\nabla k) \\ \frac{D\omega}{Dt} &= \frac{\gamma}{\nu_t} P - \beta\omega^2 + \nabla((\nu + \sigma_\omega \nu_t)\nabla\omega) + 2(1 - F_1)\frac{\sigma_{\omega 2}}{\omega}\nabla k \nabla\omega \end{aligned} \tag{5.9}$$

Here P is the production rate of turbulence, β^*, β, σ_ω, σ_k and $\sigma_{\omega 2}$ are model constants.

The Spalart-Allmaras (SA) turbulence model is a typical one-equation model originally formulated for aerodynamic applications involving wall-bounded flows. Its principle is based on the resolution of an additional transport equation for the turbulent viscosity. However, it is incapable to predict the decay of turbulence in isotropic turbulence. In low-pressure axial fan research, the SA model has been successfully applied [49]. Its advantages are robustness and lower CPU and memory usage, in comparison to two equation models.

The details of this model are given in Ref. [48]. The key transport equation for the turbulent viscosity is [43]:

$$\frac{D\nu_t}{Dt} = \nabla \cdot \left(\frac{\nu_t}{\sigma_\nu} \nabla \nu_t \right) + S_\nu \tag{5.10}$$

Here σ_ν is a constant, the source term S_ν depends on ν and ν_t, the mean rate of rotation, the gradient of ν_t and the distance to the nearest wall.

The current study focuses on the CFD simulation strategy, the details of turbulence model are not discussed here and can be found in Ref. [43].

5.3 Computational Domain, Boundary Conditions and Mesh Generation

The investigated fan is a rotor-only fan (i.e. no diffuser blades are present) with six identical blades. Considering the circumferential symmetry of the casing and

the symmetry of the blades, it is sufficient to consider only a single blade passage as computational domain when the steady operating range is considered.

In the validation study of the CFD simulation strategy, the shape of the test facility is referred to. As a category A inlet chamber test set up, there is no significant ducting at either the inlet or the outlet of the fan in the test facility. In order to reduce the influence of the imposed boundary conditions at inlet and outlet on the CFD results, the computational domain is extended here by one and two casing diameters upstream and downstream from the blades, respectively.

For ease in grid generation (with good quality), the hub is extended to the outlet. This gives a small blockage in the meridional plane, of 1.84% and 3.38% blockage for the blade with and without non-airfoil part, respectively. The computational domain is shown in Fig. 5.1.

Due to the absence of diffuser blades and the circumferentially uniform inflow conditions, the flow is considered to be steady in the frame of reference that is rotating with the (identical) fan blades.

AutoGrid (part of the NUMECA Fine/Turbo CFD environment) is employed for mesh generation. A cell-centred second-order finite volume approach is applied for the spatial discretization of the governing equations in conservative form. In the present study, the steady RANS flow equations are solved with implicit residual smoothing. Local time-stepping and three-level multigrid techniques are used to accelerate convergence of the solution of the discretised equations. Merkle preconditioning is applied in the compressible-flow code to provide fast convergence for low Mach number flows [63, 133].

In order to make the CFD simulation results comparable to measurements, the boundary conditions should represent actual flow conditions in the experiments as closely as possible. Since a settling screen is present upstream from the fan inlet in the experiments (see Fig. 4.3) and with a well-designed “bell mouth", variations in inlet velocity are expected to be small (see for instance the experimental results in Ref. [61]), the inlet flow can be assumed as being uniform and without pre-swirl and with low turbulence level. Therefore, turbulence quantities such as the turbulent viscosity ν_t in the Spalart-Allmaras turbulence model and the turbulent kinetic energy k and the dissipation rate ϵ in the SST turbulence model are estimated with low-turbulence level relations. For the Spalart-Allmaras turbulence model for internal flows (e.g turbomachinery), it is recommended that ν_t/ν is in the range $1-5$, from low to high turbulence level [78]. For the SST turbulence model, the turbulence intensity Tu for internal flows is recommended to be about 5% and estimates for k and ϵ at the inlet can be obtained from

$$k = \frac{3}{2}\left(\mathrm{Tu}\cdot U_{\mathrm{ref}}\right)^2 \qquad \epsilon = C_\mu \rho \frac{\mu}{\mu_t}\frac{k^2}{\mu}. \tag{5.11}$$

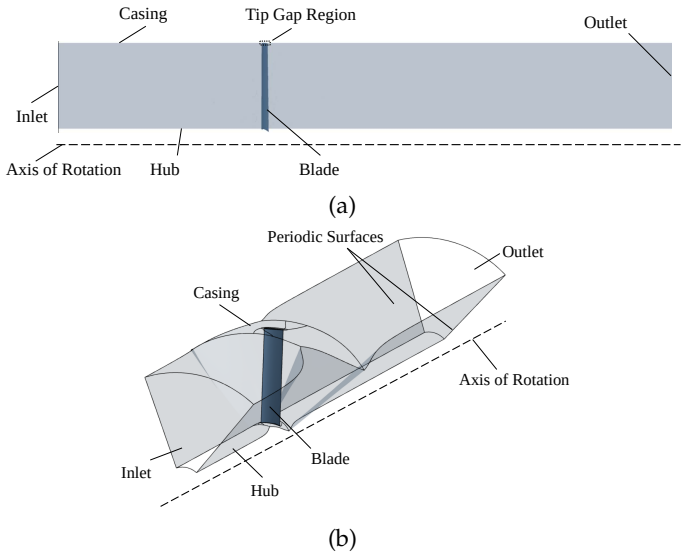

Figure 5.1: Computational Domain: (a) Meridional View, (b) Three-dimensional View.

Here $C_\mu = 0.09$ is a model constant. A typical value for $\mu_t/\mu = 50$ (for internal flows) and the characteristic velocity U_{ref} here corresponds to the streamwise velocity [78].

As measured directly, the total pressure and the volumetric flow rate are prescribed at the inlet and outlet, respectively. Note that the latter boundary condition does *not* imply that the velocity is uniformly distributed. At the outlet, the pressure distribution conforms to the radial equilibrium condition (see for example in Ref. [9]), $\frac{\partial p}{\partial r} = \rho \frac{v_\theta^2}{r}$ where the value of the static pressure p is fixed at some radius r.

At the blade and hub surfaces, the relative flow velocity vector equals zero due to the no-slip condition. The hub surfaces have the same rotational speed as the blades. At the outer casing, the absolute flow velocity vector equals zero. Due to the assumed symmetry in the circumferential direction, periodic boundary conditions are applied in circumferential direction at the corresponding surfaces (see also Fig. 5.1(b)).

5.4 Grid Convergence Study

A grid convergence study has been performed for the baseline Howden fan, in order to assess the numerical accuracy of the CFD simulations and to formulate a guideline for mesh generation with good quality and fairly low computation cost for the considered low-pressure axial fans. According to the guidelines for assessing the accuracy of CFD solutions [79], a set of three grids needs to be considered, with characteristic grid size h (for each of the three grids) defined by

$$h = \left[\frac{1}{N} \sum_{i=1}^{N} \Delta V_i \right]^{1/3} . \tag{5.12}$$

Here ΔV_i is the volume of cell i and N is the total number of cells present in the grid.

Three different multi-block structured grids ("coarse", "medium and "fine"; "c", "m", "f" in short) have been generated for the grid convergence study. The grid quality is based on considerations of skewness angle, aspect ratio and expansion ratio of the cells. The skewness angle should be as close to 90° as possible, while the aspect ratio (possible range: $1-50000$) and the expansion ratio (possible range: $1-100$) should be as small as possible. For the "coarse" grid, the minimum skewness angle is 35.9°, the aspect ratio of more than 98% cells is smaller than 1000 and the maximum expansion ratio is 2.24. Hence, the grid satisfies the quality criteria described in Ref. [134]. All employed grids satisfy the quality criteria described above.

In the guidelines [79], the grid refinement factors h_m/h_f and h_c/h_m are desired to be larger than 1.3 (these factors are $h_m/h_f = 1.30$ and $h_c/h_m = 1.36$). Since the sum of the volumes of the cells in the calculation domain is the same for all grids, the refinement factor for the cell number ratios N_f/N_m and N_m/N_c should be larger than 2.19. These conditions are met by the employed grids, see Table 5.1.

The discretised nonlinear equations have been solved iteratively. A typical convergence history curve of the global residual (i.e. the root mean average squared of the imbalance of the discretised equations for the cells) is shown in Fig. 5.2. A reduction of the global residual by three orders of magnitude is considered to indicate good convergence [78]. Here a much stricter convergence criterion, a reduction by six orders of magnitudes, is employed.

Based on the computed solutions, it has been checked that the near-wall grid resolution is sufficiently fine by determining the dimensionless wall distance $y^+ = U_\tau y/\nu$ (where y is the distance of the first grid point away from the wall and U_τ is the friction velocity). For all simulations, the maximum value $y^+_{max} < 3.3$ and the averaged value $y^+_{avg} < 0.3$. Hence, the first grid point from the wall is located in the viscous sublayer.

Table 5.1: Information on Three Grids.

Grid Level	Coarse	Medium	Fine
Number of Points in Spanwise Direction	41	57	89
Number of Points on Blade to Blade Surface	14223	25479	36063
Total Number of Grid Points	5.8×10^5	1.5×10^6	3.2×10^6

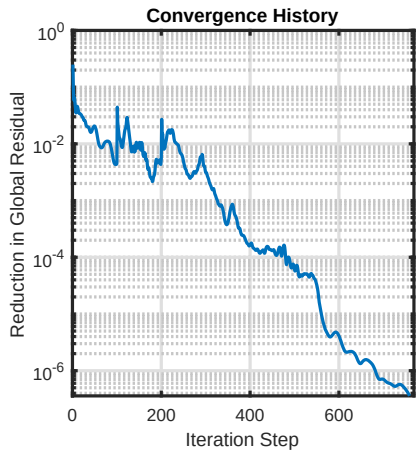

Figure 5.2: Convergence History of the Reduction of the Global Residual (with Respect to the Initial Global Residual) with Iteration Step.

For the grid independence study, the pressure coefficient ψ, the total-to-static efficiency η_{ts} and the power coefficient λ have been selected as key variables, as the focus of this study is on the aerodynamic performance.

Following the method described in Ref. [79] that is based on Richardson extrapolation for the dependence of the key variables on the mesh size h, the discretization errors have been estimated, see Table 5.2 for the flow coefficient φ = 0.156 near Best Efficiency Point (*BEP* for short; based on total-to-static efficiency η_{ts}). Here ϕ_k denotes the value of variable on the k grid, p' is apparent order of the numerical discretisation and ϕ_{ext} is the value extrapolated to zero grid size, $h \to 0$, and GCI_{fine} is grid convergence index for the fine grid.

According to the results in Table 5.2, the numerical uncertainty in the fine-grid solution is 1.25% for the pressure coefficient ψ, 3.6% for the total-to-static efficiency η_{ts} and even smaller for the power coefficient λ, which means that the computational results are (effectively) independent of grid size.

Table 5.2: Grid Convergence Analysis for Flow Coefficient φ = 0.156 near BEP.

Key Variable	ϕ_{coarse}	ϕ_{medium}	ϕ_{fine}	p'	ϕ_{ext}	GCI_{fine}
ψ [-]	0.1000	0.1005	0.1011	1.33	0.1015	1.25%
η_{ts} [%]	57.81	58.19	58.58	0.68	59.87	3.6%
λ [-]	0.0398	0.0398	0.0397	9.47	0.0398	0.0024%

Similar results for the estimated discretisation errors for the off-design flow coefficients φ = 0.105 and φ = 0.229 are given in Table 5.3 and 5.4. Considering the computational costs and limited gains in numerical accuracy, the medium grid size is selected as grid size for the analyses in Chapter 6.

Table 5.3: Grid Convergence Analysis for Small Flow Coefficient φ = 0.105.

Key Variable	ϕ_{coarse}	ϕ_{medium}	ϕ_{fine}	p'	ϕ_{ext}	GCI_{fine}
ψ [-]	0.1328	0.1337	0.1333	3.10	0.1330	0.28%
η_{ts} [%]	54.95	55.26	55.43	1.45	55.81	0.85%
λ [-]	0.0376	0.0376	0.0375	0.77	0.0373	0.77%

Table 5.4: Grid Convergence Analysis for Large Flow Coefficient $\varphi = 0.229$.

Key Variable	ϕ_{coarse}	ϕ_{medium}	ϕ_{fine}	p'	ϕ_{ext}	GCI_{fine}
ψ [-]	0.0231	0.0242	0.0244	5.62	0.0245	0.29%
η_{ts} [%]	21.88	22.98	23.19	5.23	23.26	0.38%
λ [-]	0.0358	0.0357	0.0357	1.70	0.0356	0.25%

Chapter 6

Validation of CFD Simulations

The results reported in this chapter are adapted from the published paper [50]. The research background is introduced in Sec. 6.1, the CFD results for the baseline case with “baseline" variables as indicated in Table 6.2 are described in Sec. 6.2. CFD results investigating the influence of trailing edge shape, non-airfoil part, tip gap size and employed turbulence model are described from Sec. 6.3 to 6.6 to formulate the CFD simulation strategy. The validation of this strategy for a fan with medium hub-to-tip ratio is reported in Sec. 6.7. The main conclusions are given in Sec. 6.8.

6.1 Background

To be able to use CFD simulations to support the design of low-pressure axial fans, it is important to establish their accuracy and to formulate guidelines for such simulations. Here the accuracy of such simulations is evaluated by comparison between measured and computed aerodynamic performance characteristics. The number of CFD studies dealing with the aerodynamic performance of fans with *small to medium* hub-to-tip ratio κ is limited (see for example in Refs. [33, 49, 57, 60, 61]). These studies are discussed in more detail in the following, in the order of decreasing hub-to-tip ratio κ. The dimensionless performance parameters for the fans considered in these studies are summarised in Table 6.1. Note that these studies often focus on more detailed flow phenomena and qualitative effects of blade geometry on various performance parameters, rather than the overall aerodynamic fan performance parameters considered here. Only the current fan is expected to have a backflow region, according to the criterion shown in Fig. 2.4 in Sec. 2.1 and given in Refs. [8, 27]. For fans with small κ, design approaches based on cascade analyses break down due to the significant radial redistribution of fluid. Design methods for fans with small hub-to-tip ratio κ are presented in Refs. [123, 135].

Table 6.1: Dimensionless Fan Parameters (defined in Eqs. (1.3), (1.4) and (1.5)) at Design Conditions.

Reference	Blade Count	κ	φ	ψ	Ma	Re
Current study	6	0.14	0.15	0.10	0.14	4.6×10^5
Wilkinson *et al.* [59]	8	0.29	0.13	0.057	0.17	3.0×10^6
Jin *et al.* [49]	5	0.35	0.23	0.093	0.11	9.9×10^4
Masi *et al.* [60]	10	0.35	0.31	0.073	0.14	1.6×10^5
Beiler & Carolus [33]	6	0.40	0.15	0.15	0.14	7.7×10^4
Zhu & Carolus [61, 62]	5	0.45	0.19	0.16	0.14	7.4×10^4
Vad *et al.* [57, 58]	12	0.6	0.33	0.23	0.13	4.6×10^5

For fans with a fairly large hub-to-tip ratio $\kappa = 0.6$ (and including diffuser blades) the influence of forward skewed blades with a prescribed vortex distribution on the aerodynamic performance of axial fans has been investigated in Refs. [57, 58] by experiments and CFD simulations (using the $k-\epsilon$ turbulence model). The CFD simulations account for the tip gap and the mesh independence of the CFD results has been checked. Besides measured velocities (using hot-wire anemometry) at the design point, the aerodynamic performance has also been estimated. The agreement between measured and computed performance characteristics is labelled fair (10% deviation at the design point) due to limitations in the experimental test set-up [57].

For a fan with medium hub-to-tip ratio $\kappa = 0.45$ the influence of the size of tip clearance s on the aerodynamic and the aeroacoustic performance has been studied experimentally and using RANS CFD simulations (using the SST turbulence model) in Refs. [61, 62], for three tip clearance ratios $s/D_{\text{fan}} = 0.1\%$, 0.5% and 1.0%. The comparison of measured and computed aerodynamic performance (in terms of pressure coefficient ψ, total-to-static efficiency η_{ts} and power coefficient λ as function of the flow coefficient φ) is considered good with 2% deviation at the design flow coefficient for the fans with 0.1% and 0.5% tip clearance ratio; for the fan with 1.0% tip clearance ratio, larger deviations are found for small flow coefficients. Note that the mesh independence of the CFD results has not been checked. Since complete geometrical information is available for these fans [62], these fans have also been considered here.

A design methodology for skewed blades is presented in Ref. [33]. For a fan with medium hub-to-tip ratio $\kappa = 0.4$, experiments and RANS CFD simulations have been performed to verify this methodology. The computational grids used are relatively coarse for present-day standards. The small tip gap has not been accounted for in the CFD-simulations that use the $k-\epsilon$ turbulence model. The flow fields that have been measured (using hot-film probes) at some distance downstream of the fan show that at the design flow rate the axial velocity is

quantitatively well predicted by the CFD simulations; the measured radial and circumferential velocity profiles show qualitative agreement. No direct comparison is presented of overall measured and computed aerodynamic performance characteristics.

Design guidelines for the blade sweep and the vortex distribution are formulated in Ref. [60]. In this study a comparison is also made of experimental and computed aerodynamic performance characteristics (using the $k-\omega$ turbulence model). The grid independence is established qualitatively. Good qualitative agreement is observed. For the three considered fans, good quantitative agreement is observed for either pressure coefficient or efficiency, but not for both simultaneously.

Tip leakage flows in low-pressure axial fans, with hub-to-tip ratio $\kappa = 0.35$ and with circumferentially-skewed blades, are investigated experimentally and using CFD simulations (employing the Spalart-Allmaras turbulence model) in Ref. [49]. The grid independence has been investigated, showing some dependence of the spanwise pressure rise on the employed grid size. The predicted pressure coefficient shows good qualitative agreement with the measured pressure coefficient, with 5% deviation at the design point. Unfortunately, results are neither shown for the total-to-static efficiency η_{ts} nor for the power coefficient λ.

The influence of the tip gap on the aerodynamic performance has been studied experimentally and using CFD simulations for a fan with $\kappa = 0.29$ for flow rates near the design point in Ref. [59], for tip clearance ratios $s/D_{fan} = 0.31\%$, 0.26% and 0.39%. In the CFD simulations the realisable k-ϵ turbulence model has been employed. The authors state that the experimental and CFD predictions correlate well for the pressure coefficient and reasonably well for the total-to-static efficiency.

The focus of the current study is on a fan with very small hub-to-tip ratio $\kappa = 0.14$ (much smaller than for the studies discussed above and listed in Table 6.1) for which a region of backflow is expected [8, 27]. For the considered (Howden) fan a complete description of the fan blade geometry is available as described in Sec. 4.1, in combination with the tip gap size. Part of the blade near the hub has a shape that is not aerodynamically shaped.

Three-dimensional RANS CFD simulations have been performed with Numeca Fine/Turbo software [78], where the grid independence has been thoroughly investigated as described in Sec. 5.4. Computational predictions of the aerodynamic performance have been compared against high-quality measurement data. In this comparison both the dimensionless fan pressure rise ψ and the total-to-static efficiency η_{ts} are considered.

The ultimate aim of this study is to develop a CFD simulation strategy with which accurate predictions can be obtained for low-pressure axial fans with small

hub-to-tip ratio κ. Specific objectives of this study with respect to the aerodynamic performance of low-pressure axial fans with small hub-to-tip ratio κ are to:

- Assess the accuracy of RANS-based CFD simulations;
- Study the influence of the shape of the trailing edge blade sections (sharp vs. rounded);
- Study the influence of the presence of non-aerodynamically shaped parts of the blades;
- Study the influence of the tip gap size;
- Study the influence of the employed turbulence model.

Note that the current study only focusses on the aerodynamic performance for flow rates far from stall conditions. The more complex aeroacoustic performance is not considered here (see for example in Refs. [49, 61, 62, 136]). Methods for extending the stall characteristics are described in Refs. [35, 137].

For the low-pressure axial fan that forms the focus of this thesis, the Mach number is 0.14 and the Reynolds number is 4.6×10^5 (both dimensionless numbers are defined in Eq. (1.4)), so the flows can be regarded as being incompressible and turbulent. The medium is considered as air (real gas; ideal gas with specific heat dependent on temperature).

The influence on the predicted aerodynamic performance characteristics of the items listed in Table 6.2 are specifically investigated here. For each item, two possibilities are considered that are labelled as “baseline" and “alternative" in this Table. For this baseline case, a grid convergence study has been performed whose results are reported Sec. 5.4.

Table 6.2: Investigated Variables.

Item	Baseline	Alternative
Trailing Edge Shape	Sharp	Rounded
Non-airfoil Blade Root	Not Included	Included
Tip Gap	Not Included	Included
Turbulence Model	Spalart-Allmaras	SST

For the fan with small hub-to-tip ration $\kappa = 0.14$, CFD results are shown here for the baseline case in Sec. 6.2, with “baseline" variables as indicated in Table 6.2. In addition, the CFD results that are analysed here focus on the influence on the predicted aerodynamic performance of the following factors. The influence of the trailing edge shape (sharp vs. rounded) is analysed in Sec. 6.3. The influence of part of the blade not having an aerodynamic shape near the root of the blades (indicated as non-airfoil part in Fig. 4.2) is analysed in Sec. 6.4. To the best of the

authors' knowledge, the influence of this non-airfoil part of the fan blades on the aerodynamic performance has not been studied in literature. Sec. 6.5 considers the influence of the tip gap and Sec. 6.6 that of the employed turbulence model. Note that the first three factors involve modelling of the blade geometry, while the other involves flow (turbulence) modelling.

CFD results have been obtained for a number of flow coefficients. In the following, the procedure used to display the aerodynamic performance curves consists of: (i) showing by markers the computed data points consisting of flow coefficient and pressure coefficient and (ii) showing by solid lines a spline interpolation through these data points. This is done to clearly show the trends in the performance curves. An analogous procedure is followed for the total-to-static efficiency.

6.2 Baseline Case

The CFD simulations with variables shown as "baseline" in Table 6.2 form the reference case for subsequent CFD simulations. For this reference case, the predicted aerodynamic performance is shown in Fig. 6.1.

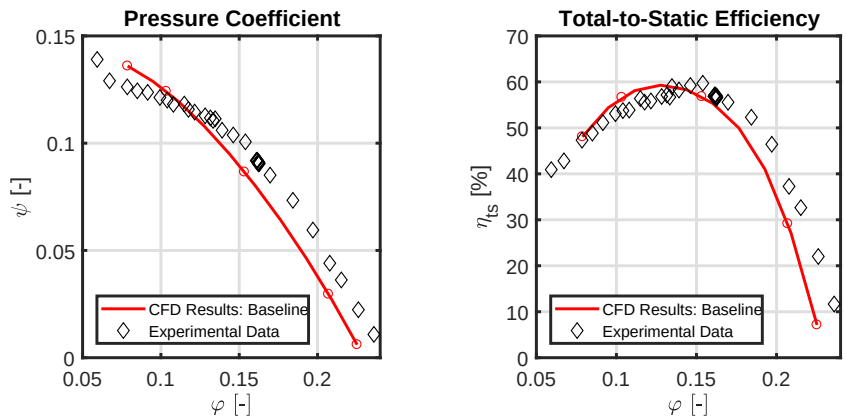

(a) $\varphi - \psi$ (b) φ - η_{ts}

Figure 6.1: Comparison of Measurements and CFD Predictions for the Baseline Case: (a) Pressure Coefficient ψ and (b) Total-to-static Efficiency η_{ts}.

As shown in Fig. 6.1(a), the predicted pressure coefficients ψ are lower than the experimental results, especially for large flow coefficients φ (with a maximum

deviation of 52% at $\varphi = 0.229$). For small φ, near the stall region, the agreement is reasonably good.

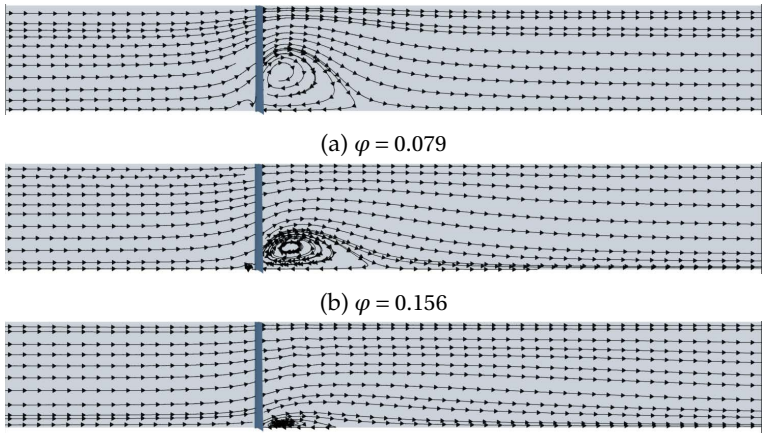

(a) $\varphi = 0.079$

(b) $\varphi = 0.156$

(c) $\varphi = 0.229$

Figure 6.2: Streamlines in the Meridional Plane for the Reference Case for Different Flow Coefficients: (a) $\varphi = 0.079$; (b) $\varphi = 0.156$ (near BEP); (c) $\varphi = 0.0229$. The fan blades are indicated by the solid grey rectangles.

The results for the total-to-static efficiency η_{ts} are shown in Fig. 6.1(b). The predicted results are lower than the experimental results and the largest deviation (compared with experimental data) is 50% at $\varphi = 0.229$. The maximum predicted (by CFD) total-to-static efficiency η_{ts} is 59% at $\varphi = 0.13$, while the experimental maximum η_{ts} is 60% at $\varphi = 0.154$. The maximum predicted total-to-total efficiency $\eta_{tt} = Q \cdot \Delta p_0 / P_{shaft}$ (from CFD; no experimental data are available for η_{tt}; all velocity components are accounted for in the dynamic pressure p_0) is 80.7% at $\varphi = 0.18$.

For the power coefficient λ (data not shown), the deviation equals 14% at BEP, being even larger for large flow coefficients φ. Overall, these CFD simulations of the reference case do not satisfactorily quantify the aerodynamic performance of the investigated fan.

In order to gain additional understanding of the performance of this fan, the flow fields have been analysed. As indicated in Sec. 2.1, backflow regions [8] are expected for this fan. This is confirmed by the current CFD results, see the streamlines in the meridional plane depicted in Fig. 6.2, for flow coefficients $\varphi =$ 0.079, 0.156 and 0.229. As expected, the extent of the backflow region decreases with increasing flow coefficient φ. For the lower flow coefficients, the vortex

downstream of the blades occupies a significant part of the flow path (for φ = 0.156 nearly 40% based on its radial extent).

The streamlines (based on the relative velocity) in the blade-to-blade plane are shown in Fig. 6.3 at different spanwise locations (hub, midspan and tip) near BEP. The flow is attached to the blades, except near the hub.

The vortex distribution, $r\overline{v}_{\theta 2}(r)$ (with $\overline{v}_{\theta 2}$ the circumferentially-averaged circumferential component of the absolute velocity downstream of the blades), see also Sec. 2.7, is important for the distribution of the energy transfer from blades to fluid, as follows from the Euler relation (Eq. (2.11)). The CFD-results near BEP have been used to compute the vortex distribution. The result shown in Fig. 6.4 demonstrates that the vortex distribution strongly differs from a free-vortex design, for which $r\overline{v}_{\theta 2}(r)$ = const.

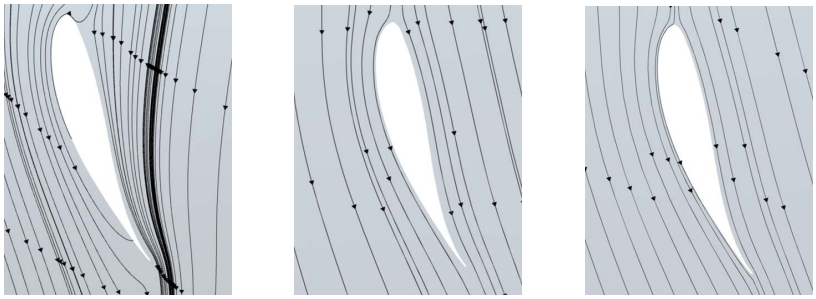

(a) Hub (b) Middle (c) Tip

Figure 6.3: Velocity Streamlines based on the Relative Velocity in the Blade-to-blade Plane at Different Spanwise Locations for the Reference Case: (a) near Hub, (b) Mid-span and (c) near Tip. Results for φ = 0.156 near BEP.

6.3 Influence of Trailing Edge Shape

In classical airfoil theory the trailing edge shapes considered are sharp (or cusp-shaped with zero thickness), as this enforces both the location of the rear stagnation point and the local direction of the flow. However, for strength considerations, actual trailing edge shapes are different. Hence, two trailing edge shapes are considered, the sharp trailing edge conforming to the Wortmann profile and the rounded trailing edge conforming to the actual geometry, see Fig. 6.5(a). A zoom-in on the trailing edge region in Fig. 6.5(b) shows the (small) difference between the sharp and rounded trailing edge shapes.

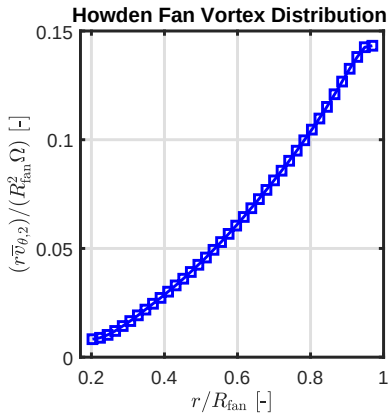

Figure 6.4: Vortex Distribution of Investigated Fan for $\varphi = 0.156$, near BEP for the Reference Case.

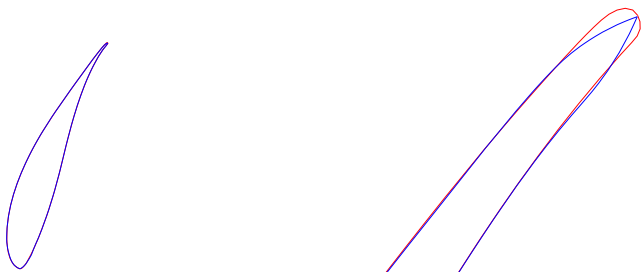

(a) Airfoil Section: Wortmann profile with Sharp Trailing Edge [129] and Actual Profile

(b) Sharp and Rounded Trailing Edge

Figure 6.5: Shape of Airfoil Section and of Trailing Edge, for Sharp (Blue Curve) and Rounded (Red Curve) Trailing Edge Shapes.

CFD simulations with these two trailing edge shapes have been performed, using the conditions shown as “baseline" in Table 6.2. The employed grids have (approximately) the same size and grid quality. Note that in these CFD simulations the tip gap has not been taken into account.

The predicted aerodynamic performance for the two trailing edge shapes is shown in Fig. 6.6. Although the difference in blade section geometry is rather small, the predicted aerodynamic performance is significantly different.

As shown in Fig. 6.6(a), the CFD simulations with the rounded trailing edge

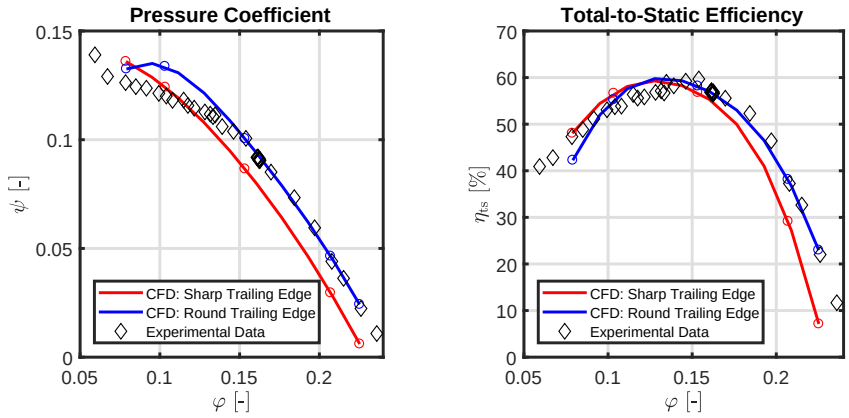

(a) $\varphi - \psi$ (b) φ - η_{ts}

Figure 6.6: Comparison between Measurements and CFD Predictions with Sharp and Rounded Trailing Edge Geometry: (a) Pressure Coefficient ψ and (b) Total-to-static Efficiency η_{ts}.

(much) better predict, compared with reference case with sharp trailing edge, the pressure coefficient ψ over the full range of considered flow coefficients φ, especially at high φ.

For the total-to-static efficiency η_{ts}, the results shown in Fig. 6.6(b) for the reference case and for the rounded trailing edge are nearly the same for flow coefficients φ near BEP, and in agreement with experimental results. For higher φ, the CFD prediction for η_{ts} with the sharp trailing edge is lower than that with the rounded trailing edge geometry. The latter is higher than the measured efficiency.

For the power coefficient λ (data not shown), the prediction with the rounded trailing edge case shows good agreement with measurements with 3% deviation at BEP, while for the sharp trailing edge case, the deviation equals 14% at BEP and is even larger for large flow coefficients.

Thus, the influence of the trailing edge shape on the CFD predictions of the aerodynamic characteristics is significant. The use of the actual, rounded trailing edge shape yields CFD predictions that overall are in much better agreement with the experimental aerodynamic performance characteristics.

To investigate the origin of these differences, the flow field is visualised around the trailing edge where the two geometries differ, see Fig. 6.7 at midspan for flow coefficient $\varphi = 0.156$ near BEP. With the sharp trailing edge, flow separation is predicted at the suction side near the trailing edge, while for the rounded trailing edge the extent of the separation is much smaller. The streamlines in the meridional plane with the rounded trailing edge for $\varphi = 0.156$ (data not shown) are very

similar to those with the sharp trailing edge that are displayed in Fig. 6.2.

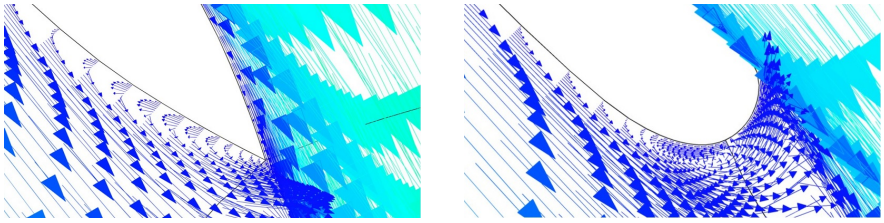

(a) Sharp Trailing Edge (b) Rounded Trailing Edge

Figure 6.7: Relative Velocity Vector Field in the Blade-to-blade Plane near the Trailing Edge at Mid-span Location for Flow Coefficient $\varphi = 0.156$ near BEP.

6.4 Influence of Nonaerodynamic Shape

The considered fan has non-airfoil blade sections near the root (see Fig. 4.2(b)). The influence of such non-airfoil sections on the aerodynamic performance characteristics is investigated by comparing CFD results for the case that accounts for the presence of the non-airfoil sections with the case where only the “main blade" is represented. The hub diameters for these two cases are $D_{\text{hub}} = 0.250m$ and $0.339m$, respectively.

CFD simulations of these two blades have been performed, with rounded trailing edge, and where other settings shown as “baseline" in Table 6.2 have been employed. The employed grids have (approximately) the same size and grid quality.

The CFD predictions for the aerodynamic performance characteristics of fan blades with and without non-airfoil sections near the root are shown in Fig. 6.8.

When accounting for the non-airfoil blade root, both pressure coefficient ψ and total-to-static efficiency η_{ts} from the CFD simulations are smaller than for blades without the non-airfoil root over the whole range of flow coefficients φ. As for the power coefficient λ (data not shown), nearly the same predictions have been obtained for these two cases, with the largest deviation of 2.1% near flow coefficient $\varphi = 0.105$.

To investigate the origin of the difference in the aerodynamic performance between these two blades, especially for small flow coefficients φ, the streamlines in the meridional surface for $\varphi = 0.105$ are shown in Fig. 6.9. The downstream backflow region for the blade with the non-airfoil sections near the root is larger than that for without the non-airfoil sections. Also visible in Fig. 6.9(b) is that

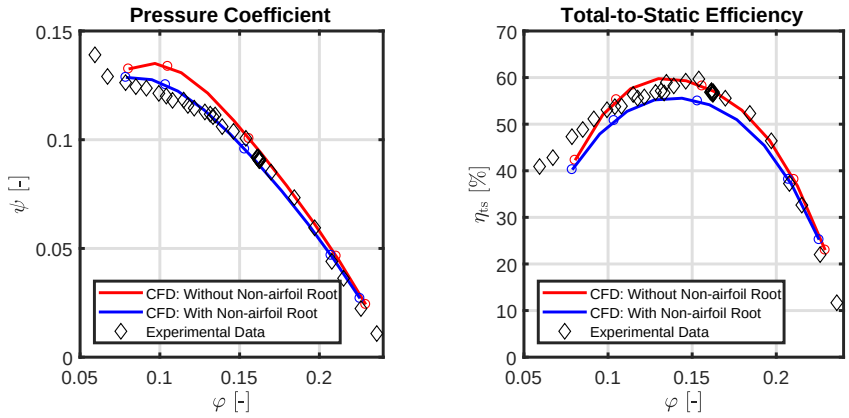

(a) $\varphi - \psi$ (b) φ - η_{ts}

Figure 6.8: Comparison of Measurements and CFD Predictions with and without Non-airfoil Blade Sections near Root: (a) Pressure Coefficient ψ and (b) Total-to-static Efficiency η_{ts}.

upstream of the blades a vortex is present near the hub for the blades with non-airfoil sections near the root. The presence of this vortex is considered to result in larger secondary flow losses and lower static pressure increases. For larger flow coefficient $\varphi = 0.229$ the upstream vortex effectively is not present, and the extent of the downstream backflow region is reduced.

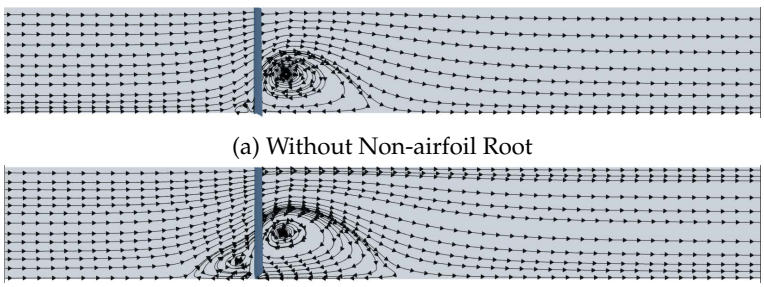

(a) Without Non-airfoil Root

(b) With Non-airfoil Root

Figure 6.9: Comparison of Meridional Surface Streamlines: (a) Without Non-airfoil Blade Sections near Root; (b) With Non-airfoil Blade Sections near Root; Both for flow coefficient φ = 0.105.

6.5 Influence of Tip Gap Size

It is well-known (see for instance [38, 138, 139]) that the size of the tip gap affects the aerodynamic performance, due to the tip leakage flow from pressure side to suction side that results in the formation of a tip vortex and in blockage. Using LES simulations, tip leakage flows have been studied in Ref. [42].

An increase of the tip gap results in a decrease of pressure rise and efficiency [38, 85, 139], and more severe stall [140, 141]. The tip gap is accounted for in some CFD studies of low-pressure axial fans [49, 57, 59–61, 72, 76], but ignored in others [33, 60, 76, 136]. For low-pressure axial fans, CFD simulations with different tip gaps have been reported [61]. Their results show that the deviations between CFD predictions and measurements increase with increasing tip gap.

Here CFD simulations with and without tip gap are performed (with the rounded trailing edge and excluding the non-airfoil blade sections near the root) to investigate the influence of the tip gap size on the predicted aerodynamic performance of the fan with small hub-to-tip ratio κ. The multi-block structured grid in the tip gap is composed of an H and an O grid. There are 17 points and 13 points in the spanwise and azimuthal direction, respectively, with 193 points and 81 points wrapping around the O and the H grid. The number of grid points in the tip gap region is sufficiently large according to Ref. [49]. The sensitivity of the grid resolution in the tip gap region has been explored by generating grids with 13 as well as 17 points in spanwise direction. The CFD results show that the largest deviation in the predicted aerodynamic performance with these two tip gap grid resolutions is 1.4% in the total-to-static efficiency.

The predicted pressure coefficient ψ and the total-to-static efficiency η_{ts} are shown in Fig. 6.10 and the predicted power coefficient λ is shown in Fig. 6.11. As expected, the pressure coefficient ψ, the total-to-static efficiency η_{ts} and the power coefficient λ decrease with increasing tip-gap ratio s/D_{fan}. The difference in λ between the blade with 0.22% tip gap ratio and the blade without tip gap is small. The influence of the tip gap size becomes smaller with increasing flow coefficient φ.

Quantitatively, for the actual tip gap ratio of 0.43% in the measurements, the CFD results are quantitatively significantly different (both for pressure rise ψ and total-to-static efficiency η_{ts}) from measured values. Unusually and unexpectedly, CFD simulations significantly *underpredict* the aerodynamic performance in this case.

The meridional streamlines show that tip recirculation and a backflow region near the hub are present for the cases of 0.43% and 0.22% tip gap ratio when $\varphi = 0.156$ (data not shown). These flow phenomena result in blockage.

The meridional streamlines with 0.43% and 0.22% tip gap ratio for $\varphi = 0.156$ indicate (data not shown) that tip recirculation is present as well the backflow

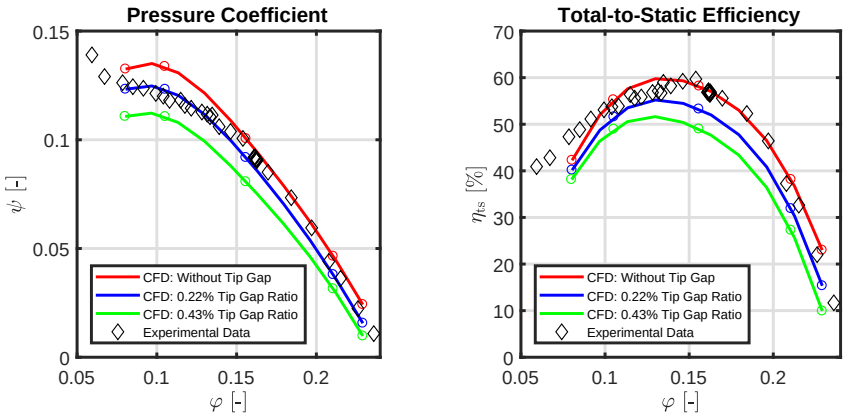

(a) $\varphi - \psi$ (b) φ - η_{ts}

Figure 6.10: Dependence of Pressure Coefficient ψ and Total-to-static Efficiency η_{ts} on Flow Coefficient φ: Measurements, CFD Simulations with Different Sizes of the Tip Gap and without Tip Gap. Note that in the experiments the tip gap ratio equals 0.43%.

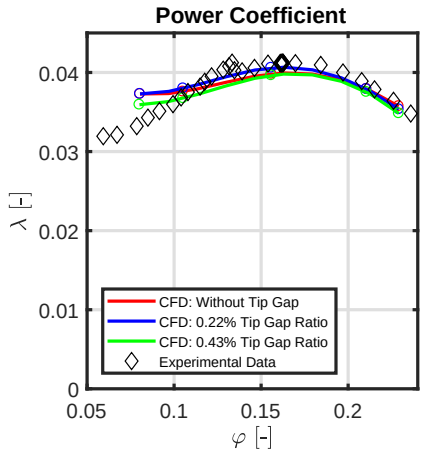

Figure 6.11: Dependence of Power Coefficient λ on Flow Coefficient φ: Measurements, CFD Simulations with Different Sizes of the Tip Gap and without Tip Gap. Note: Tip gap ratio equals 0.43% in the Experiments.

region near the hub, resulting in blockage.

The streamlines in four streamwise cut planes near the tip area are shown in Fig. 6.12 (viewed from downstream of the blade) for these two tip gap ratios. The red dashed lines refer to the boundary of each cut plane, numbers of “1" to “4" refer to the location from near the leading edge to near the trailing edge. The tip vortex starts from the blade leading edge, appears at mid location of the blade and further develops at the trailing edge and downstream of it. The vortex region increases significantly in size with larger tip gap ratio, which results in larger blockage and losses.

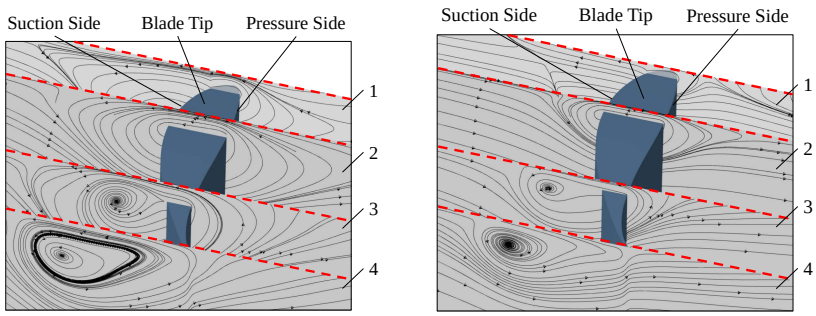

(a) 0.43% Tip Gap Ratio (b) 0.22% Tip Gap Ratio

Figure 6.12: Surface Streamlines at Four Streamwise Cut Planes (“1" to “4", from leading edge towards trailing edge): (a) Blade with 0.43% Tip Gap Ratio; (b) Blade with 0.22% Tip Gap Ratio. Both at flow coefficient $\varphi = 0.156$, near BEP.

Based on the current results, CFD simulations for the fan with small hub-to-tip ratio κ can not adequately predict the influence of the tip gap on the aerodynamic performance. Accordingly, for use of CFD within an industrial context, it is recommended not to take the tip gap into account. Then quantitatively good agreement can be obtained between CFD predictions and experiments for the fan considered here in detail. In a scientific context, CFD simulations accounting for the tip gap need to be studied in (much) more detail.

6.6 Influence of Employed Turbulence Model

For the required turbulence model, there is no definite answer as to which model is the most suitable in general for low-pressure axial fan CFD simulations. The influence of the turbulence model on CFD predictions has been studied in Ref. [76] for different variants of the k-ϵ turbulence model.

The Spalart-Allmaras turbulence model [48] has been initially applied here, based on considerations of low computational cost and successful use in investigations of axial flow fans [49]. The SST turbulence model is a two-equation model that combines advantages of the Wilcox $k-\omega$ model and the $k-\epsilon$ model. It has improved capability for flow predictions involving separation [61]. Hence, the SA and SST turbulence models have been selected to investigate the influence of the turbulence model on the predicted aerodynamic performance of the axial fan with small hub-to-tip ratio κ. CFD simulations with the rounded trailing edge shape and the main blade without tip gap have therefore been performed.

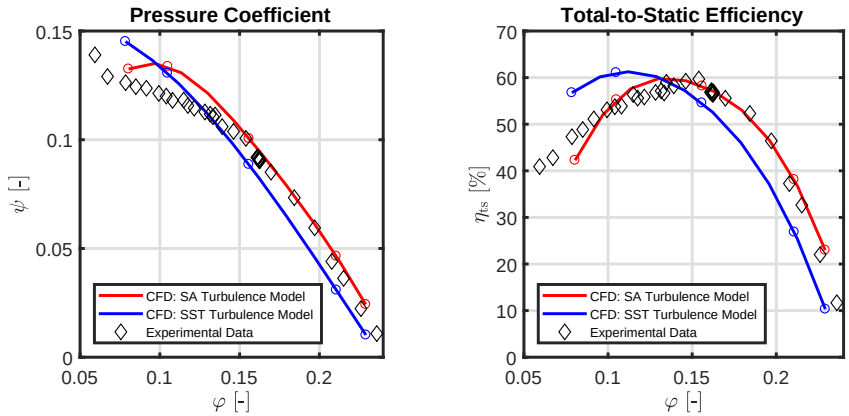

(a) $\varphi - \psi$ (b) φ - η_{ts}

Figure 6.13: Dependence of Pressure Coefficient ψ and Total-to-static Efficiency η_{ts} on Flow Coefficient φ: Measurements, CFD simulations with SST and SA turbulence models.

The CFD results are shown in Fig. 6.13. The SST-model predicts a lower pressure rise ψ (except near stall conditions) than the SA-model. The results with the SA-model agree well with experimental results. With respect to the total-to-static efficiency η_{ts}, the results with the SST-model overpredict and underpredict η_{ts} for small and large φ, respectively. The SST-model underpredicts the power coefficient λ over the whole range of φ (data not shown), with a deviation of 9% at BEP in comparison to the measurements. The results with the SA-model are in much better agreement with the experimental aerodynamic performance.

An investigation of the flow fields shows that the SST-model predicts much larger backflow regions than obtained with the SA-model. The meridional surface streamlines are shown in Fig. 6.14. Compared with the streamlines with the SA-model shown in Fig. 6.2, the backflow region downstream of the blades is larger, corresponding to larger losses.

For a more detailed comparison the (circumferentially-averaged) total and static pressures have been compared at different axial locations. Upstream of the blades these are the same for both turbulence models. Downstream of the blades the total pressures are almost equal, but at an axial distance $0.5D_{\text{fan}}$ downstream of the blades the SA-model predicts a higher static pressure than the SST-model. This means that the predicted velocity distributions are different, corresponding to the larger predicted backflow region with the SST-model.

Overall, the use of the Spalart-Allmaras turbulence model is recommended for CFD simulations of axial fans with small hub-to-tip ratio, as it gives much better agreement with the experimental results for the fan considered here in detail. Note that this sensitivity of the CFD predictions to the employed turbulence model is not noted for the fan with medium hub-to-tip ratio $\kappa = 0.45$ [62, 80], see Sec. 6.7.

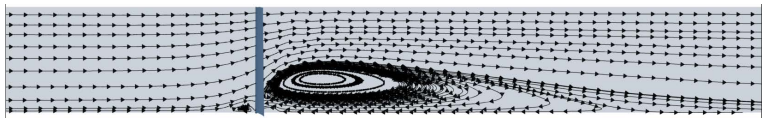

Figure 6.14: Meridional Streamlines: SST Turbulence Model ($\varphi = 0.156$).

6.7 Validation of CFD Strategy for a Fan With Medium Hub-to-Tip Ratio

To verify that the employed CFD simulation techniques are adequate for the simulation of low-pressure axial fans with *medium* hub-to-tip ratio κ (rather than the fan with the low κ that is the focus of the current study), CFD simulations have been performed of the US17 fan that is fully described in Ref. [62] and Sec. 4.4. For this fan with $\kappa = 0.45$, full geometrical data and high-quality measured aerodynamic characteristics are available from Refs. [62, 80], other dimensionless fan parameters are given in Table 6.1.

The flow around the blade with 0.1% tip clearance ratio is simulated, following the approach described in Chapter 5. The fluid type is air (real gas) and the Spalart-Allmaras and the SST turbulence models are both considered. The multi-block structured grid is generated with AutoGrid and the total number of grid points is 1.22×10^6. The minimum skewness angle is 21.42°. The aspect ratio of nearly all cells is smaller than 1000 and the maximum expansion ratio is 3.8. Hence, the grid satisfies the quality criteria given in Ref. [134] and explained in Sec. 5.3.

The convergence criterion for the iterative solution of the discretised equations is a reduction of the global residual by at least three orders of magnitude. The convergence history curves with the SA and the SST turbulence model for a flow coefficient φ near BEP are shown in Fig. 6.15, indicating that good convergence is obtained with both turbulence models.

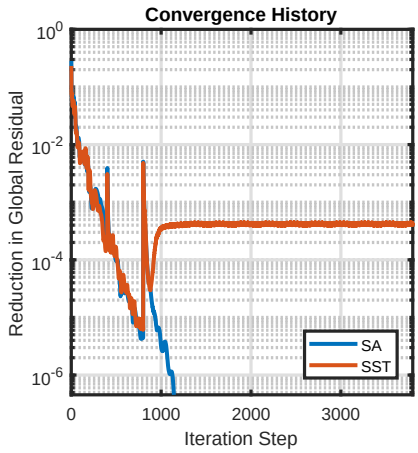

Figure 6.15: Convergence History Curves: SA and SST turbulence model.

The CFD predictions for the aerodynamic performance characteristics for this fan are shown in Fig. 6.16. The predictions with both turbulence models show good agreement with measurements. For the pressure coefficient ψ, results with the SA and the SST turbulence models are nearly the same and higher than the experimental data, except at the lowest flow coefficient φ near stall. Near BEP, the deviation from measurements with both models is 2.3%. For the total-to-static efficiency η_{ts}, except at the lowest flow coefficient φ, all predictions are higher than measurements, the prediction of SST model is 4% higher near BEP. For the power coefficient λ (data not shown), the deviation with the SA model near BEP is 0.7%; the SST model underpredicts the power coefficient λ, with the largest deviation of 4% at BEP. Thus, the aerodynamic performance characteristics can be well predicted with both turbulence models.

The meridional surface streamlines predicted when using the SA turbulence model near BEP ($\varphi = 0.16$) are shown in Fig. 6.17. As expected, no backflow region downstream of the fan is observed in the CFD simulation results.

Concluding, the employed simulation techniques are also adequate for CFD simulations of low-pressure axial fans with medium hub-to-tip ratio, here with $\kappa = 0.45$.

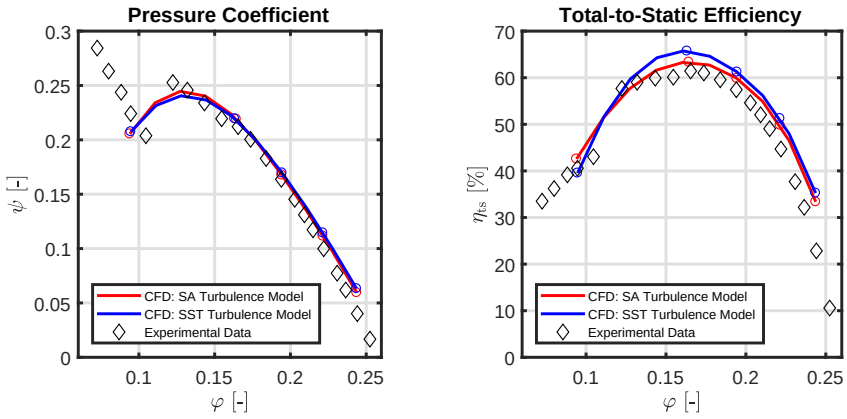

(a) $\varphi - \psi$ (b) φ - η_{ts}

Figure 6.16: Comparison of Measurements and CFD Predictions of US17 Fan: (a) Pressure Coefficient ψ and (b) Total-to-static Efficiency η_{ts}.

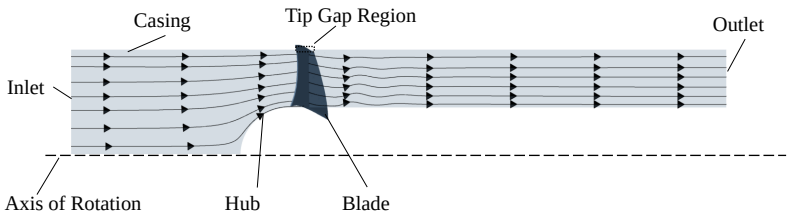

Figure 6.17: Meridional Surface Streamlines for the US17 Fan with $\varphi = 0.16$ near BEP; Results using SA turbulence model.

6.8 Conclusions

Although CFD simulations are widely used in the design of turbomachinery, for axial fans attention has been limited to fans with medium to large hub-to-tip ratio κ. The current study therefore focuses on a RANS CFD simulation strategy for fans with a small hub-to-tip ratio κ. Using reliable measurements of the aerodynamic performance of an axial fan with small hub-to-tip ratio and a complete geometrical description of the fan, many CFD simulations have been performed and analysed in order to investigate the influence of a number of parameters, ultimately aimed at formulating a strategy and guidelines for obtaining accurate CFD predictions of the aerodynamic performance (pressure coefficient ψ *and* total-to-static efficiency η_{ts}) for such machines.

The trailing edge shape (sharp vs. rounded) has a large influence on the predicted aerodynamic performance. The actual trailing edge geometry (rounded in this case) should be used in the CFD simulations for improved agreement with the experimental aerodynamic performance.

The current results show that the presence of non-airfoil sections near the root has a minor influence on the pressure coefficient and hence on the total-to-static efficiency, due the formation of a vortex upstream from the blades near the hub. Overall, the “main blade" part well represents the aerodynamic performance.

With increasing tip gap ratio, the pressure coefficient and the total-to-static efficiency decrease. The CFD simulations with the actual tip gap ratio present in the experiments do not adequately predict the influence of the tip gap on the aerodynamic performance. For use of CFD simulations within an industrial context, it is recommended not to take the tip gap into account, as then quantitatively good agreement is obtained between CFD predictions and experiments.

CFD simulations employing the SST turbulence model significantly underpredict the aerodynamic performance in comparison to the experiments, while those using the SA model yield much better agreement. Therefore, the use of the SA turbulence model is recommended for CFD simulations of axial fans with small hub-to-tip ratio.

For future studies it is recommended to: (i) perform detailed flow measurements (velocity and pressure distributions) for detailed validation of CFD simulations, (ii) account for the actual hub shape downstream of the fan (bulb-shaped; not extended to the outlet as in the current CFD simulations) present in the experiments, (iii) study in more detail the influence of the tip gap on the aerodynamic performance, (iv) consider the influence of the outflow region on the aerodynamic performance and (v) perform CFD simulations for other fan types with small hub-to-tip ratios.

Chapter 7

Effect of Blade Skew on Aerodynamic Performance

The results reported in this chapter are adapted from the published paper [93]. The research background is introduced in Sec. 7.1, the CFD results of axial fan blades with sweep, dihedral, axial skew and circumferential skew are described in Sec. 7.3. An overview of skew effects is discussed in Sec. 7.4, and the main conclusions are given in Sec. 7.5.

7.1 Research Background

Classical design methods for axial fans [8, 9, 11, 21, 27] (see also Chapter 2) are usually based on two-dimensional considerations of lift and drag coefficients of blade airfoil sections (see Sec. 2.5), cascade analyses (see Sec. 2.6) and radial equilibrium conditions (see Sec. 2.7) to determine the stagger angles of the two-dimensional blade sections at various radial locations. To obtain the three-dimensional blade geometry, the two-dimensional airfoil sections are stacked along a specific line, the so-called stacking line (see Sec. 2.8).

In conventional design methods, the simplest radial stacking line is applied, which means that the stacking points lie on a radially-directed straight line. Early research about three-dimensional stacking has been performed by Godwin [82] on compressor blades, while the first investigation for axial fan blades was by Mohammed et al. [83]. Later investigations on three-dimensional stacking lines are generally expressed in terms of sweep, dihedral and skew. The concept of sweep was initially introduced by Busemann [28] in 1935 in aircraft wing design to enhance drag reduction at transonic speed [29]. For a wing with sweep the airfoil sections are shifted in the chord direction, while with dihedral the airfoil sections are shifted in the direction perpendicular to the chord direction. Skew is a more general term, encompassing sweep as well as dihedral.

In wing aerodynamics [29, 142], sweep is considered to lead to a reduction of the lift coefficient and the slope of the lift curve (with respect to that of the unswept wing) by a factor $\cos\gamma$, where γ is the sweep angle (in radians). The effect of dihedral is investigated in Ref. [143] and the corresponding lift reduction factor is $\cos^2\gamma$. A reduction in lift coefficient leads to reduced flow turning [144]. For axial fans, a similar $\cos\gamma$ effect has been reported [33, 83, 89].

For axial fans, the chord direction dictates sweep and dihedral (as for wings), while the absolute inflow and blade rotation directions dictate axial and circumferential skew, respectively [31–33]. Forward and backward sweep mean that the blade section is shifted upstream and downstream, respectively, in the relative flow field. Forward and backward dihedral and axial skew mean that the blade section is shifted upstream or downstream, respectively, of the baseline blade section in the absolute flow field. Forward or backward circumferential skew mean that the blade section is shifted in the direction of rotation or opposite, respectively. Abbreviations for the various types of blade skew are summarised in Table 7.1.

Table 7.1: Abbreviations for Types of Blade Skew

	Forward	Backward
Sweep	FSW	BSW
Dihedral	FDH	BDH
Axial Skew	FAS	BAS
Circumferential Skew	FCS	BCS

Mohammed et al. [83] first investigated the effects of sweep on axial fan performance for an impeller with hub-to-tip diameter ratio $\kappa = 0.5$. Their experimental data indicate that the blades with *FSW* operate more efficiently than baseline (unswept) blades at low flow coefficients, while for large flow coefficients the performance of all cases is almost the same. With respect to flow fields, *FSW* is found to affect the blade surface velocity distribution mostly at the tip on the suction side; nearly no effects are observed at hub and mid sections. For *FSW*, a reduction of accumulation of boundary layer flow near the tip is also found.

Subsequent investigations of the effects of sweep, dihedral and skew reported beneficial effects, such as improvement of efficiency (η_{ts} or η_{tt}), reduction of endwall (hub and shroud) and tip gap losses and control of secondary flow (radial flow). Most of these advantages are found for forward types [84].

Since any shift of a blade section can be decomposed into two mutually perpendicular directions (for example, sweep can be decomposed into axial and circumferential skew), some of these benefits have common origins. Therefore, *FSW* and *FCS* are often investigated together, as in Refs. [33, 84].

A simplified explanation of the effects of forward skewed blade effects on the velocity distribution is as follows. For *FSW* (and *FDH*, *FCS*, *FAS*) the blades near the tip protrude into the upstream flow and are able to perform work on the fluid in advance. Radial equilibrium considerations show that this leads to locally increased axial velocities near the tip and lower axial velocities near the hub. These changes in velocity fields affect flow angles, lift and vortex distributions ($r\,v_{\theta 2}$) of each blade section, resulting in changed overall performance. The secondary flow downstream of blades is found to decrease (increase) by forward (backward) blade sweep, respectively [34].

Inside the blade passage, a reduction of radial accumulation of low-momentum fluid in boundary layers at the suction side surface is frequently reported [35, 89–91] as the main benefit (in aerodynamic performance) from *FSW* and *FCS*. This radial migration induced by forward swept blades is illustrated in Refs. [84, 85, 92], showing that for forward swept blades the flow path of radially outward flow near the blade surface is shortened. This is confirmed by the measured pressure distribution in Refs. [83, 90] and the streamlines from Computational Fluid Dynamics (*CFD* for short) simulations in Refs. [89, 91] near the blade suction side surface. Therefore, the accumulation of low-momentum fluid near the tip is reduced, and the associated reduction of end-wall and the tip losses both contribute to the improvement of efficiency [35]. A reasoning analogous to the one that explains the benefits of forward-swept blades shows that backward-swept blades are less favourable for improvement of aerodynamic performance [89].

Yet, there is no universal conclusion on how these blade shapes can influence the aerodynamic performance for all axial fan blades, as noted by Vad in his remarkable overviews [84, 85]. In comparison to a baseline case, *FSW* gave an increased η_{tt} in Ref. [35], unchanged η_{ts} in Ref. [33] and decreased η_{tt} in Ref. [36]. For *BSW*, studies reported increased η_{tt} in Ref. [37] as well as decreased η_{tt} in Ref. [36]. Note that these results have been reported for different blades and different flow coefficients.

With respect to dihedral, effects similar to those for sweep (efficiency gain [31, 86], reduction of tip losses and unloading of the tip [88]) have been reported. Furthermore, *FDH* is reported to suppress secondary flow and delay corner stall [94], while *BDH* gives opposite effects [95]. In Ref. [96], *FDH* with a large angle (45°) is found to eliminate stall in an axial fan with $\kappa = 0.5$, while η_{tt} is decreased at high flow rates.

The forward and backward swept blades referred to above are mainly *FSW*, *FDH*, *FCS* and *BSW*, *BDH*. Investigations of *BCS* and axial skew are rarely reported. Since circumferential skew involves a sweep component, *FSW* and *FCS* are usually discussed together, while *BSW* and *BCS* are less interesting. As for axial skew, it is only reported in Ref. [91], with *FAS* compared to *FSW*, without reference to *BAS*.

The analyses of the effects of sweep generally focus on total-to-total efficiency and total-to-total pressure rise, while effects on total-to-static efficiency and total-to-static pressure rise are only reported in few studies.

The hub-to-tip diameter ratio κ of the axial fans in the above mentioned investigations are all medium to high, with some examples listed in Table 7.2. Studies of axial fans with small *HTR* ($\kappa \leq 0.2$) are rarely found. As shown in Refs. [89, 91], radial outward flow occurs nearly over the whole blade surface from hub to tip. This is not likely to occur for fans with small *HTR* where the chord of the blade sections is relatively smaller. Another important characteristic of such fans is that backflow occurs downstream of the fan blades [8, 27]. To the best of the authors' knowledge, the effects of sweep, dihedral and skew on the backflow region have not been reported in the literature.

Table 7.2: Hub-to-Tip Diameter Ratio κ of Example Axial Fans

κ	Reference
0.4	Beiler & Carolus [33]
0.45	Hurault *et al.* [34]
0.5	Mohammed & Raj [83]
0.5	Ramakrishna and Govardhan [91]
0.5	Vad *et al.* [36]
0.68	Corsini & Rispoli [35]

The focus of this study is on a baseline Howden axial fan as described in Sec. 4.1 with small *HTR* ($\kappa = 0.14$). As shown in Fig. 7.1, extensive backflow together with hub corner stall are present downstream and upstream of the blades for such this fan [50].

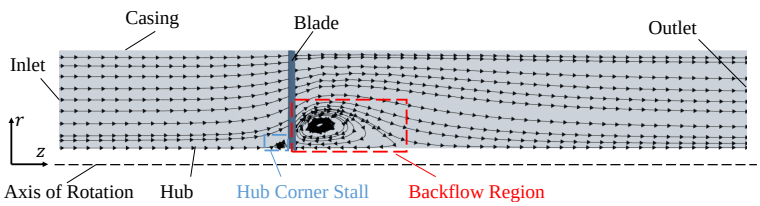

Figure 7.1: CFD Results for the Streamlines in the Meridional Plane: Backflow region and hub corner stall of Howden fan at BEP [50]

The main aim of this study is to investigate the effects of sweep, dihedral and skew on the aerodynamic performance of low-pressure axial fans with *small hub-to-tip ratio* κ. CFD simulations are employed, since it is (relatively) easy to

change the blade geometry and determine the resulting overall aerodynamic performance as well as investigate corresponding flow fields. As discussed above, the advantages and disadvantages of sweep and dihedral can also be utilized via circumferential skew and axial skew. Therefore, the investigations of sweep and dihedral are reported as focal points, with some investigations of skew to strengthen the results. Since the operation range of the investigated low-pressure axial fan with small *HTR* is outside of the stall range, this study focuses on flow rates near the best efficiency point *BEP* and on large flow rates.

Specific objectives of this CFD study are to study the effects of sweep, dihedral and skew on:

- Total-to-total and total-to-static pressure and efficiency;
- Hub corner stall and backflow region near *BEP*;
- Flow fields near the blade surface and in the blade-to-blade view, close to *BEP*;
- Reduction of the pressure coefficient due to sweep and dihedral.

It should be noted that the objective of the current study is not to perform an optimization, but to study the effects of sweep, dihedral and skew on the aerodynamic performance of low-pressure axial fans with small *HTR*. Therefore, neither structural mechanics nor aeroacoustic effects are considered, although sweep is often employed to reduce noise.

The outline of this study is as follows. The geometry of the baseline fan with small *HTR* as well as that of the fans with sweep, dihedral and skew are described in Sec. 7.2. The predicted aerodynamic performances and flow field analyses are presented in Sec. 7.3. An overview of the effects of sweep, dihedral and axial and circumferential skew are given in Sec. 7.4. Finally, conclusions and recommendations are formulated in Sec. 7.5.

7.2 Blade Geometry with Sweep, Dihedral and Skew

By changing the stacking line (and keeping the shape of the blade sections the same), sweep, dihedral and skew can be applied to the baseline fan blade. In a cylindrical coordinate system, r, θ, z indicate the radial, circumferential and axial locations, corresponding to spanwise, rotation and absolute inflow directions. With sweep, the stacking line is shifted parallel to the chord line. The stagger line (red line in Fig. 4.2(c)) is used here (instead of the chord line) as reference for sweep. Dihedral means that the stacking line is shifted in the direction that is perpendicular to the direction of sweep. Axial and circumferential skew mean that the stacking line is shifted in axial and circumferential direction, respectively.

The stacking line of the baseline fan is radially straight. Here blades with sweep, dihedral and skew are considered where the stacking line is *straight* (but

not radial as for the baseline fan). The stacking lines are then characterised by a single angle (γ_1 for sweep, γ_2 for dihedral, γ_3 for axial skew and γ_4 for circumferential skew). Examples of stacking lines and corresponding angles of sweep, dihedral, axial and circumferential skew are shown in Fig. 7.2 (a), (b) and (c).

The change of the stacking line results in a shift of the location of the stacking points of the blade sections on the Blade-to-blade (*B2B* in short) surface. The blade section shifts of sweep, dihedral and skew in the *B2B* view are shown in Fig. 7.3 with O, O_1, O_2, O_3 and O_4 representing the stacking point of the blade sections for baseline case and cases with sweep, dihedral, axial and circumferential skew respectively.

Cases of sweep, dihedral, axial and circumferential skew, forward as well as backward, have been investigated; the angles γ_1, γ_2, γ_3, γ_4 range from $-25°$ to $25°$ (with $5°$ increment). Examples of the baseline fan blade (for which $\gamma_1 = \gamma_2 = \gamma_3 = \gamma_4 = 0°$), and blades with *FSW*, *BDH*, *FCS* and *BAS* are shown in Fig. 7.4.

7.3 Predicted Aerodynamic Performance

The CFD results for the baseline fan are compared to the fans with skewed blades in order to investigate the effects of sweep, dihedral and skew on the aerodynamic performance, in Secs. 7.3.1, 7.3.2, 7.3.3 and 7.3.4 respectively. The aerodynamic performance curves are shown first, followed by the analyses of the flow fields in order to better understand the origins of the observed effects.

In order to avoid too much overlap of performance curves, results are shown for sweep angles of $5°$, $15°$ and $25°$. The discussed overall aerodynamic parameters are pressure coefficient ψ, total pressure coefficient ψ_{tt}, total-to-static efficiency η_{ts} and total-to-total efficiency η_{tt}. Six flow coefficients are considered: low flow coefficient (φ near 0.11), near *BEP* (φ near 0.13 and 0.15) and larger flow coefficients (φ near 0.19, 0.21 and 0.23). The performance curves are created by cubic spline interpolation through the six CFD predicted points. Since the resulting characteristics of ψ and ψ_{tt} are nearly the same, only the results for ψ are shown.

7.3.1 Sweep

The results for sweep are reported first. As described in Ref. [85], outward radial fluid migration for non-free vortex designs can be moderated via *FSW* to reduce losses. Thus, the combination of *FSW* and a non-free vortex distribution has been recommended to obtain improved performance. The vortex distribution of the baseline fan strongly differs from a free-vortex design (as shown in Fig. 6.4). Therefore, improved aerodynamic performance is expected from *FSW*,

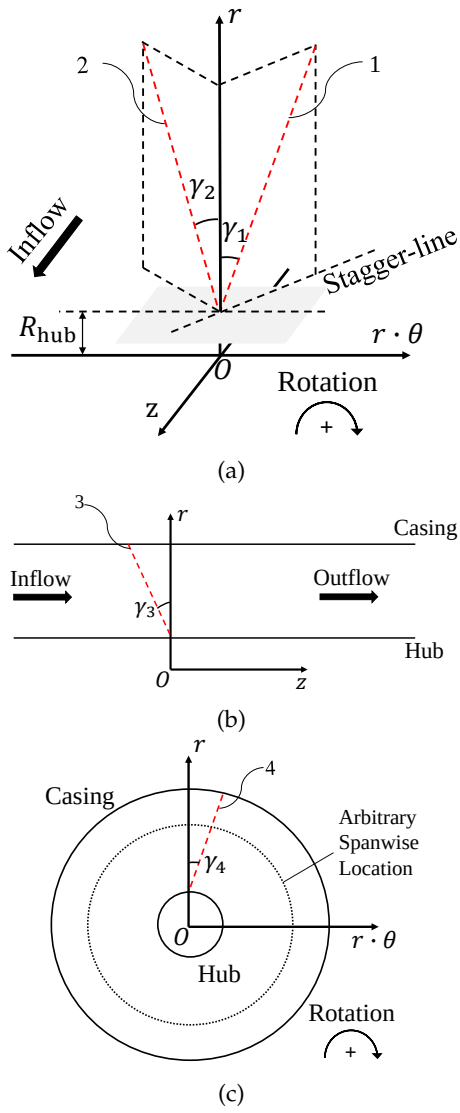

Figure 7.2: Geometrical Description of (a) Stacking Line for Sweep and Dihedral (in red and denoted by "1" and "2", respectively) and Angles γ_1 and γ_2 (b) Stacking Line for Axial Skew (in red and denoted by "3") and Angle γ_3 (c) Stacking Line for Circumferential Skew (in red and denoted by "4") and Angle γ_4

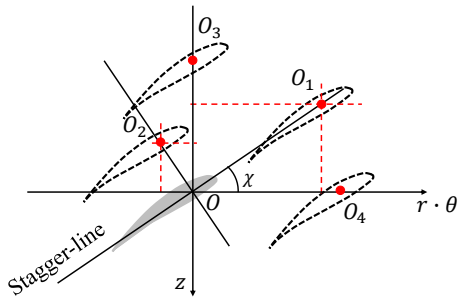

Figure 7.3: Geometrical Description of Blade Section Shift: O, O_1, O_2, O_3 and O_4 represent stacking points of original blade, and blades with (forward) sweep and dihedral, axial and circumferential skew, respectively. Inflow is in the positive z-direction

relative to the baseline fan. With respect to the pressure coefficient, it could be expected that a reduction by a factor $\cos\gamma$ is observed.

The predicted aerodynamic performance of fan blades with forward sweep (*FSW*) for different sweep angles is shown in Fig. 7.5.

Contrary to expectation, the pressure coefficient ψ is hardly affected by *FSW* for the *BEP* flow coefficient (φ near 0.15) and larger (see Fig. 7.5(a)). For small flow coefficient φ, only for a sweep angle of 25° a decrease is observed (by a factor of 0.96; much less than expected from the $\cos\gamma$ effect).

The total-to-static efficiency η_{ts} decreases with increasing *FSW* sweep angle for the low flow coefficient φ near 0.11 (maximum drop by 1.87% for 25°*FSW*), see Fig. 7.5(b). Modest improvements are noted near *BEP* and for large φ. Near *BEP*, the largest improvement is 0.33% for 15°*FSW*. At large φ near 0.23, the maximum increase is 1.21% for 25°*FSW*.

With increasing *FSW*, the total-to-total efficiency η_{tt} decreases at low flow coefficient φ and increases at high flow coefficient φ, see Fig. 7.5(c). The maximum drop (1.82%) and improvement (1.19%) are both obtained for 25°*FSW* at low and high φ, respectively. Near *BEP*, the predicted performance is effectively not affected by *FSW*. Overall, fan blades with *FSW* give improved η_{tt} at large flow coefficients, while limited benefits are obtained near *BEP*.

Contrary to *FSW*, *BSW* does not give benefits, as shown in Fig. 7.6. A larger *BSW* angle results in a larger decrease of the pressure coefficient ψ, the total-to-static efficiency η_{ts} as well as the total-to-total efficiency η_{tt}. The drop in ψ and η_{ts} does not vary much with flow coefficient φ. However, for η_{tt}, larger decreases are found for large φ. Near *BEP*, the maximum drop (for 25°*BSW*) in ψ is 3.4%, and the drops in η_{ts} and η_{tt} are 1.7% and 1.6%, respectively.

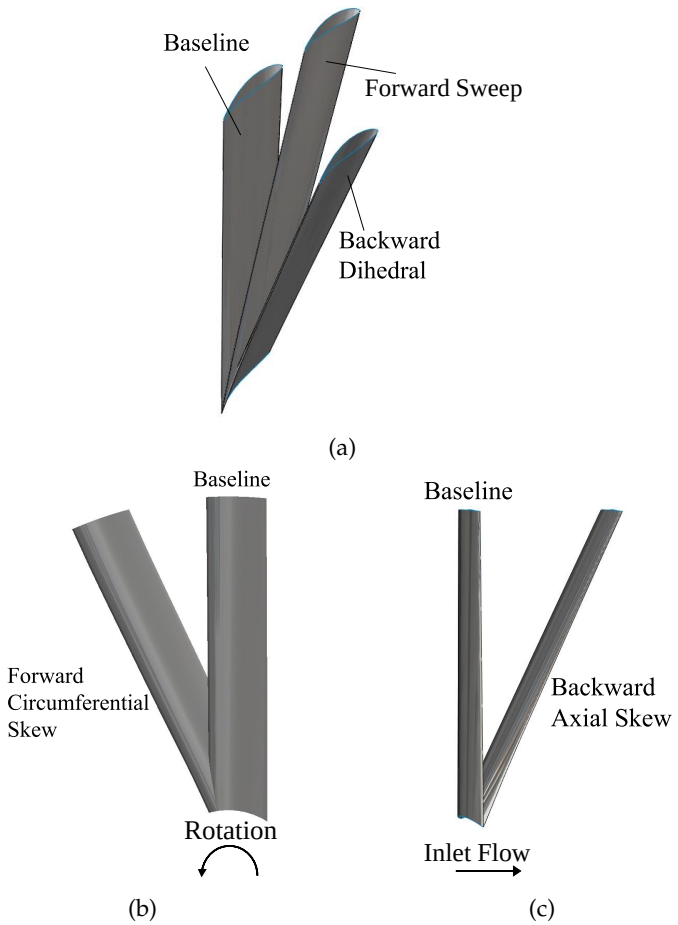

Figure 7.4: Example Blades of Baseline Case and (a) *FSW* and *BDH*, (b) *FCS* and (c) *BAS*

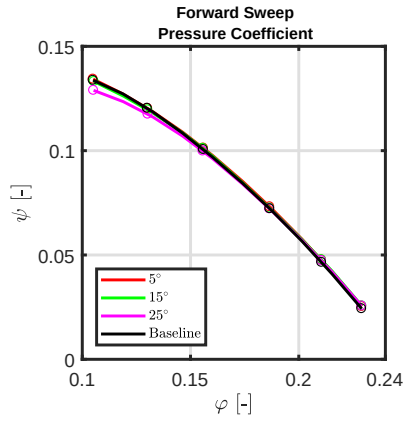

(a) $\varphi - \psi$

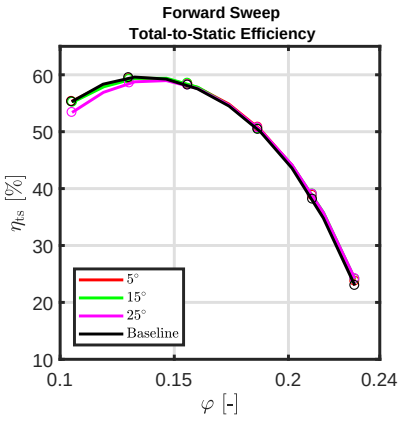

(b) $\varphi - \eta_{ts}$

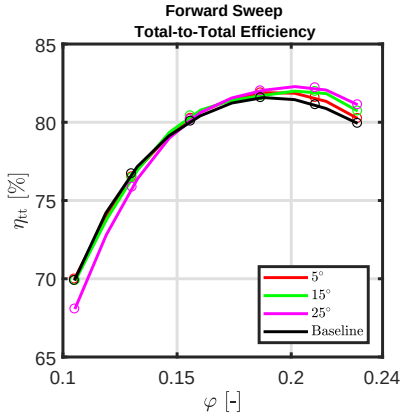

(c) $\varphi - \eta_{tt}$

Figure 7.5: CFD Predictions: Comparison between Baseline Fan and Fans with *FSW*: (a) Static Pressure Coefficient ψ, (b) Total-to-static Efficiency η_{ts} and (c) Total-to-total Efficiency η_{tt}.

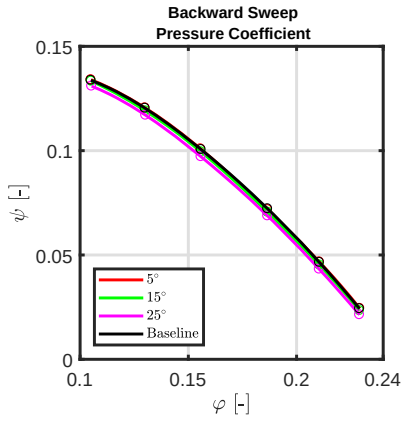

(a) $\varphi - \psi$

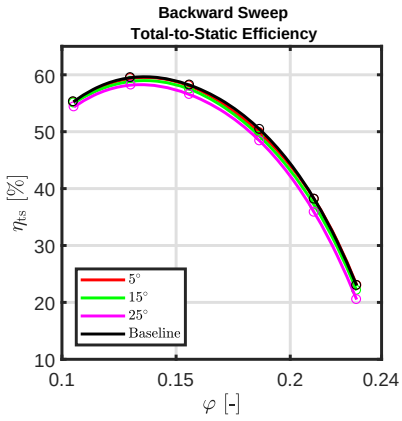

(b) $\varphi - \eta_{ts}$

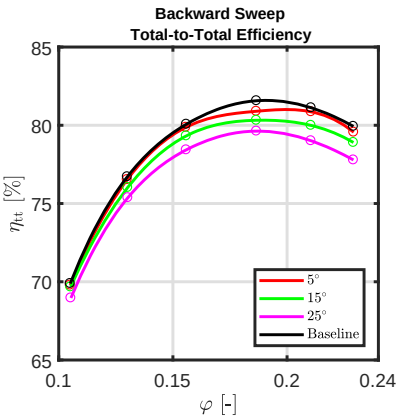

(c) $\varphi - \eta_{tt}$

Figure 7.6: CFD Predictions: Comparison between Baseline Fan and Fans with *BSW*: (a) Pressure Coefficient ψ, (b) Total-to-static Efficiency η_{ts} and (c) Total-to-total Efficiency η_{tt}

For the baseline fan at large flow coefficient $\varphi = 0.23$, secondary flow and backflow are almost eliminated [50]. In order to investigate the influence of sweep on the downstream backflow region and radial migration near the blade surface, the flow field analyses focus on streamlines in the meridional plane and near the blade suction side surface at *BEP*. In particular, the occurrence of hub corner stall and the backflow region are investigated, see also Fig. 7.1. The cases of *FSW* and *BSW* with maximum angle of 25° are investigated to have a clearer view of the influence of sweep on the flow field.

The streamlines in the meridional plane for 25°*FSW* and 25°*BSW* are shown in Fig. 7.7. The downstream backflow region with *BSW* blades is larger than that with *FSW* blades. However, the upstream hub corner stall region with *BSW* blades is smaller than that with *FSW* blades. More intensive connections between the hub corner stall and backflow regions are found with *FSW* blades, which may give more losses that reduce the improvement in aerodynamic performance expected with *FSW* blades.

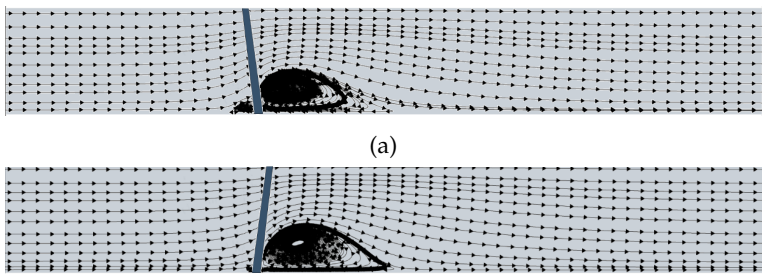

(a)

(b)

Figure 7.7: Comparison of Meridional Surface Streamlines: (a) 25°*FSW* and (b) 25°*BSW*; Both for flow coefficient at *BEP*

The streamlines of the relative flow at *BEP* near the blade suction side surface (inside the boundary layer; at averaged value of $y^+_{\text{avg}} = 8.7$) are compared in Fig. 7.8 for the baseline blade, and blades with 25°*FSW* and 25°*BSW*. Here the view is in the axial direction, from inlet towards outlet.

Radial outward flow is present for all cases, which starts from the hub towards mid-span of the blade and collects near the trailing edge. For the baseline case and *BSW*, the radial flow develops towards the tip, but for *FSW* there are even some streamlines from tip towards lower span at the trailing edge. The main streamlines occupy most area of blade surface, which is different from what is found in Refs. [89, 91] (where κ equals 0.4 and 0.5, respectively). Overall, the radial outward flow path is reduced by *FSW*, and the radial outward flow region is limited for these fans with small *HTR*.

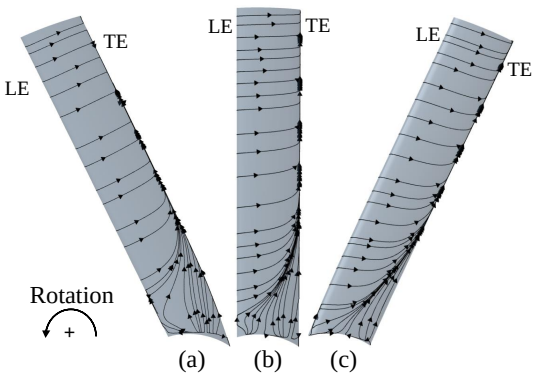

Figure 7.8: Boundary Layer Streamlines near Blade Suction Side Surface for (a) 25°*FSW*, (b) Baseline and (c) 25°*BSW*; All for flow coefficient at *BEP*, "LE" and "TE" stand for leading and trailing edge.

In both Fig. 7.7(a) and (b), the corner vortex is present near the hub. The relative velocity streamlines in the *B2B* view at 2.5% spanwise location are shown in Fig. 7.9. For both baseline case and *BSW*, only a vortex near the trailing edge is found, but with *FSW* a vortex near the leading edge is also found, corresponding to the more intensive hub corner stall also shown in Fig. 7.7.

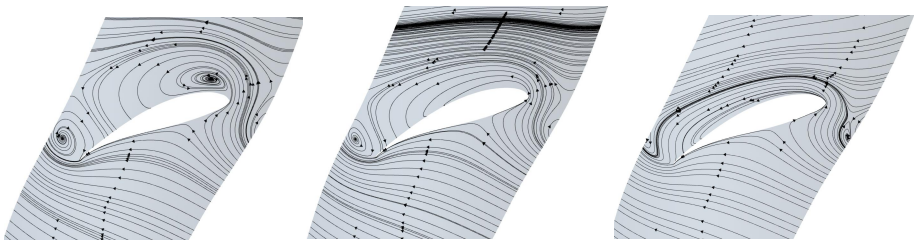

Figure 7.9: Velocity Streamlines Based on the Relative Velocity in the Blade-to-blade Plane at 2.5% Spanwise Location for: (a) 25°*FSW* (b) Baseline Case and (c) 25°*BSW*; All for flow coefficient near *BEP*

Therefore, sweep applied to axial fans with small hub-to-tip ratio will give minor improvements in pressure coefficient ψ and total-to-static efficiency η_{ts} over the full range of flow coefficient φ, but *FSW* is helpful to obtain higher total-to-total efficiency η_{tt} at large φ. With respect to the velocity distribution, although

sweep clearly affects the radial migration, the affected area is quite small, which therefore hardly contributes to the overall aerodynamic performance. The flow field analyses have shown that *FSW* is able to reduce the downstream backflow region (*BSW* has the opposite effect), yet more intensive upstream hub corner stall is also found for *FSW*.

7.3.2 Dihedral

With dihedral, the stacking line is shifted in the direction perpendicular to the chord line. *FDH* has been reported to give increased total-to-total efficiency (by 1.33%) [86] and to affect the velocity distribution downstream of the fan blades [94]. Also, *BEP* is shifted towards a lower flow coefficient φ by *FDH*. An extreme case (with large dihedral angle of 45°) is considered in Ref. [96], where *FDH* eliminates the stall in the operation range. As for the reduction in lift coefficient, different from sweep, a factor $\cos^2\gamma$ has been reported in Ref. [143] for wings.

The predicted aerodynamic performance of fan blades with *FDH* for different dihedral angles is shown in Fig. 7.10.

For the pressure coefficient ψ, a decrease in ψ is found with *FDH*. This reduction increases with *FDH* angle. The maximum decrease is 22% with 25°*FDH* for flow coefficient $\varphi = 0.23$.

For the total-to-static efficiency η_{ts}, blades with $5° - 25°$ *FDH* give improvements at low flow coefficients φ, the maximum increase is 0.95% found for 15°*FDH* near $\varphi = 0.11$; at flow coefficients φ larger than *BEP*, 5°*FDH* gives nearly same efficiency as the baseline case, while others result in drops; the maximum drop is found at $\varphi = 0.23$ for 25°*FDH*.

With respect to the total-to-total efficiency η_{tt}, blades with $5° - 15°$ *FDH* perform better for all flow coefficients φ; 25°*FDH* performs better only at low φ. The largest improvement is 0.82% with 15°*FDH* near $\varphi = 0.11$; this is the same as what has been found for η_{ts}.

Therefore, considering the improved, higher η_{ts} and η_{tt}, 15°*FDH* performed better among all *FDH*. Larger dihedral angles are not recommended due to large drops in both ψ and η_{ts}.

The predicted aerodynamic performance of fan blades with *BDH* for different angles shows significant decreases in aerodynamic performance (data not shown), with larger dihedral angles giving larger decreases. 5°*BDH* gives nearly the same performance as the baseline case; all other *BDH* result in decreased performance over all φ. The maximum drops in pressure coefficient ψ, total-to-static efficiency η_{ts} and total-to-total efficiency η_{tt} are for 25°*BDH*.

According to Ref. [94], *FDH* is able to suppress secondary flow. In order to investigate the effects of dihedral on the hub corner stall and backflow, the streamlines in the meridional plane are shown in Fig. 7.11 for 25°*FDH* and 25°*BDH* at

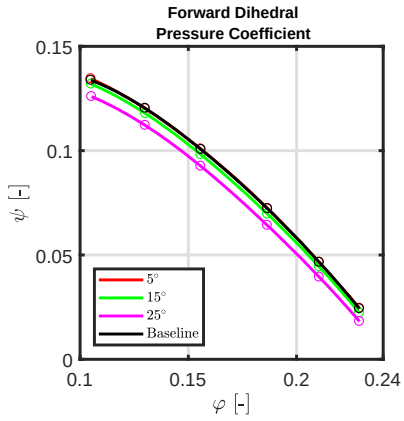

(a) $\varphi - \psi$

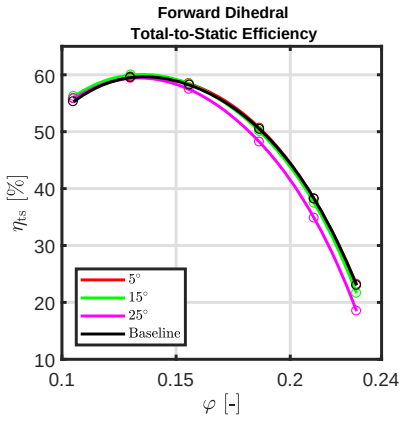

(b) $\varphi - \eta_{ts}$

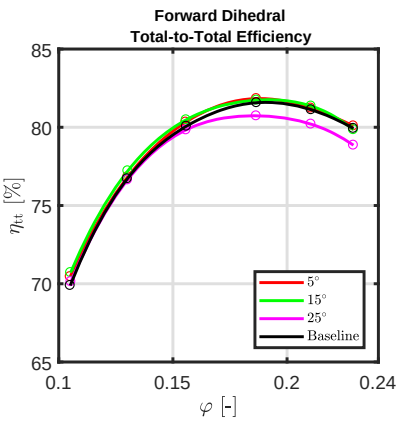

(c) $\varphi - \eta_{tt}$

Figure 7.10: CFD Predictions: Comparison between Baseline Fan and Fans with *FDH*: (a) Pressure Coefficient ψ (b) Total-to-static Efficiency η_{ts} and (c) Total-to-total Efficiency η_{tt}

flow coefficient φ near *BEP*. *FDH* (slightly) intensifies the hub corner stall upstream of the blade and reduces the backflow region downstream the blade; the opposite effects are found with *BDH*.

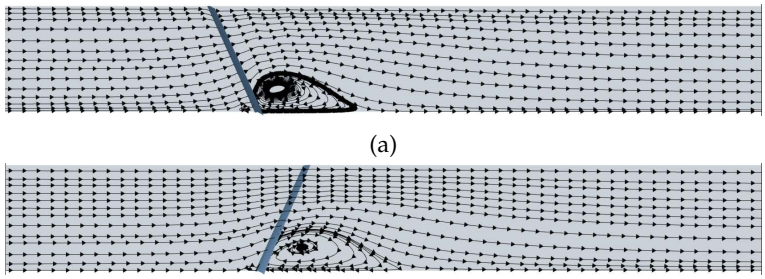

(a)

(b)

Figure 7.11: Comparison of Meridional Surface Streamlines: (a) 25°*FDH* and (b) 25°*BDH*; Both for flow coefficient at *BEP*

The relative velocity streamlines near the blade suction side surface are shown in Fig. 7.12 for 25°*FDH* and 25°*BDH* and are compared with the baseline case for flow coefficient φ near *BEP*.

The streamlines are different from those for sweep cases in Fig. 7.7, no significant difference in radial outward flow pattern is found between *FDH* and *BDH* blades, but the extent of radial flow is reduced in comparison to the baseline case.

A visualisation of the relative velocity streamlines on the *B2B* view at 2.5% spanwise location, for both baseline case and *BDH*, showed that only a vortex near the trailing edge is found at the hub (data not shown). For *FDH* a small vortex near mid chord is also found, which corresponds to a slightly more intensive hub corner stall region.

Although higher total-to-total efficiency η_{tt} can be obtained from 15°*FDH*, the overall aerodynamic performance of fan blades with dihedral is not satisfactory, since no significant improvement in total-to-static efficiency η_{ts} is obtained.

7.3.3 Axial Skew

For axial skew, the blade leans towards the inflow or outflow direction, as described in Sec. 7.2. Investigations on axial skew are not often reported, especially on *BAS*. According to the results in Sec. 7.3.1 and 7.3.2, axial skew is expected to affect the backflow region and hub corner stall.

The predicted aerodynamic performance of fan blades with *FAS* for different angles is shown in Fig. 7.13.

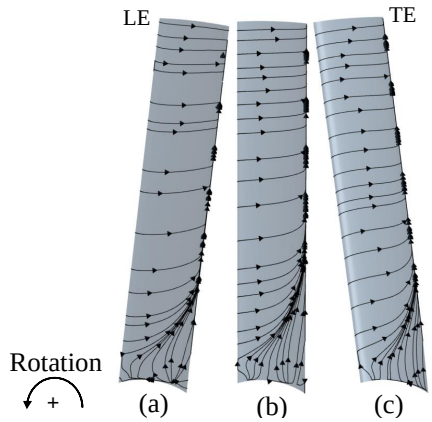

Figure 7.12: Boundary Layer Streamlines near Blade Suction Side Surface for (a) 25°*FDH*, (b) Baseline and (c) 25°*BDH*; All for flow coefficient at *BEP*, "LE" and "TE" Stand for leading and trailing edge.

For the pressure coefficient ψ, only 5°*FAS* blade gives a small increase at all flow coefficients φ; the others show a drop in ψ. A larger axial skew angle leads to a larger drop; the maximum is 24.6% for 25°*FAS* near $\varphi = 0.23$.

For the total-to-static efficiency η_{ts}, increases are not very significant. The maximum increase is 0.7% for 15°*FAS* at φ near 0.11; the maximum decrease is 4.3% for 25°*FAS* near $\varphi = 0.23$. Near *BEP*, only the blade with 25°*FAS* gives a decrease; at large φ, decreases are found for all *FAS* except with 5° axial skew angle.

For the total-to-total efficiency η_{tt}, improvements are obtained for all angles for all φ, except 25°*FAS*.

The predicted aerodynamic performance of fan blades with *BAS* for different angles show (data not presented) that the aerodynamic performance is reduced for *BAS*; larger skew angles give larger decreases. Only 5°*BAS* at large φ gives some increase in ψ and η_{ts}.

The meridional surface streamlines for fan blades with forward and backward axial skew of 5°, 15° and 25° are shown in Fig. 7.14. *BAS* leads to a backflow region with larger extent in streamwise direction; the opposite effect occurs with *FAS*. However, *FAS* tends to give a larger hub corner stall region upstream of the blades. These observations conform with the expectation.

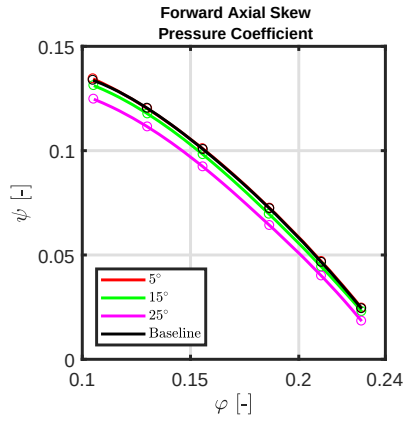

(a) $\varphi - \psi$

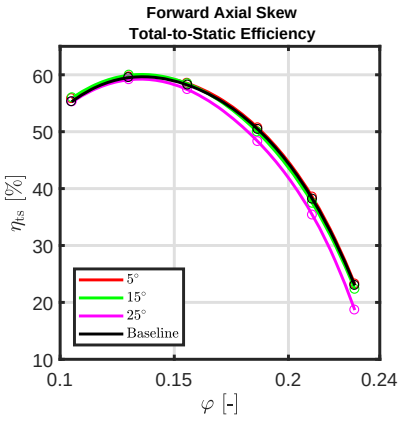

(b) φ - η_{ts}

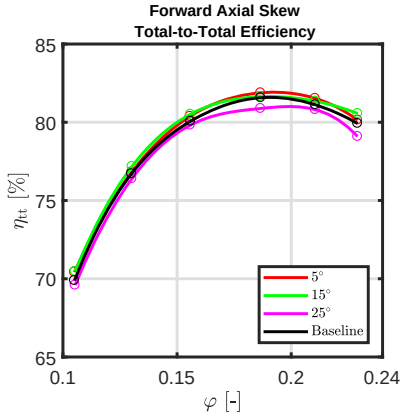

(c) φ - η_{tt}

Figure 7.13: CFD Predictions: Comparison between Baseline Fan and Fans with *FAS*: (a) Pressure Coefficient ψ (b) Total-to-static Efficiency η_{ts} and (c) Total-to-total Efficiency η_{tt}.

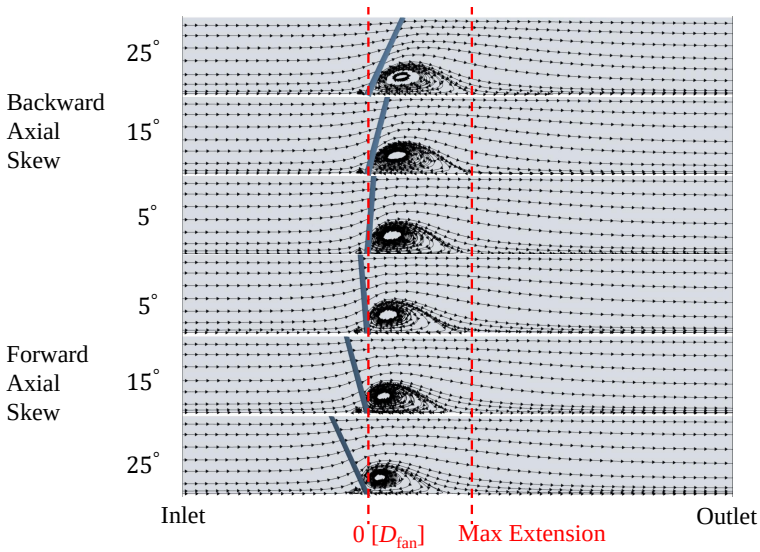

Figure 7.14: Backflow Region Downstream of Fan Blades with Different Forward and Backward Axial Skew Angles

7.3.4 Circumferential Skew

As described in Sec. 7.2, advantages and disadvantages of sweep will also be observed with circumferential skew. Therefore, the results in Sec. 7.3.1 and Sec. 7.3.2 suggest that radial migration boundary layer flow is expected to be reduced by *FCS*.

The predicted aerodynamic performance of fan blades with *FCS* with different angles is shown in Fig. 7.15. The predicted results are qualitatively similar to the results for *FSW*. No significant improvement is found in both pressure coefficient ψ and total-to-static efficiency η_{ts} over all flow coefficients φ. Some improvements are found in total-to-total efficiency η_{tt} at large φ.

The predicted aerodynamic performance of fan blades with *BCS* with different angles is quite similar to the results with *BSW* in Sec. 7.3.1. For pressure coefficient ψ, total-to-static efficiency η_{ts} and total-to-total efficiency η_{tt}, larger skew angles result in larger decreases. For different flow coefficients φ, the drops in ψ and η_{ts} are nearly the same, but for η_{tt} larger decreases are obtained at large φ. However, at low flow coefficient φ near 0.11, the predicted performance of *BCS* is nearly the same as that of the baseline case, which is different from what is reported for *BSW*.

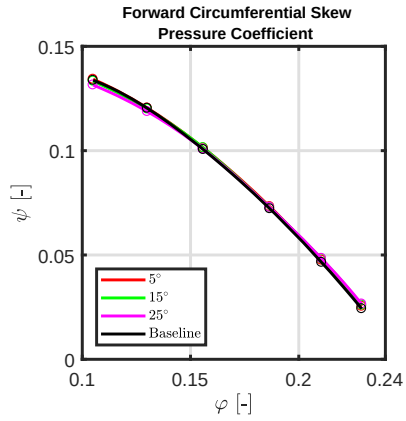

(a) $\varphi - \psi$

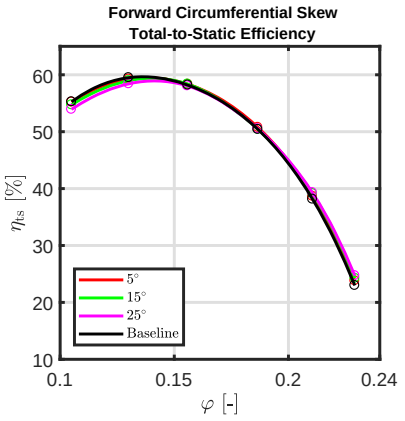

(b) φ - η_{ts}

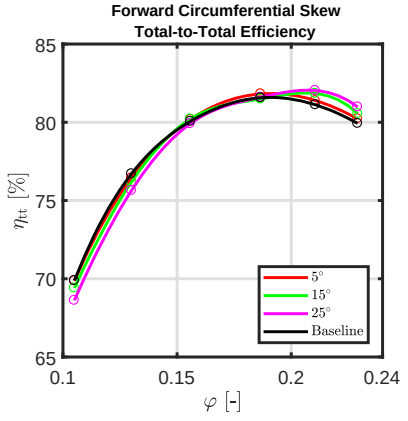

(c) φ - η_{tt}

Figure 7.15: CFD Predictions: Comparison between Baseline Fan and Fans with *FCS*: (a) Pressure Coefficient ψ (b) Total-to-static Efficiency η_{ts} and (c) Total-to-total Efficiency η_{tt}.

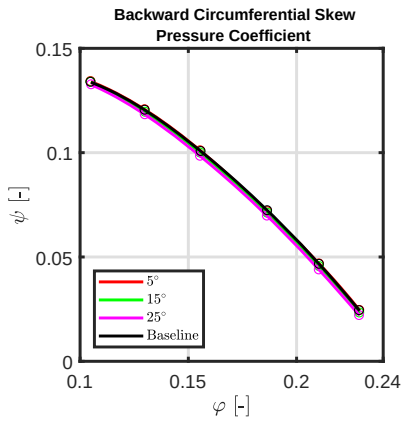

(a) $\varphi - \psi$

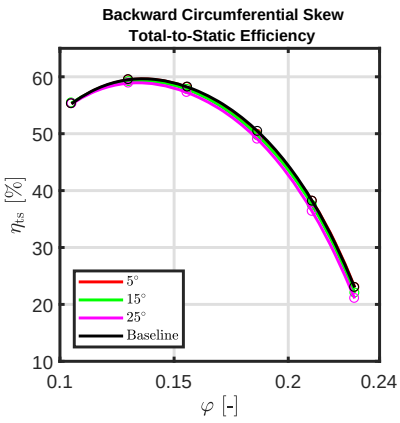

(b) φ - η_{ts}

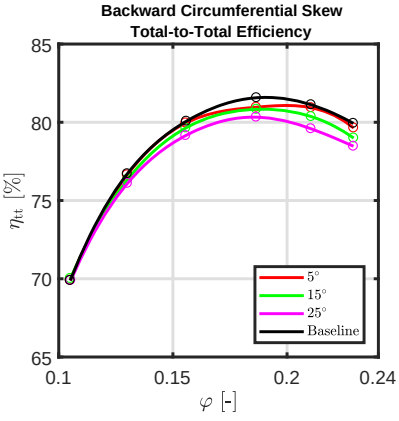

(c) φ - η_{tt}

Figure 7.16: CFD Predictions: Comparison between Baseline Fan and Fans with *BCS*: (a) Pressure Coefficient ψ (b) Total-to-static Efficiency η_{ts} and (c) Total-to-total Efficiency η_{tt}.

The visualisation of the boundary layer streamlines on surface near blade suction side (data not presented) shows that with *FCS* the outward flow path near trailing edge is shortened; for *BCS* the opposite effect is observed.

7.4 Overview of skew effects

In this section the effects on the aerodynamic performance of sweep, dihedral and axial and circumferential skew are compared. The focus is on radial migration in Sec. 7.4.1, the extent of the backflow region in Sec. 7.4.2, the pressure reduction in Sec. 7.4.3 and the maximum efficiencies in Sec. 7.4.4.

7.4.1 Radial Migration Flow

As discussed in Sec. 7.3, the boundary layer radial outward flows near the suction side are present for all blades. Differently from the flow patterns in medium to high *HTR* fans where the radial migration occupies most of the suction side surface (shown for example in Ref. [85]), the radial flow in the current study is mostly around the hub area and develops towards the tip near the trailing edge.

Blades with *FSW* and *FCS* give shortened outward flow paths near the blade suction side surface; *BDH* also shows such potential (although less noticeable). For *BSW* and *BCS* the effect is opposite. However, due to the limited affected area near the suction side surface, such benefits hardly contribute to overall aerodynamic improvements.

7.4.2 Backflow Region

Blades with *FSW* and *FDH* reduce the backflow downstream of the blades, but intensify the hub corner stall region upstream of blades and the separation near the hub blade section; *BSW* and *BDH* have the opposite effects.

In order to quantitatively compare the influence on the backflow region from sweep, dihedral and axial and circumferential skew, the size of the backflow region is quantified by a backflow area percentage $P(z)$ through streamwise (axial) cross-sections $A(z)$ downstream of the fan blade

$$P(z) = \frac{\int_{A(z)} H(v_z)\, dA}{\int_{A(z)} dA} \qquad H(v_z) = \begin{cases} 1 & v_z \leq 0 \\ 0 & v_z > 0 \end{cases}, \tag{7.1}$$

where v_z is axial velocity. The integrals present in Eq. (7.1) are numerically evaluated, based on a Delaunay triangulation of the cross-sections.

The backflow area percentages $P(z)$ are investigated for streamwise locations at $z/D_{\text{fan}} = 0.05$ to $z/D_{\text{fan}} = 0.65$, where the fan is located at $z/D_{\text{fan}} = 0$.

In order to show the most significant trends, the backflow area percentages are shown in Fig. 7.17 for 25° sweep, dihedral and axial and circumferential skew (both forward and backward).

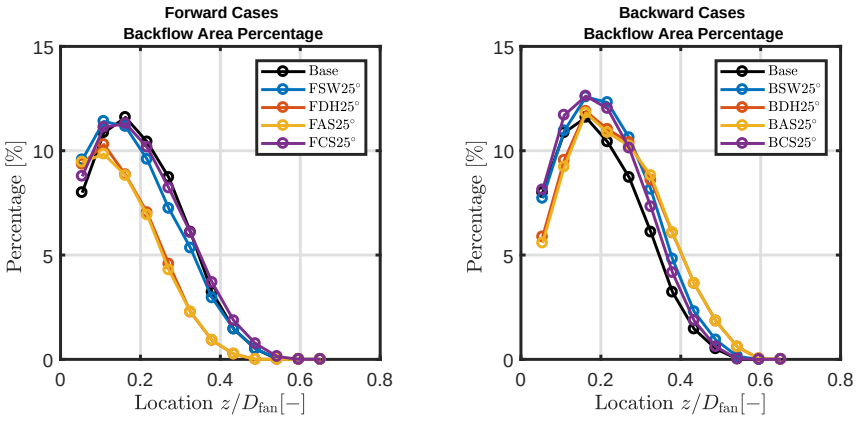

(a) (b)

Figure 7.17: Backflow Percentage $P(z)$ in Eq. (7.1) for Various Axial Sections Downstream of the Blades for $\gamma = 25°$: (a) Forward Blades (b) Backward Blades.

Compared with the baseline case, blades with forward skew decrease both the size and the axial extent of the backflow region. The opposite holds for blades with backward skew. The effects of sweep and circumferential skew are similar; the same holds for dihedral and axial skew.

In detail, *FAS* gives the smallest backflow area as well as the smallest axial extent. Blades with *BAS* give the largest axial extent. The largest backflow area is observed for *BSW* and *BCS*.

Since the stagger angle of the investigated fan is $\chi = 15°$, circumferential and axial skew participate more in sweep and dihedral, respectively. Hence, circumferential skew plays a main role in the outward radial flow pattern, while axial skew plays a main role in the backflow region and hub corner stall region.

7.4.3 Pressure Reduction

In investigations of wing aerodynamics [28, 142, 143] and axial fan aerodynamics [33, 83, 89], it is shown or assumed that lift/pressure is reduced by $\cos\gamma$ with sweep and by $\cos^2\gamma$ with dihedral. In order to investigate this effect for fans with small *HTR*, the pressure coefficient ratios between sweep, dihedral and the

baseline case (ψ/ψ_{Base}) are compared in Fig. 7.18 for different flow coefficients φ for $\gamma = 25°$.

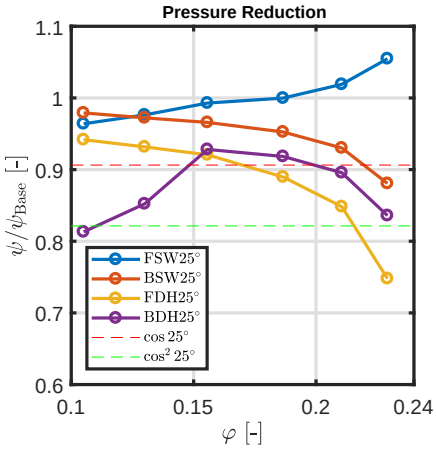

Figure 7.18: CFD Predictions: Pressure Reduction ψ/ψ_{Base} due to Sweep and Dihedral, with $\gamma = 25°$; $\varphi - \psi/\psi_{\text{Base}}$ with Forward and Backward Sweep and Dihedral

Neither the $\cos\gamma$ effect for sweep nor the $\cos^2\gamma$ effect for dihedral is observed in current study. Backward and forward sweep (the same holds for dihedral) could be expected to give the same pressure reduction, which is not observed. This is different from the results reported in Ref. [89] where the pressure reduction due to forward and backward sweep is reasonably equal (for fans with κ in the range $0.4 - 0.5$). With forward skewed (in the general sense) blades, only *FSW* gives some increase in pressure coefficient ψ.

Overall, the pressure with sweep and dihedral is larger than expected, based on the lift reduction factors of $\cos\gamma$ and $\cos^2\gamma$ for sweep and dihedral from aerodynamics.

These deviations are considered to be due to the flow in axial fans being (much more) three-dimensional (spanwise variations in angle of attack; hub corner stall and backflow region, etc.) in comparison to flows around wings.

7.4.4 Predicted Maximum Efficiency

Finally, the potential is investigated for employing sweep, dihedral and axial and circumferential skew to improve the *maximum* (when varying the flow coefficient φ) total-to-static and total-to-total efficiency; $\eta_{\text{ts,max}} = \max_\varphi \eta_{\text{ts}}$ and $\eta_{\text{tt,max}} = \max_\varphi \eta_{\text{tt}}$. These maximum efficiencies are shown in Fig. 7.19.

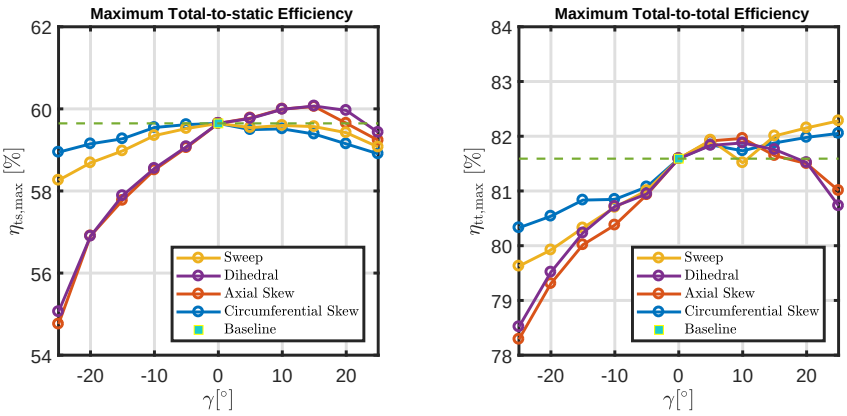

(a) Skew Angle - $\eta_{ts,max}$

(b) Skew Angle - $\eta_{tt,max}$

Figure 7.19: Predicted *Maximum* Efficiency for Blades with Sweep, Dihedral and Skew, for Different (Positive and Negative) Angles: (a) Total-to-static Efficiency $\eta_{ts,max}$ (b) Total-to-total Efficiency $\eta_{tt,max}$

The results for the maximum total-to-static efficiency $\eta_{ts,max}$ are shown in Fig. 7.19 (a). The highest $\eta_{ts,max}$ is found for 15°*FDH* (increase by 0.42%). Axial skew and dihedral give almost the same $\eta_{ts,max}$. For negative angles, axial skew and dihedral give significant decreases in maximum $\eta_{ts,max}$. Increases in $\eta_{ts,max}$ are not found with forward sweep and circumferential skew, but the decreases with backward sweep and circumferential skew are smaller.

The results for the maximum total-to-total efficiency $\eta_{tt,max}$ are shown in Fig. 7.19(b). The highest $\eta_{tt,max}$ with sweep and circumferential skew is found for the largest considered angle (increases by 0.69% and 0.46%, respectively). For dihedral and axial skew, the optima are found in forward direction for angles in the range $5° - 15°$.

7.5 Conclusions

By using a validated CFD simulation method for low-pressure axial fans with small hub-to-tip diameter ratio [50] as reported in Chapter 6, simulations have been performed to investigate effects of (forward as well as backward) sweep, dihedral and skew on the aerodynamic performance of such fans, with a linear stacking line.

In contrast to the flow patterns in medium to high *HTR* fans where radial migration occupies most of the suction side surface, the radial flow in the current study is more limited due to the chord of the blade sections being relatively smaller. The beneficial aerodynamic effects of skew (in the general sense) of the blades are therefore more limited here. In general, backward skew gives negative effects, while forward skew can (conditionally) give positive effects.

Blades with sweep hardly lead to improvements in pressure coefficient and total-to-static efficiency. Only at large flow coefficient does forward sweep result in higher total-to-total efficiency. Forward dihedral gives some improvement in total-to-static and total-to-total efficiency near *BEP* and for large flow coefficient, but 25°*FDH* and all blades with *BDH* result in negative effects. Circumferential skew gives a performance similar to that with sweep, in both forward and backward direction, with higher total-to-total efficiency.

It should be noted that the reason for the similar performance in sweep and circumferential skew, as well as with dihedral and axial skew, is the small stagger angle $\chi = 15°$. The benefits and disadvantages of sweep and dihedral can be traced to circumferential and axial skew. With different stagger angles, the proportion of circumferential and axial skew in sweep and dihedral is changed, and the consequent performance may also be changed.

Differently from wing aerodynamics where lift coefficients are reduced by factors $\cos\gamma$ and $\cos^2\gamma$ for sweep and dihedral respectively, the reduction of the pressure coefficients is much more limited (pressure rise is larger than expected). This is considered to be the result of the (much more) complex three-dimensional flow patterns in axial fans, involving backflow and hub corner stall that are absent in flows around wings.

The highest η_{ts} is predicted for axial skew; only 5°*FAS* gives positive effects on both pressure coefficient and efficiency. *FAS* as well as *FDH* influence the backflow region significantly, where a larger forward angle helps to suppress the backflow.

Although the improvements from sweep, dihedral and skew on fan aerodynamic performance are limited for the considered baseline fan with small *HTR*, for different optimization purposes, different blade shifts can be applied. *FSW* and *FCS* with large angles can be used for higher η_{tt}, while *FDH* and *FAS* can suppress backflow and give positive effects on η_{ts}.

For future studies, it is recommended to: (i) investigate the effects of sweep, dihedral and skew with non-straight stacking line (with angles γ_1, γ_2, γ_3 and γ_4 in Fig. 7.2 that vary with spanwise locations), aimed at partial combination of beneficial shape variations into a single blade, (ii) study the effects of the vortex distribution together with sweep, dihedral and skew to obtain better flow control and reduced loss and (iii) perform CFD simulations for other small *HTR* axial fans with sweep, dihedral and skew and (iv) perform measurements of small

HTR axial fans to investigate the effects of sweep, dihedral and skew on overall aerodynamic performance as well as local flow phenomena like tip leakage flow.

Chapter 8

Optimal Vortex Distribution Design Method

The results reported in this chapter are adapted from a submitted journal paper. The research background is introduced in Sec. 8.1. The vortex distribution design method is concisely described in Sec. 8.2. The selection of free-vortex and polynomial vortex designs, following the ideas of Bamberger and Carolus [13, 145], are presented in Sec. 8.3. In this Section an analytical formulation is also given for the optimal HTR for free-vortex designs (for the first time in the literature about axial fans, to the author's best knowledge). The parameters of the baseline fan and design results are described in Sec. 8.4. For the fan designs resulting from various vortex distributions, the aerodynamic performance and the flow fields resulting from CFD simulations are presented in Sec. 8.5. Finally, conclusions and recommendations are formulated in Sec. 8.6.

8.1 Research Background

As introduced in Chapter 2, the vortex distribution (denoted by $r\,v_{\theta 2}(r)$, with r and $v_{\theta 2}$ being the radial coordinate and the downstream circumferential component of the absolute velocity, respectively) design method for axial fans is well established, a detailed description can also be found in Refs. [21, 121].

In this approach the vortex distribution $r\,v_{\theta 2}(r)$ acts as input and the geometry of the fan blades is a result. The simplest vortex distribution is the so-called free-vortex design where $r\,v_{\theta 2}(r)$ is constant value alone the blade span. The performance of resulting designs can be assessed by experiments or CFD simulations.

Ruden [146] first described the possibility of employing different vortex distributions (deviating from the free-vortex distribution) for axial-fan designs, where the radial equilibrium condition (described later in Sec. 8.2; see Eq. (8.2)) has been used.

Wallis [21] discusses both free-vortex and general vortex distributions in his book, with extensive theoretical background. Isolated airfoil theory and cascade analyses are also discussed in relation to their suitability with respect to the blade solidity. Following Wallis's ideas, Downie et al. [121] provide practical design guidelines for low to medium pressure rise rotor-only axial fans. They introduce the vortex distribution design method for general vortex distributions step by step, with well-explained assumptions and selections of variables. Three rotors with different blade numbers and blade section profiles have been designed and their performance has been measured. In comparison to the measured performance, the vortex distribution design method provides adequate predictions of the velocity distribution (mainly the axial component) and of the overall performance at the design point (flow coefficient $\varphi = 0.23$). The HTR of the fan design $\kappa = 0.38$ and according to the measured axial velocity distribution, no backflow is present.

Castegnaro and Masi [11] surveyed the aerodynamic performance of 30 rotor-only axial fans with different vortex distributions at design or BEP duty point. It was found that free-vortex designs conform most to the Cordier curve and perform better with small total pressure coefficients (ψ_{tt} around 0.1) and small HTRs (κ around 0.2 to 0.3) in comparison with designs of other vortex distributions. The aerodynamic performance of four small-scale fans (designed by free and general vortex distributions) have been evaluated experimentally in order to investigate the influence of the vortex distribution on the aerodynamic performance at the design point of rotor-only axial fans. The investigated flow coefficient φ ranges from 0.1 to 0.4, the total-to-total pressure coefficient ψ_{tt} varies from 0.1 to 0.3 with HTR κ being 0.31, 0.44 (two fans) and 0.64. It was found that the general vortex distribution design is able to extend the stall margin and is more sensitive to the influence of the tip clearance effect. In addition, the measured axial velocity distributions at the design flow rate showed no backflow.

For a free-vortex design, the constant involved is directly related to the ideal total pressure rise, as follows from the Euler relation. For more general vortex distributions the additional degrees of freedom can be employed to optimise selected design aspects (with some optimisation algorithm).

Sörensen et al. [147, 148] optimised the total-to-total efficiency of a rotor-only fan by varying the HTR κ and the vortex distribution. In their optimisation problem, constraints were formed by the required total-pressure rise at a number of flow rates, a range for the blade solidity, an upper limit for the absolute flow angle at outlet and for the angle of attack. It was found numerically that an optimum HTR exists ($\kappa_{opt} = 0.69$ and 0.63 with their diffuser efficiency being 95% and 90%, respectively). Their design method was validated by comparison with measurements for one designed fan with $\kappa = 0.69$. The estimated design duty corresponds

to flow coefficient $\varphi = 0.3$ and total pressure coefficient $\psi_{tt} = 0.41$. Good agreement in efficiency η_{ts} and η_{tt} was observed for large flow rates. For the velocity distributions (in both axial and circumferential components), results of the design method were similar to those from measurements, except near the hub and the tip region. Backflow was not expected with their large HTR, and is not referred to.

A preliminary design guideline based on the achievable total-to-total efficiency η_{tt} was reported by Masi et al. [124] where the fan performance, including considerations of inlet and outlet guide vanes, were analysed theoretically with a linear vortex distribution (corresponding to a constant local swirl coefficient $v_{\theta 2}/v_x$). An efficiency chart as function of flow coefficient φ, swirl coefficient and HTR was presented. The results showed that κ plays an important role in affecting diffusion losses and swirl velocity losses. With lower κ, η_{tt} increased since the sensitivity of η_{tt} to other parameters was reduced at the same time. The optimal swirl coefficient was also analysed as function of φ and κ. Experimental data was shown as validation. Following this design approach, the authors optimized a small-scale baseline fan [123], where κ was decreased from 0.4 to 0.28 and $\eta_{tt.max}$ increased by 4%. It should be noted that the investigated fan operated at small $\varphi = 0.04 - 0.15$ with total pressure coefficient $\psi_{tt} = 0.01 - 0.03$. Under these conditions backflow is not present.

The idea that the kinetic energy at the outlet represents a loss for rotor-only axial fans was also reported by Bamberger and Carolus [13, 145]. As a guide to the design of such machines, they investigated the achievable total-to-static efficiency η_{ts}. To this end, they determined the vortex distribution such that the kinetic energy power at outlet is minimised. In their minimisation problem, the flow rate and the required ideal total-pressure rise form constraints. They considered linear variations of the vortex distribution, so with two degrees of freedom. Additionally, the HTR κ was a degree of freedom. They determined the corresponding maximum ideal total-to-static efficiency $\eta_{ts.idmax}$ for a large number of values of specific speed σ and specific diameter δ inside the so-called Cordier Band.

Additionally, Bamberger and Carolus [13, 145] determined for a large number of (parametrically) designed fans, the aerodynamic performance via CFD simulations [107]. Interpolation within their parameter space was performed with an artificial neural network [106]. The maximum total-to-static efficiency obtained from their set of CFD simulations (where the tip clearance ratio is constant at 0.1%), $\eta_{ts,CFD}$, was 68% for a medium specific speed σ ($\sigma \simeq 1.3$) and a specific diameter δ at the upper limit of the specific fan diameters ($\delta \simeq 1.9$). The difference between their maximum total-to-static efficiency $\eta_{ts,CFD}$ from CFD simulations and the maximum ideal total-to-static efficiency $\eta_{ts.idmax}$ is about 10% for large specific speeds ($\sigma \simeq 2.0$), corresponding to the range of interest for the current

study. In this range of specific speeds, the hub-tip ratio κ from designs based on optimisation of CFD results were larger than the critical hub-tip ratio κ according to Strscheletzky [8, 149, 150]. This may be due to the range of hub-tip ratio $\kappa \geq 0.3$ considered in [13, 106, 145], and as a consequence backflow was absent. It should be noted that the maximum η_{ts} (68%) was obtained at an untypical operation point for axial fans, close to the area of mixed-flow fans.

The previous studies [13, 123, 124, 145] have shown that in order to increase the total-to-static efficiency of rotor-only fans, the HTR κ may be reduced, since this gives smaller wasted axial kinetic energy. However, for fans with small κ backflow is more likely to occur according to the well-known Strscheletzky criterion [8, 149, 150]. Some aspects of this criterion are discussed in Appendix A. Note that in all studies referred to above, the HTR is in the range $\kappa > 0.28$ where backflow is not present.

For low-pressure axial fans with high total-to-static efficiency, the HTR tends to be smaller than for fans types studied more widely in the literature. For the application of the (well established) vortex distribution design method to such fans with small HTR, the following aspects should be carefully considered:

- The occurrence of backflow.
- The large variations in spanwise direction of angles and magnitudes of the relative velocity vectors at inlet and outlet of blade sections, due to the large spanwise variation of the blade speed u; $u_{tip}/u_{hub} = 1/\kappa$.
- The resulting large spanwise variation of the required lift coefficient of the blade sections, with a large required lift coefficient at the hub.

The objective of the current study is to improve the total-to-static efficiency η_{ts} as well as the total-to-total efficiency η_{tt} of low-pressure axial fan with small κ by finding optimized vortex distributions. Specific objectives are to:

- Find optimal fan blade designs by (i) determining the vortex distribution $r v_{\theta 2}(r)$ through an optimization process for the maximum ideal total-to-static efficiency $\eta_{ts.idmax}$ where the target flow coefficient and the total pressure coefficient form constraints and (ii) properly selecting the spanwise distribution of the required lift coefficient of the blade sections.
- Investigate the effects of both free-vortex and polynomial vortex distributions on the aerodynamic performance by means of extensive CFD simulations, employing the strategy developed in [50] and reported in Chapter 5 for fans with small κ.

8.2 Vortex Distribution Design Method

The vortex distribution design method is a method for determining the fan blade geometry from basic information involving the desired duty point. Of the blade geometry, the number of blades Z, the hub and tip diameters, D_{hub} and D_{fan} respectively, are given. Of the operational parameters, the rotational speed Ω and the volumetric flow rate Q are specified. The lift coefficient distribution in spanwise direction $C_l(r)$ of the fan blade sections is specified. The increases in pressure, p_{f} and p_{fs}, total-to-static efficiency η_{ts} and the blade stagger angle $\chi(r)$ and the chord length distribution $l(r)$ are results of the method.

The primary design input parameter in this method is the vortex distribution $r\,v_{\theta 2}(r)$, where r is the radial coordinate and $v_{\theta 2}$ is the circumferential component of the absolute velocity downstream of the fan blades, that is specified along the spanwise direction.

The vortex distribution $r\,v_{\theta 2}(r)$ is important to the energy transfer from the rotating blades to the fluid, as follows from the Euler relation (Eq. (2.11)) [9]

$$\frac{p_{02} - p_{01}}{\rho \eta_h} = W = u_2 v_{\theta 2} - u_1 v_{\theta 1} = \Omega\,(r_2 v_{\theta 2} - r_1 v_{\theta 1}) \tag{8.1}$$

where W is the specific work and η_h is the (estimated) hydraulic (total-to-total) efficiency; subscripts 1 and 2 indicate quantities upstream and downstream of the fan blades. For axial fans without appreciable radial flow, the (local) blade speed is constant from inlet to outlet, i.e. $u_1 = u_2 \equiv u(r) = \Omega r$. The Euler relation shows that the energy transfer is determined by the change, from inlet to outlet, of the fluid's angular momentum (per unit mass) $r\,v_\theta$. Generally, for fans without inlet guide vanes, the inlet flow is directed in the axial direction without pre-rotation, so $v_{\theta 1} = 0$. This assumption is adopted in the following.

Variations of the vortex distribution with radius r give different loadings of the blade sections. For a so-called *free-vortex* distribution $r\,v_{\theta 2}(r) = \text{const}$, and hence all blade sections have equal loading.

The pressure $p_2(r)$ downstream of the blades (assumed to be uniform in circumferential direction) can be determined from the radial equilibrium equation (Eq. (2.19)) [9]

$$\frac{1}{\rho}\frac{dp_2}{dr} = \frac{1}{r} v_{\theta 2}^2 \tag{8.2}$$

By combining the Euler equation (8.1) and the radial equilibrium equation (8.2) with the additional assumptions that the inlet stagnation pressure p_{01} is uniform and that the hydraulic efficiency η_h is independent of r, it follows after some

algebra that (see also [11])

$$v_{x2}\frac{dv_{x2}}{dr} = \left(\eta_h\Omega - \frac{r v_{\theta 2}}{r^2}\right)\frac{d}{dr}(r v_{\theta 2}) \tag{8.3}$$

For a free-vortex distribution, the axial velocity downstream of the fan blades is constant, $v_{x2}(r) = \text{const}$.

Equation (8.3) represents, for specified vortex distribution $r v_{\theta 2}$, an ordinary differential equation for the axial velocity downstream of the fan blades, $v_{x2}(r)$, that can be solved (numerically) in combination with the condition that the axial velocity distribution $v_{x2}(r)$ be consistent with the flow rate Q, i.e.

$$Q = \int_{R_{\text{hub}}}^{R_{\text{fan}}} v_{x2}(r) 2\pi r dr\,, \tag{8.4}$$

where R_{hub} and R_{fan} are the fan hub and tip radii, respectively. Aspects of the (numerical) solution of Eqs. (8.3) and (8.4) are discussed in Appendix B, where it is also shown that a solution of these equations only exists above a minimum flow rate (that depends on the vortex distribution).

With inlet velocities $v_{\theta 1}$, v_{x1} and outlet velocities $v_{\theta 2}$, v_{x2} known (respectively, from the vortex distribution and the solution of Eqs. (8.3) and (8.4)), the required force (per unit spanwise length) exerted by the blades on the flow can be determined through cascade analysis, see for instance [9]. The components of the forces can be expressed in terms of lift and drag forces L and D, respectively (see also Fig. 8.1). In turbomachinery handbooks [9, 139] the lift force is taken as acting at an angle β_m relative to the axial direction. In isolated airfoil theory the lift force is taken as acting at an angle β_1 determined by the direction of the relative inlet velocity vector $\boldsymbol{w}_1$.

It should be noted that in isolated airfoil theory, the flow directions from far upstream and downstream are determined by the direction of $\boldsymbol{w}_1$, since the local deflection due to the presence of the airfoil is negligible. However, in cascade theory the flow deflection results in different directions of the relative inlet and outlet velocity vector $\boldsymbol{w}_1$ and $\boldsymbol{w}_2$, corresponding to the difference between the flow angles β_1 and β_2. The mean flow angle β_m is defined by Eq. (2.16)

$$\tan\beta_m = \frac{1}{2}(\tan\beta_1 + \tan\beta_2)$$

In the cascade theory applied in the current study the lift and drag forces are defined with respect to β_m (as also done in [13, 21, 27]). The lift and drag forces L and D conventionally are scaled with the mean relative velocity w_m (with corresponding lift and drag coefficients C_l and C_d), $C_l = \frac{L}{\frac{1}{2}\rho w_m^2 l}$ with an analogous

definition for C_d. Here l is the chord length of airfoil profile and the magnitude w_m of the mean velocity vector $\boldsymbol{w}_m = \frac{1}{2}(\boldsymbol{w}_1 + \boldsymbol{w}_2)$ is given by $w_m = v_x / \cos\beta_m$.

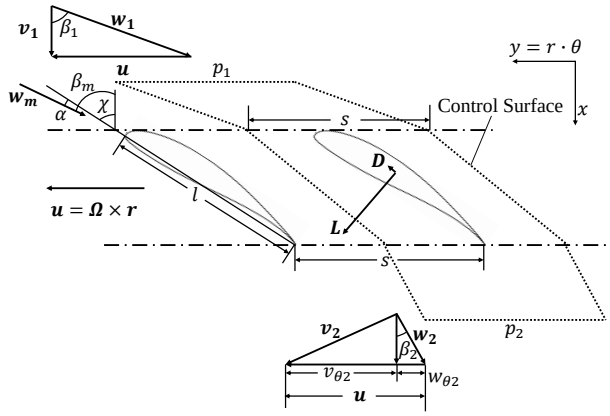

Figure 8.1: Velocities and Forces within a Blade Cascade (schematically): "1" and "2" denote inlet and outlet locations; s is the pitch, l is the chord length; $\boldsymbol{v}$, $\boldsymbol{u}$ and $\boldsymbol{w}$ denote absolute, blade and relative velocity vectors, β_1 and β_2 denote the relative flow angles at inlet and outlet (with respect to the axial direction) respectively, χ denotes the blade stagger angle (with respect to the axial direction); p is pressure; L and D denote lift and drag forces (exerted by the blade on the fluid). The pitch s is given by $s = 2\pi r / Z$ where Z is the number of fan blades.

The conservation law of mass applied to the control surface indicated in Fig. 8.1 gives $v_{x1} = v_{x2} \equiv v_x$. It is assumed that any deviations, due to radial flow, are approximately accounted for by taking $v_x = \frac{1}{2}(v_{x1} + v_{x2})$. As a result of the conservation law of momentum applied to the control surface indicated in Fig. 8.1, it follows that (Eq. (2.18)) [9]:

$$C_l = 2\frac{s}{l}\cos\beta_m(\tan\beta_1 - \tan\beta_2) - C_d \tan\beta_m \,. \tag{8.5}$$

Since the drag coefficient C_d is much smaller than lift coefficient C_l, the last term in the right-hand side of this equation will be neglected here. With a selected lift coefficient distribution, $C_l(r)$, the chord distribution $l(r)$ follows from Eq. (8.5).

From experimental or computational data in the form $C_l = C_l(\alpha)$ and $C_d = C_d(\alpha)$, the required angle of attack α (see also Fig. 8.1) can be determined, if the lift requirement does not exceed its maximum capacity, i.e. $C_l \le C_{l,\max}$. From the angle of attack α, the blade stagger angle χ follows, since $\beta_m = \chi + \alpha$, see also

Fig. 8.1. It should be noted that the stagger angle $\chi(r)$ in the current study is measured relative to the axial direction (contrary to the the stagger angle defined in Refs. [50, 93] where the circumferential direction has been used as reference). The chord length distribution $l(r)$ is determined from Eq. (8.5).

This process can be repeated at a number of spanwise locations. With the stagger angle $\chi(r)$ and the chord length $l(r)$ distributions thus known, the fan blade geometry is determined, up to a (distribution of) blade skew.

In fan design, lift and drag coefficient curves for isolated airfoils are usually employed (for instance using XFOIL [19], see also [104]) for isolated airfoils. For large values of the blade solidity l/s, the flows around the blades in the cascade influence one another. This "interference" effect generally leads to a reduction of the lift coefficient, which can be evaluated approximately through the use of a Weinig lift reduction coefficient K_c. This coefficient has been obtained for cascades consisting of flat plates as well as circular arcs by means of (complex) potential flow theory that involves conformal mappings, see also the book by Lakshminarayana [139].

The selection of the spanwise distribution of the lift coefficient $C_l(r)$ is important to the method. High lift coefficients are desirable, since they result in smaller chord lengths $l(r)$ (see Eq. (8.5)). The specified lift coefficient must not exceed the maximum $C_{l,\max}$ of the blade sections, so $C_l(r) \le C_{l,\max}$. At the hub, the flow deflection is generally large, requiring a large lift coefficient. Small chord lengths near the hub are also required to avoid blade overlap. Therefore, the prescribed lift coefficient at the hub is taken equal to $C_{l,\max}$. At the tip, the lift coefficient should be estimated conservatively ($C_l \le C_{l,\max}$) for better anti-stall characteristics. The interference effect is currently not accounted for. Although this is somewhat oversimplified, the result may be that the overall pressure rise is only slightly influenced, since the contribution of the hub region to the overall pressure rise is fairly small.

The vortex distribution design process gives the distribution of the downstream velocity components $v_{x2}(r)$, $v_{\theta 2}(r)$ and the total pressure $p_{02}(r) - p_{01}$ by Eq. (8.1). The overall, mass-flow weighted pressure rise $\overline{\Delta p_0}$ and dynamic pressure at the outlet $\overline{p_{\mathrm{dyn},2}}$ become

$$\overline{\Delta p_0} = \frac{1}{Q}\int_{R_{\mathrm{hub}}}^{R_{\mathrm{fan}}} v_{x2}(r)\Delta p_0(r) 2\pi r dr \qquad \overline{p_{\mathrm{dyn},2}} = \frac{1}{Q}\int_{R_{\mathrm{hub}}}^{R_{\mathrm{fan}}} v_{x2}(r)\left[\frac{1}{2}\rho\left(v_{x2}^2(r) + v_{\theta 2}^2(r)\right)\right] 2\pi r dr . \tag{8.6}$$

The total-to-static efficiency η_{ts} is determined by

$$\eta_{\mathrm{ts}} = \eta_h\left(1 - \frac{\overline{p_{\mathrm{dyn},2}}}{\overline{\Delta p_0}}\right). \tag{8.7}$$

In the present analysis, an estimated hydraulic efficiency η_h is taken into consideration, to obtain better agreement between the specified target pressure rise and the actual pressure rise (either from CFD simulations or from experiments). From simplicity, the hydraulic efficiency η_h has been assumed to be uniform in spanwise direction. This hydraulic efficiency is present in Eqs. (8.1), (8.3) and (8.7). The incorporation of the hydraulic efficiency η_h forms a (small) extension of the method by Bamberger and Carolus [13] (whose objective was the determination of the *maximum attainable* total-to-static efficiency) that is considered to be important to ensure that the desired duty point is attained by designs resulting from the vortex distribution design method.

The analysis is shown here in dimensional form, for physical clarity, while Bamberger and Carolus [13] expressed it in dimensionless form employing the dimensionless radius r^* and the dimensionless axial and circumferential velocity components, φ_{x2} and $\varphi_{\theta 2}$ respectively, defined by

$$r^* = \frac{r}{R_{\text{fan}}} \qquad \varphi_{x2} = \frac{v_{x2}}{\Omega R_{\text{fan}}} \qquad \varphi_{\theta 2} = \frac{v_{\theta 2}}{\Omega R_{\text{fan}}}\,. \tag{8.8}$$

Although this two-dimensional vortex distribution design method is based on strong assumptions, primarily the absence of radial flow, backflow near the hub and tip leakage, it is considered to capture the essential physics of the three-dimensional flow fields expected in axial fans. Of course, the adequacy of this design method needs to be established via CFD simulations and/or experimental tests.

8.3 Selection of Vortex Distribution

The vortex distribution forms an important degree of freedom in the vortex design method. An additional degree of freedom is the hub-tip diameter ratio κ (or the hub diameter). The simplest vortex distribution is the free-vortex distribution, $r\,v_{\theta 2}(r) = \text{const}$.

Bamberger and Carolus [13] studied how the vortex distribution can be selected such that the maximum ideal total-to-static efficiency, $\eta_{\text{ts.idmax}}$, is obtained. In their analysis, the kinetic energy at outlet of the fan blades is considered to form the most dominant loss. In the optimisation of this efficiency $\eta_{\text{ts.idmax}}$, the target total pressure coefficient ψ_{tt} and flow coefficient φ form constraints; the degrees of freedom are formed by the dimensionless vortex distribution $r^*\varphi_{\theta 2}$ and the HTR κ. They have not considered restrictions with respect to detailed cascade flow analysis, such as the required lift coefficient distribution and limits with respect to the flow deflection. Bamberger and Carolus [13] only considered

linear distributions of the vortex distribution, $r v_{\theta 2}(r) = A + Br$. A free-vortex distribution is retrieved from their representation when $B = 0$.

8.3.1 Free-vortex design

With a free-vortex distribution, it follows from Eq. (8.3) that the dimensionless axial velocity $\varphi_{x2} = \text{const}$. From Eq. (8.4) and Eq. (8.6), it follows that for a free-vortex distribution, the dimensionless velocities defined in Eq. (8.8) are given in terms of the dimensionless flow coefficient φ and total pressure rise coefficient ψ_{tt} by

$$\varphi_{x2}(r^*) = \frac{\varphi}{1-\kappa^2} \qquad \varphi_{\theta 2}(r^*) = \frac{\psi_{\text{tt}}}{2\eta_h r^*}\,. \tag{8.9}$$

With decreasing hub-to-tip diameter ratio κ, the dimensionless axial velocity φ_{x2} decreases and the dimensionless circumferential velocity $\varphi_{\theta 2}$ increases. This suggests that for free-vortex distributions an optimal hub-to-tip diameter ratio, denoted by κ_{opt}, may exist for which the ideal total-to-static efficiency is maximal. With the dimensionless velocities downstream of the fan blades given by Eq. (8.9), the ideal total-to-static efficiency in Eq. (8.7) becomes (after some algebra)

$$\eta_{\text{ts}} = \eta_h - \frac{\psi_{\text{tt}}}{\eta_h}\left[\left(\frac{\varphi\eta_h}{\psi_{\text{tt}}}\right)^2 \frac{1}{(1-\kappa^2)^2} + \frac{\ln\kappa}{2(1-\kappa^2)}\right]. \tag{8.10}$$

Therefore, the total-to-static efficiency η_{ts} for a free vortex design is a function of η_h, κ and operation duty point (φ, ψ_{tt}). The variation of the ideal (with $\eta_h = 100\%$) total-to-static efficiency η_{ts} with κ is shown in Fig. 8.2 for three design duty points. For different design duty points with the same ratio φ/ψ_{tt}, a vertical scaling (determined by the value of ψ_{tt}/η_h) of the η_{ts} curve is obtained.

The optimal hub-tip-ratio κ_{opt} is obtained by finding the value of κ for which $\frac{\partial\eta_{\text{ts}}}{\partial\kappa} = 0$. It follows after some algebra that this value κ_{opt} satisfies the equation

$$\eta_h \frac{\varphi}{\psi_{\text{tt}}} = \frac{1}{2}\sqrt{\frac{1}{2\kappa_{\text{opt}}^2}(1-\kappa_{\text{opt}}^2)^2 + (1-\kappa_{\text{opt}}^2)\ln\kappa_{\text{opt}}}\,. \tag{8.11}$$

This equation gives for a *free-vortex distribution* the optimum value for the hub-tip ratio (κ_{opt}) for a specific design duty point ($\varphi, \psi_{\text{tt}}$). To the authors' best knowledge, this is the first time that such an equation is given in investigations of rotor-only axial fans.

Surprisingly, Eq. (8.11) is identical to that for the hub-to-tip diameter ratio in the Strscheletzky criterion for the backflow region (shown in the book by Eck [8] in his FIG.251). According to Castegnaro [11], the Strscheletzky criterion is "still

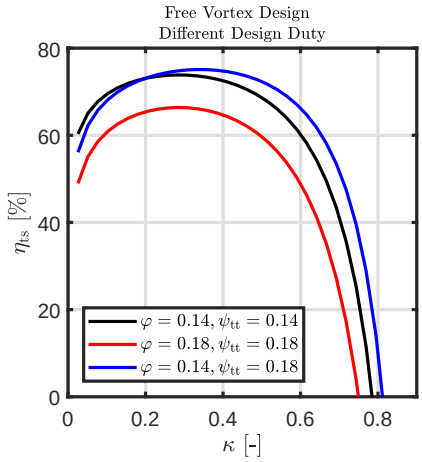

Figure 8.2: Free vortex designs: variation of the ideal total-to-static efficiency η_{ts} with HTR κ and design duty points; η_h = 100%.

the only analytic method that allows a computation of the hub-to-tip ratio". Some additional information on the Strscheletzky criterion is given in Appendix A.

8.3.2 Polynomial vortex distribution

Theoretically there is an infinite number of possibilities with respect to the vortex distribution. For example, a linear distribution ($r v_{\theta 2} = Ar + B$) is employed in the initial design consideration in Wallis's book [21] as well as in Refs. [13, 121]. A power-law function for the vortex distribution is used in Ref. [85]. A more general form has been suggested by Horlock [151] and employed by Carolus & Starzmann [104] where the vortex distribution is expressed as a polynomial in the dimensionless radius r^*:

$$r^* \varphi_{\theta 2}(r^*) = \frac{\psi_{tt}}{2\eta_h} \sum_{i=0}^{M} a_i (r^*)^i \tag{8.12}$$

where a_i are constants ($i = 0 \ldots M$). Note that in this expression, the vortex distribution is scaled here with respect to the free-vortex distribution, see Eq. (8.9). The free-vortex distribution corresponds to $M = 0$. In the current study, linear, quadratic and cubic distributions, corresponding to $M = 1, 2, 3$ respectively, are also investigated.

Differently from the analytic expression for the free-vortex distribution in Sec. 8.3.1, a numerical method has to be employed to find the distribution of $r^*\varphi_{\theta 2}$ that gives the optimal total-to-static efficiency $\eta_{\text{ts,max}}$. With a_i $(i = 0 \dots M)$ and κ as degrees of freedom, at specified duty point ψ_{tt} (or ψ_{ts}) and φ, the optimisation problem is described by a constrained nonlinear function η_{ts} in multiple variables (or degrees of freedom).

The method of calculating the optimal ideal achievable total-to-static efficiency $\eta_{\text{ts.max}}$ described above has been implemented in Matlab, using a constrained nonlinear multivariable function optimiser ("fmincon" function using the 'interior-point' algorithm). An extra constraint $\tan\beta_2 > 0$ is imposed to ensure that the optimized value of $r^*\varphi_{\theta 2}$ results in a realistic outlet circumferential velocity distribution $v_{\theta 2}(r)$ for rotor-only axial fans. Initial values and search ranges for the vortex distribution $r^*\varphi_{\theta 2}$ and the HTR κ are based on the optimum values for a free vortex distribution (see Eqs. (8.9) and (8.11)). The output parameters are the maximum value $\eta_{\text{ts.max}}$, the optimum κ_{opt}, the (dimensionless) vortex distribution $r^*\varphi_{\theta 2}(r^*)$ and the downstream (dimensionless) velocity components $\varphi_{x2}(r^*)$, $\varphi_{\theta 2}(r^*)$.

As a consistency check of the optimised result, an alternative optimisation algorithm (Differential Evolution Method [152], known for its robustness and flexibility, see for example, [128]) has also been employed, essentially giving the same optimal results.

8.4 Case Study: Design Duty and Results

The vortex design method described in Sec. 8.2 is applied to a baseline fan with small HTR as reported in Ref. [50], of which the detailed geometrical parameters and measurements data are known and for which the CFD simulation strategy has been validated.

8.4.1 Fan Configuration and Design Parameters

Each of the six identical blades consists of a "main blade" and a "nonairfoil part". Based on the reported simulation strategy for axial fans with small HTR [50], only the "main blade" is considered; the tip gap is not taken into consideration here, and hence $D_{\text{fan}} = D_{\text{casing}}$. The HTR of the baseline fan is $\kappa = 0.18$. The BEP is selected as design duty point.

The dimensionless geometrical and design parameters for the baseline fan are summarised in Table 8.1. It should be noted that the total pressure coefficient ψ_{tt} is obtained from the CFD simulations as reported in Refs. [50, 93] as it could not be obtained from the available measured data. Since the CFD simulation results have been validated with respect to the pressure coefficient ψ and the

total-to-static efficiency η_{ts}, the predicted value of the pressure coefficient ψ_{tt} is considered to be reliable.

Table 8.1: Dimensionless Geometrical and Design Parameters of the Baseline Fan.

Hub-tip Diameter Ratio κ [-]	0.18
Airfoil Type	Wortmann Profile
Solidity at Tip of Main Blade [-]	0.155
Solidity at Hub of Main Blade [-]	0.844
Design Flow Coefficient φ [-]	0.154
Design Pressure Coefficient ψ [-]	0.101
Design Total Pressure Coefficient ψ_{tt} [-]	0.138
Specific Speed σ [-]	1.873
Specific Diameter δ [-]	1.513

In order to obtain comparable results in the design study, the same Wortmann profile with round trailing edge of the baseline fan has been selected as the shape of the blade sections. The point of maximum thickness of the Wortmann profile is chosen as stacking point for each spanwise location.

The dependence of the lift and drag coefficients on the angle of attack α have been predicted with XFOIL [19, 104] for a large Reynolds number $\mathrm{Re} = 5 \times 10^5$, see Fig. 8.3(a) and (b). The maximum lift coefficient $C_{l.\max} = 1.8$ at angle of attack α around 10°.

Considerations on the choice of the lift coefficient distribution $C_l(r)$ are given in Sec. 8.2. A linear spanwise variation has been considered here, with $C_{l.\mathrm{hub}} = C_{l.\max}$ at the hub. At the tip, the lift coefficient has been selected conservatively, $C_{l.\mathrm{tip}} = 1.3$, for a better stall margin. The hydraulic efficiency η_h is estimated as 85%, based on CFD results in [50] and also applied in Ref. [123].

8

8.4.2 Design Results

The optimisation of the total-to-static efficiency η_{ts} described in Sec. 8.2 provides the optimized vortex distribution $(r^*\varphi_{\theta 2})$ with corresponding $\eta_{ts.\max}$, optimal HTR κ_{opt} as well as the distributions of the blade geometrical parameters, stagger angle $\chi(r^*)$ and of the solidity $l(r^*)/s(r^*)$.

The optimized vortex distribution $(r^*\varphi_{\theta 2})$, optimal HTR κ_{opt} and corresponding axial velocity coefficient $\varphi_{x2}(r^*)$ are summarized in Fig. 8.4(a) and (b). With increasing number of degrees of freedom in $r^*\varphi_{\theta 2}$, the optimal κ_{opt} and the value of $r^*\varphi_{\theta 2}$ near the hub decrease, which agrees with the indications in Wallis's book [21]. At the tip, the values of $r^*\varphi_{\theta 2}$ for the polynomial vortex distribution designs

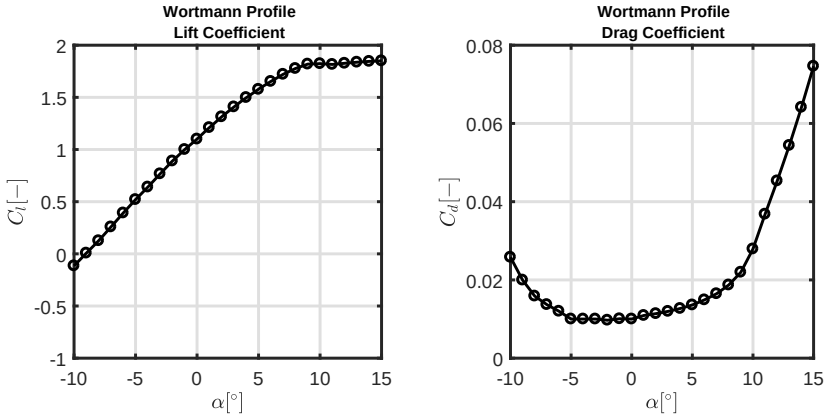

(a) (b)

Figure 8.3: Performance of An Isolated Wortmann Profile, as Predicted with XFOIL [19], as Function of Angle of Attack α; (a) Lift Coefficient $C_l(\alpha)$, (b) Drag Coefficient $C_d(\alpha)$.

are larger than for the free vortex design; the maximum value is obtained for the linear vortex distribution design ($M = 1$).

The spanwise variation of the axial velocity coefficient φ_{x2} is shown in Fig. 8.4(b). For the free vortex design, the constant value design equals the design duty $\varphi = 0.154$; for the other designs, $\varphi_{x2}(r^*)$ effectively increases monotonically, except the quadratic and the cubic distribution vortex designs ($M = 2$ and 3) that show a small increase towards the hub and the quadratic vortex distribution ($M = 2$) shows a small drop near the tip. With increasing value of M, the non-uniformity of the downstream axial velocity distribution increases.

The maximum total-to-static efficiency $\eta_{\text{ts.max}}$ for the different vortex designs are listed in Table 8.2. A larger polynomial degree M, with a larger number of degrees of freedom in the optimisation process, gives a larger $\eta_{\text{ts.max}}$, but with decreasing increments. It can be inferred that there is a limitation for $\eta_{\text{ts.max}}$ for (even) larger polynomial degree M.

Table 8.2: Design Results: Optimal Total-to-static Efficiency $\eta_{\text{ts.max}}$ for Different Degree M of the Polynomial Vortex Distribution Designs.

M	0	1	2	3
$\eta_{\text{ts.max}}$	56.66%	57.78%	58.17%	58.40%

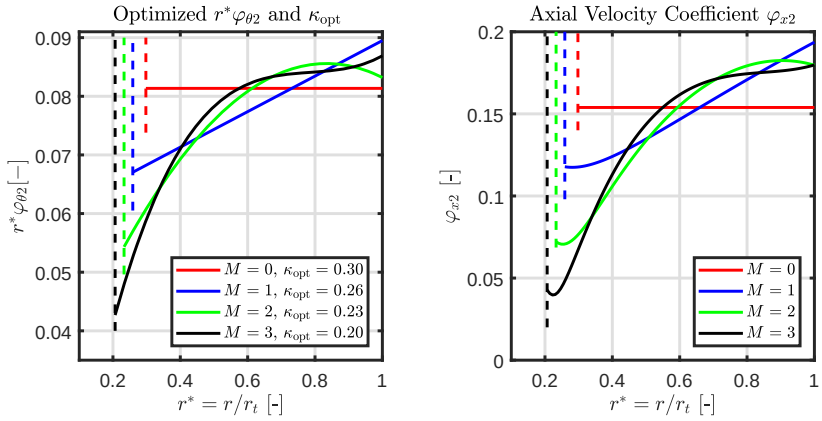

Figure 8.4: Design Results: (a) Optimized Dimensionless Vortex Distribution $r^*\varphi_{\theta 2}(r^*)$, (b) Corresponding Axial Velocity Coefficient Distribution $\varphi_{x2}(r^*)$; for various values of the degree M of the polynomial expression in Eq. (8.12), with corresponding optimal HTR κ_{opt} indicated by the dotted vertical lines.

The resulting distributions of the stagger angle $\chi(r^*)$ and the solidity $l(r^*)/s(r^*)$ for different vortex distributions $r^*\varphi_{\theta 2}(r^*)$ (corresponding to $M = 0,1,2,3$) are shown in Fig. 8.5(a) and (b), together with data for the baseline fan.

For the stagger angle, the variations in stagger angle are much smaller for the baseline fan than for the optimised designs. Compared with baseline design, smaller and larger χ are found for the free and polynomial vortex distribution designs at the hub and the tip, respectively. Near the hub, the smallest χ is about 35°for by the linear vortex distribution ($M = 1$); for other designs, χ at the hub ranges between 37° and 40°. From mid span towards the tip, the stagger angles χ of all vortex designs converge to each other at about 78°.

For the solidity, the variations in solidity are much smaller for the baseline fan than for the optimised designs. Compared with the baseline design, larger and nearly the same solidity are found for the free and polynomial vortex designs at the hub and the tip, respectively. High solidity values (≥ 1) are found near the hub. This is due to the small HTR for the designs with $M \geq 2$, with corresponding small pitch s. From hub towards mid span, the solidity rapidly decreases to values $\frac{l}{s} < 1$. Similarly as with the stagger angle distributions, the solidity distributions of the free and polynomial vortex distribution designs differ from each other mainly near the hub. The largest values are exhibited by the linear and quadratic vortex designs, while the lowest value is given by the free vortex

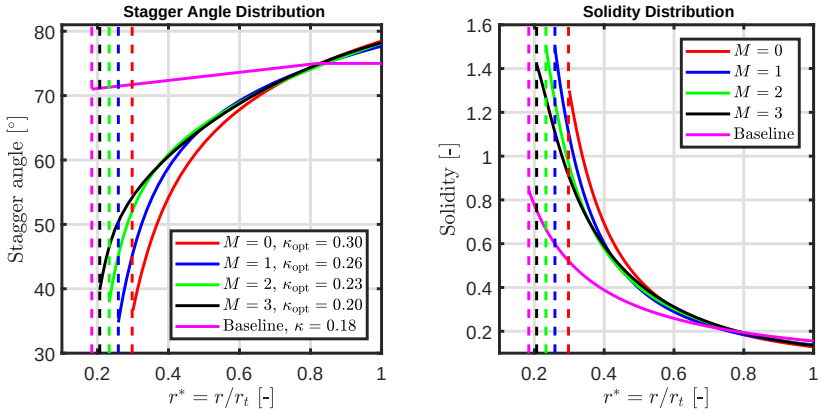

(a) (b)

Figure 8.5: Baseline Case and Design Results for Different Vortex Distribution: (a) Stagger Angle Distribution $\chi(r^*)$, (b) Solidity Distribution $l(r^*)/s(r^*)$; the dotted vertical lines indicate κ_{opt}.

design (with higher κ).

For both stagger angle and solidity distributions, the values of the free and polynomial vortex distribution designs converge to the same value as that for the baseline case from spanwise location $r^* = 0.8$ and larger r^*.

8.5 Predicted Aerodynamic Performance of Designs

In order to investigate the effects of the vortex distribution on the aerodynamic performance, CFD results for blades designed with the four different vortex distributions from Sec.8.3 are compared to that of the baseline case in Secs. 8.5.1 to 8.5.4. The aerodynamic performance curves are shown first, followed by analyses of the flow fields to better understand the origins of the observed effects.

The discussed overall aerodynamic parameters are pressure coefficient ψ, total pressure coefficient ψ_{tt}, total-to-static efficiency η_{ts} and total-to-total efficiency η_{tt}. Six flow coefficients are considered: low flow coefficient (φ near 0.10 and 0.13), near BEP (φ near 0.15) and larger flow coefficients (φ near 0.19, 0.21, and 0.23). The performance curves are created by cubic spline interpolation through the six data points obtained from the CFD simulations. Since the resulting characteristics of ψ and ψ_{tt} are nearly the same, only the results of ψ are shown.

8.5.1 Free-Vortex Distribution Design

The predicted aerodynamic performance with the free-vortex designed fan blades is shown in Fig. 8.6.

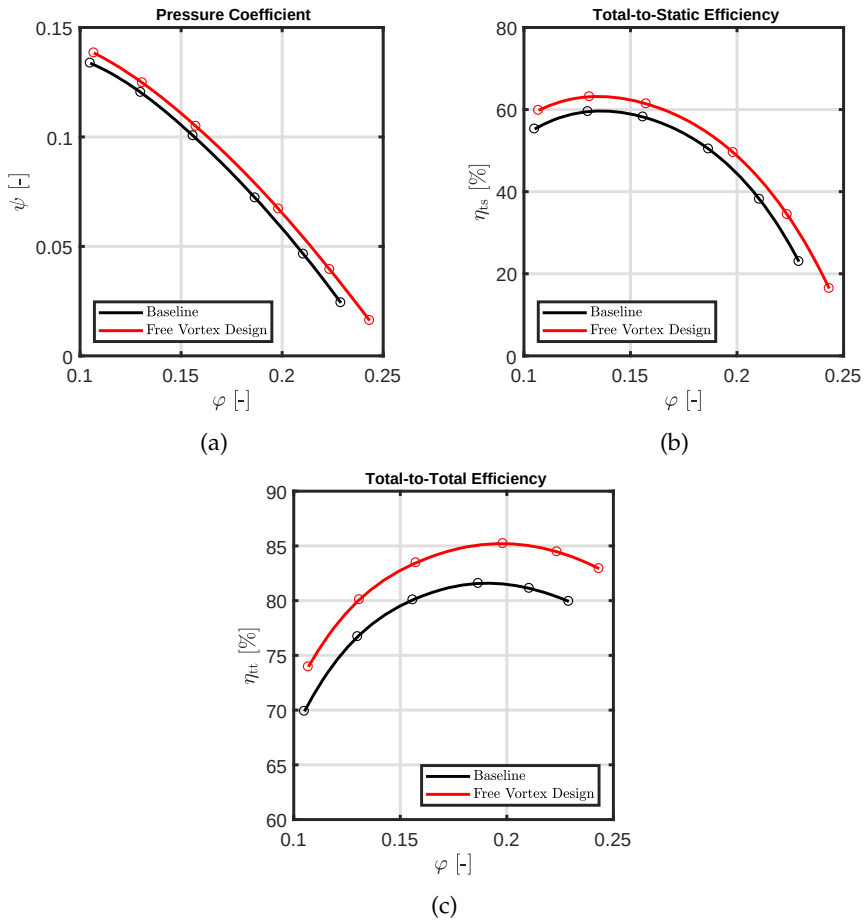

Figure 8.6: Comparison between CFD Predictions for the Baseline Fan and for the Fan with the Free Vortex Distribution Design: (a) Pressure Coefficient ψ, (b) Total-to-static Efficiency η_{ts} and (c) Total-to-total Efficiency η_{tt}.

For the pressure coefficient ψ and the total pressure coefficient ψ_{tt}, the free-vortex design gives improved performance compared to the baseline case. At the design duty point, the improvements in ψ and ψ_{tt} are 4.4% and 3.0%, respectively.

For the total-to-static efficiency η_{ts} and the total-to-total efficiency η_{tt}, significant improvements are found. Near the design duty point φ around 0.15, the improvement in η_{ts} is about 3.5%. For η_{tt}, the largest increase is 4.0% near large flow coefficient $\varphi = 0.23$ and the improvement of η_{tt} near $\varphi = 0.15$ is about 3.6%. Therefore, the current design method is able to improve both total-to-static and total-to-total efficiency, while achieving the desired pressure rise.

As reported in Refs. [50, 93], backflow downstream of the baseline rotor (with small HTR $\kappa = 0.184$) is present for low to high flow coefficients ($\varphi = 0.10 - 0.23$). For the free-vortex fan design with higher $\kappa = 0.30$ and improved aerodynamic performance, the flow streamlines in the meridional plane are investigated first at φ near 0.10 and 0.15. The results in Fig. 8.7 show that a limited backflow region is found at flow coefficient φ near 0.1, but no backflow is present near the design duty point φ near 0.15. The hub corner stall is not found. Therefore, the losses due to secondary flow are significantly decreased by the free-vortex designed fan blade with $\kappa_{opt} = 0.3$.

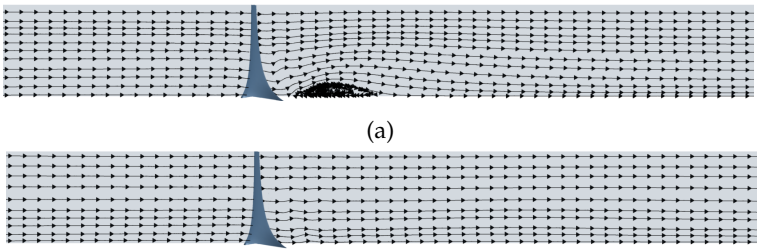

(a)

(b)

Figure 8.7: Comparison of Meridional Surface Streamlines of Fan with Free-vortex Design for Different Flow Coefficients: (a) φ near 0.10, (b) φ near 0.15 (design point).

The relative flow streamlines in the Blade-to-Blade (*B2B* in short) view have been analysed: no separation is found for all flow coefficients at all spanwise sections. Since flow separation is more likely to occur at low flow coefficients, and in order to avoid repetition, only the streamlines in B2B plane at the hub, mid and tip spanwise locations at φ near 0.10 are shown in Fig. 8.8. No separation is observed, which demonstrates that the spanwise stagger angle distribution $\chi(r)$ has been well designed.

8.5.2 Linear Vortex Distribution Design

The optimal HTR for the linear vortex distribution is $\kappa_{opt} = 0.26$. According to the Strscheletzky criterion represented by Eq. (8.11) (and obtained from free-vortex

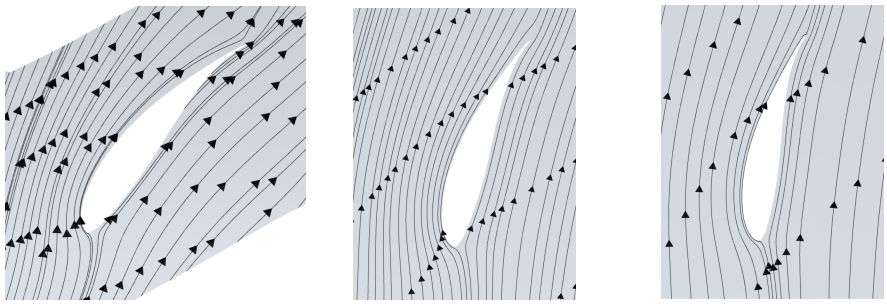

(a) (b) (c)

Figure 8.8: Velocity Streamlines based on the Relative Velocity in the Blade-to-blade Plane at Different Spanwise Locations for the Free-vortex Design Blade at Low Flow Coefficient φ near 0.10: (a) Near Hub, (b) Midspan, and (c) Near Tip.

analysis), for the current design duty the critical value for the occurrence of backflow is $\kappa = 0.30$. Therefore, for the design with linear vortex distribution, backflow could be expected.

The predicted aerodynamic performance for the optimal fan design based on a linear vortex distribution is shown in Fig. 8.9.

For both pressure coefficient ψ and total pressure coefficient ψ_{tt}, the linear vortex distribution design fan blade matches the performance of the baseline fan (and hence satisfies the required duty point) at all flow rates, except at low flow coefficients φ near 0.10.

Improvements are found in both total-to-static and total-to-total efficiency η_{ts} and η_{tt}. For η_{ts}, the maximum improvement is 3.9% at flow coefficient φ near 0.13; at the design duty point (φ near 0.15), the increase in η_{ts} is 3.3%; at large φ, the improvement is smaller. For η_{tt}, larger improvements are found at larger φ; at φ near 0.23, the improvement is about 4.3%.

The reduced pressure performance at low flow coefficient (φ near 0.10) indicates that more losses are present for the linear vortex distribution designed blade, in comparison with the baseline case. The streamlines in the meridional plane for φ near 0.10 are shown in Fig. 8.10 for both cases. This shows that the radial extent of backflow region is larger for the baseline case, while the axial extent is larger for the linear vortex distribution designed fan. Therefore, the backflow region may not be the direct reason for lower pressure performance. Hence, potential flow separations in B2B plane are investigated next.

For both the baseline and linear vortex distribution design fan, the relative velocity streamlines in the B2B view near mid span and near tip show no separation

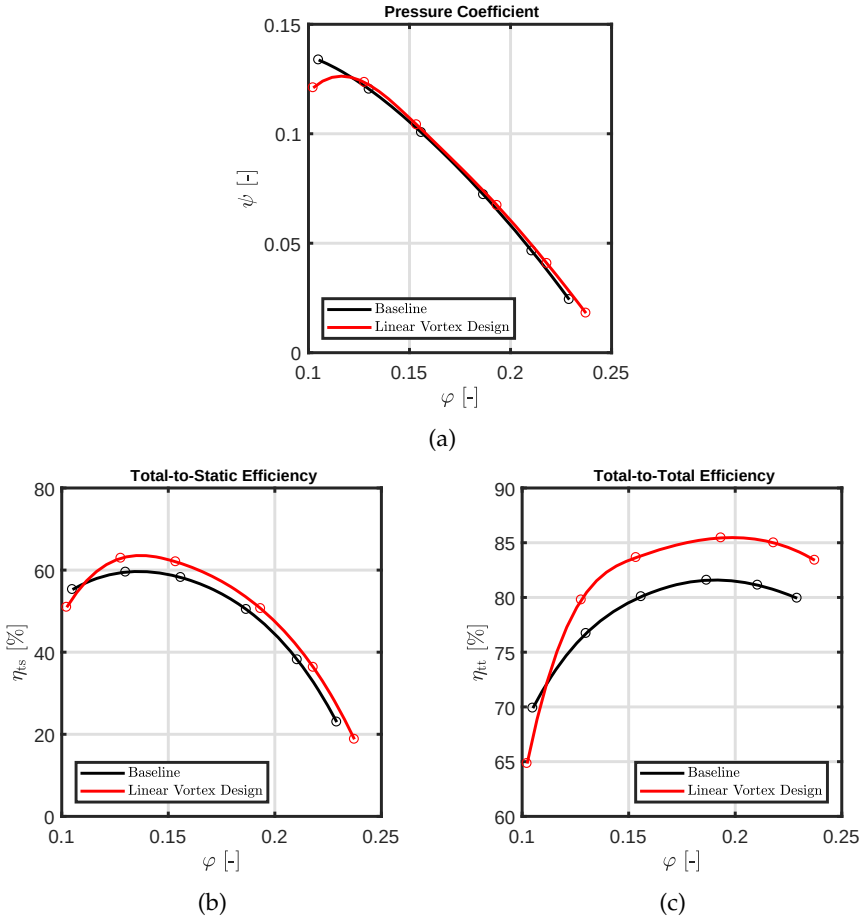

Figure 8.9: Comparison between CFD Predictions for the Baseline Fan and for the Fan with the Linear Vortex Distribution Design: (a) Pressure Coefficient ψ, (b) Total-to-static Efficiency η_{ts} and (c) Total-to-total Efficiency η_{tt}.

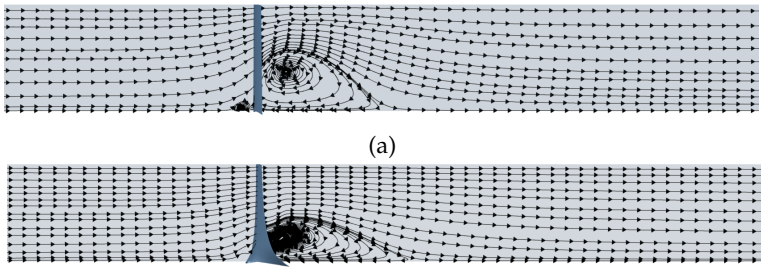

(a)

(b)

Figure 8.10: Comparison of Meridional Surface Streamlines for Flow Coefficient φ near 0.10: (a) Baseline Fan, (b) Linear Vortex Distribution Design Fan.

(figure not shown). However, near the hub, extensive separations are found for the linear vortex distribution design, as shown in Fig. 8.11. The separations and the larger blade surface area (larger chord length, see Fig. 8.5) near the hub of the linear vortex distribution design fan contribute to larger losses and the drops in the pressure coefficients (both ψ and ψ_{tt}) for low flow coefficient.

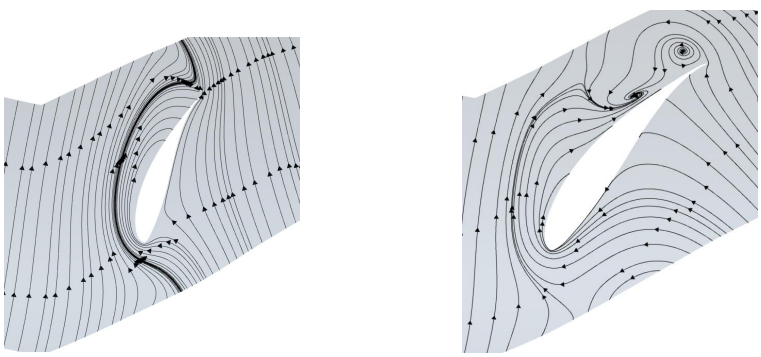

(a) (b)

Figure 8.11: Velocity Streamlines based on the Relative Velocity in the Blade-to-blade Plane near the Hub for Low Flow Coefficient φ near 0.10: (a) Baseline Case (b) Linear Vortex Distribution Design Fan.

Further investigations of the flow fields have shown that at the medium and

larger flow coefficients, neither backflow nor separation is found in the meridional and the blade-to-blade view, respectively, which corresponds to the improved performance shown in Fig. 8.9. In order to avoid repetition, the detailed figure is not shown.

8.5.3 Quadratic Vortex Distribution Design

The optimal HTR with a quadratic vortex distribution is $\kappa_{opt} = 0.23$. Based on the Strscheletzky criterion (developed for free-vortex distributions), backflow may be expected for this design. The predicted aerodynamic performance of the quadratic vortex distribution design fan is shown in Fig. 8.12.

Compared with the free vortex and the linear vortex distribution design, the quadratic vortex distribution design results in a pressure reduction at low flow coefficient φ near 0.10 and 0.13. Yet, the design duty (φ near 0.15) is still satisfied for both pressure coefficient ψ and total pressure coefficient ψ_{tt}.

For the efficiency, improvements are found for $\varphi > 0.13$. Near the design duty point, the improvement of the total-to-static efficiency η_{ts} and total-to-total efficiency η_{tt} are 2.4% and 3.2%, respectively.

The meridional surface streamlines have been analysed at both low flow coefficient φ near 0.10 and at the duty point φ near 0.15. Backflow is present for both cases, the results at φ near 0.15 are shown in Fig. 8.13.

Differently from the linear vortex distribution design, the quadratic vortex distribution design results in a lower pressure rise at flow coefficient φ near 0.10 and 0.13. The relative velocity streamlines on the B2B plane near the hub show that with increased flow coefficient φ, flow separations on the suction side of blade section become less significant and smaller vortex extents near the trailing edge are found. However, separations are present, even at φ near 0.15 (design duty). Combining the investigations in Fig. 8.11, the backflow together with the large stagger angles near the hub result in the observed flow separations near the hub.

Further investigations have shown that at mid-span and tip locations, no separation is found in the B2B plane for all flow coefficients φ and that the flow patterns are similar with what is shown in Fig. 8.8. The detailed figure is not shown to avoid repetition.

8.5.4 Cubic Vortex Distribution Design

The optimal HTR with a cubic vortex distribution is $\kappa_{opt} = 0.20$. Based on the Strscheletzky criterion (developed for free vortex distributions), backflow may be expected for this design. The predicted aerodynamic performance of the cubic vortex distribution design is shown in Fig. 8.14. For the pressure coefficient ψ and

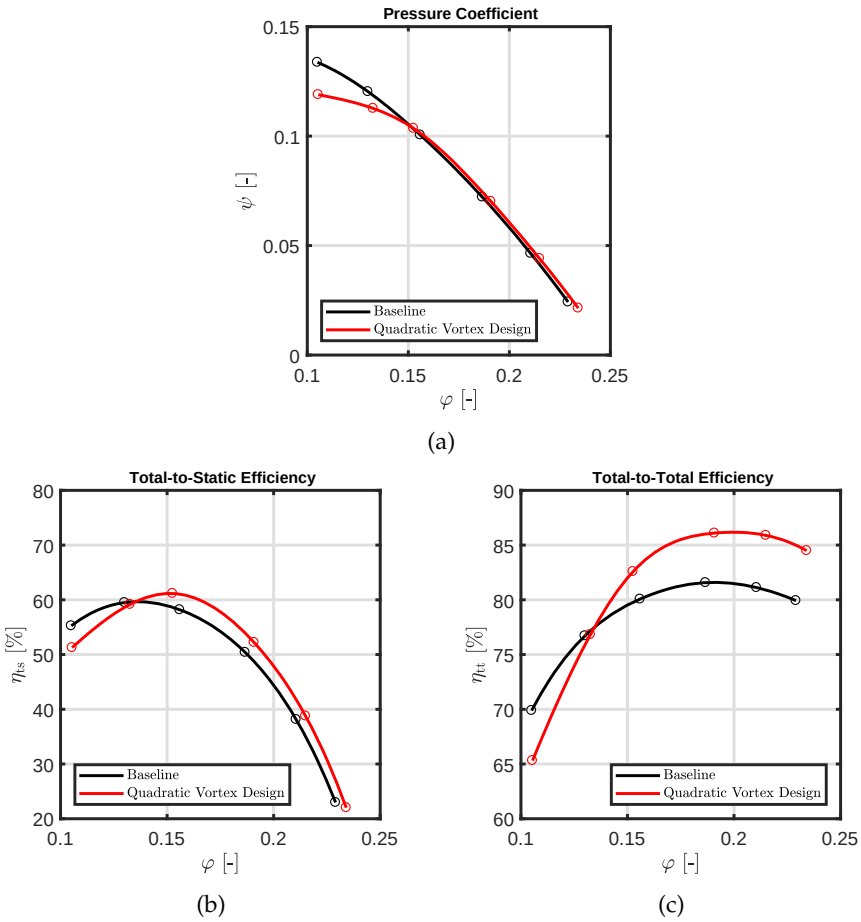

Figure 8.12: Comparison between CFD Predictions for the Baseline Fan and for the Fan with the Quadratic Vortex Distribution Design: (a) Pressure Coefficient ψ, (b) Total-to-static Efficiency η_{ts} and (c) Total-to-total Efficiency η_{tt}.

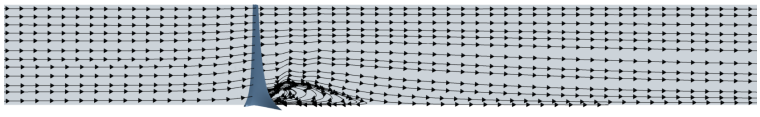

Figure 8.13: Meridional Surface Streamlines for the Quadratic Vortex Distribution Design for Flow Coefficient φ near 0.15.

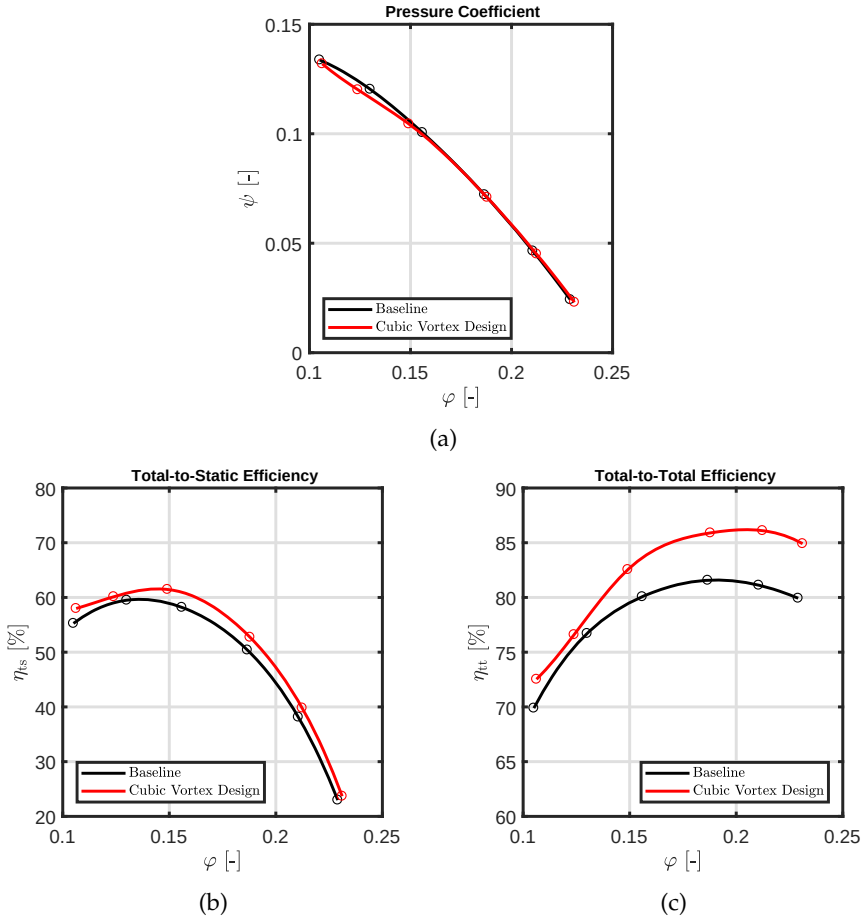

Figure 8.14: Comparison between CFD Predictions for the Baseline Fan and for the Fan with the Cubic Vortex Distribution Design: (a) Pressure Coefficient ψ, (b) Total-to-static Efficiency η_{ts} and (c) Total-to-total Efficiency η_{tt}.

the total pressure coefficient ψ_{tt}, similarly to the quadratic vortex distribution design, a reduced performance is given by the cubic vortex design at low flow coefficient φ near 0.10 and 0.13. Yet, the required pressure rise is satisfied at the duty point and for larger φ.

For the total-to-static and total-to-total efficiency η_{ts} and η_{tt}, improvements are found for all flow coefficients φ. The maximum improvement of η_{ts} is 1.9% at φ near 0.15 and for η_{tt} it is 4.6% at φ near 0.20.

The meridional flow field analysis showed that the overall flow patterns for the cubic vortex distribution design (data not shown) are similar to those for the quadratic vortex distribution design: backflow is present for low flow coefficient and near design duty; the B2B surface streamlines are similar to those for quadratic vortex distribution design.

8.5.5 Overview of CFD results

The results in the previous sections have shown that the design duty (for pressure coefficient ψ as well as total pressure coefficient ψ_{tt}) can be achieved by all optimal vortex distributions. The overview of all CFD predictions in this section focuses on: (i) the total-to-static and total-to-total efficiencies, η_{ts} and η_{tt}; (ii) the absence/presence of backflow in relationship to (φ/ψ_{tt}, κ) values and the Strscheletzky criterion.

The predicted *maximum* total-to-static and total-to-total efficiencies $\eta_{ts.max}$ and $\eta_{tt.max}$ for all vortex distribution design fans (characterised by the polynomial degree M in Eq. (8.12)) are given in Fig. 8.15, together with the baseline results as reference.

The optimal free and polynomial vortex distributions give significant improvements in both $\eta_{ts.max}$ and $\eta_{tt.max}$. For $\eta_{ts.max}$, the linear vortex distribution ($M = 1$) gives the highest improvement by 3.9%; lower improvements are found for the quadratic and the cubic vortex distribution ($M = 2$ and 3).

It should be noted that the CFD results for η_{ts} at the design point are slightly larger (by 3.7% in average) than the design results shown in Table 8.2. This may be due to various reasons, such as: (i) the spanwise constant estimate of the hydraulic efficiency η_h and (ii) radially outward flow in the CFD simulations in contrast to the two-dimensional flow assumed in the vortex design method. This gives an increased flow towards the lighter loaded mid span to tip blade sections.

For the maximum total-to-static efficiency $\eta_{tt.max}$, a larger improvement is found for larger M. The increase in $\eta_{tt.max}$ for the quadratic and the cubic vortex distribution designs are both around 4.6%. This tendency of improved $\eta_{tt.max}$ with respect to the polynomial degree M in the vortex distribution is related to the reduced HTR κ_{opt} for larger M. A smaller value of κ corresponds to smaller a

axial velocity, and hence reduced hydraulic losses. A similar conclusion has been reported by Masi et al. [124].

By reducing the axial velocity, it is expected that $\eta_{\text{ts.max}}$ increases due to decreased exit losses (dynamic pressure). However, it can be observed from the CFD results in Fig. 8.15 that the designs with smaller κ (corresponding to large M) do not necessarily result in improved $\eta_{\text{ts.max}}$. A possible explanation from Bamberger and Carolus [13] is that the potential of improving η_{ts} by reducing κ has already been largely exploited by the current optimization method. This agrees with the results in Table 8.2 showing a diminishing increase of η_{ts} with increasing M. However, the CFD results for the small HTR cases show backflow, which leads to a drop in the aerodynamic performance.

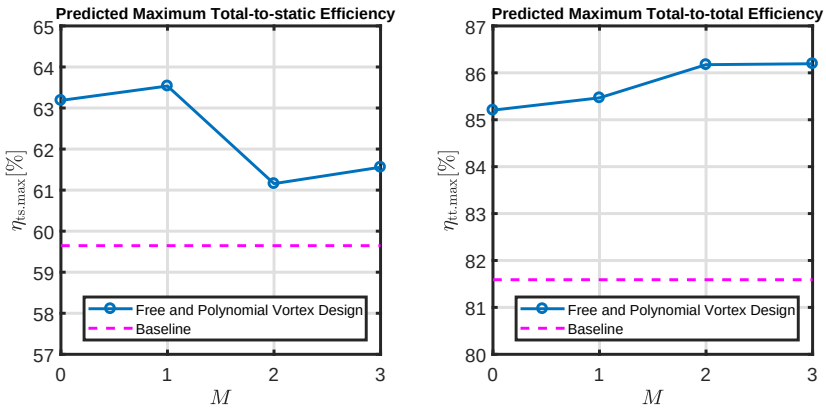

Figure 8.15: Predicted Maximum Efficiency as Function of Polynomial Degree M of the Vortex Distribution in Eq. (8.12): (a) Total-to-static Efficiency $\eta_{\text{ts.max}}$, (b) Total-to-total Efficiency $\eta_{\text{tt.max}}$. The efficiency of the baseline fan is shown as reference.

For both efficiencies, free and polynomial vortex designs give improvements (compared with baseline case) in the range of flow coefficients $\varphi > 0.15$. At φ near 0.10, the linear and the quadratic vortex distribution designs show a lower performance; at φ near 0.13, similar efficiencies are found for the quadratic vortex distribution and improvements are obtained for the other vortex distribution designs.

To assess the accuracy of the Strscheletzky backflow criterion, all CFD results have been analysed for the occurrence or absence of backflow in the meridional plane. The results are shown in Fig. 8.16. Since the Strscheletzky criterion involves $\varphi/\psi_{tt.id}$, where $\psi_{tt.id}$ is the ideal pressure coefficient, the corresponding

variable for the CFD simulations is $\varphi\eta_{tt}/\psi_{tt}$ (since $\psi_{\text{tt.id}} = \psi_{\text{tt}}/\eta_{\text{tt}}$). The results indicate that the Strscheletzky criterion does not accurately "separate" the cases with backflow from those without. However, the criterion works well as a *conservative* preliminary estimate for the presence of backflow, even for non-free vortex distributions, since only one case with backflow occurs in the “safe" area for the Strscheletzky criterion.

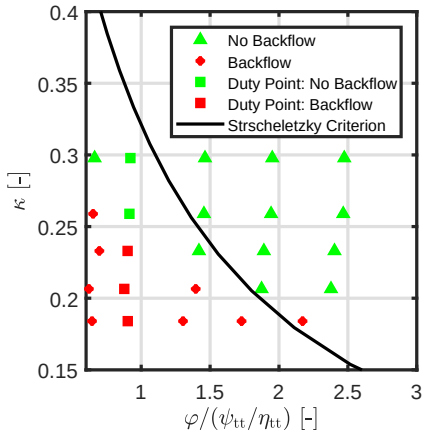

Figure 8.16: Occurrence of Backflow, Depending on $\varphi\eta_{tt}/\psi_{\text{tt}}$ and κ; CFD results and Strscheletzky criterion.

8.6 Conclusions

To achieve higher efficiency (η_{ts} and η_{tt}) of low-pressure axial fans with small HTR, the well-known vortex distribution design method is employed where the duty point is expressed by the flow coefficient φ and the total pressure coefficient ψ_{tt}. The application of this method to fans with small HTR involves specific challenges, as described in the Introduction.

Once the vortex distribution and the lift curve distribution for the selected airfoil blade sections have been selected, cascade analysis provides the stagger angle and chord length distributions. These in turn give the full geometry of the blade sections (up to a choice for the stacking line, taken as radial here).

Following the approach by [13], the vortex distribution $r v_{\theta 2}(r)$ and the hub-tip diameter ratio κ are selected such that the maximum $\eta_{\text{ts.max}}$ is obtained. This is accomplished by solving a constrained nonlinear multi-variable problem, where

κ and the coefficients in the adopted polynomial expression Eq. (8.12) for the vortex distribution form the degrees of freedom.

For a free-vortex distribution, an analytic solution is given (for the first time) for the optimal κ_{opt} and the expected achievable $\eta_{ts.idmax}$ as function of (φ, ψ_{tt}). Surprisingly, this optimal κ_{opt} is equal to that according to the Strscheletzky backflow criterion.

For polynomial vortex distributions, linear, quadratic and cubic types have been investigated. Compared with the free vortex case, the increased number of degrees of freedom results in higher $\eta_{ts.max}$ and decreased κ_{opt}. This means that for the polynomial vortex distribution designs backflow may be expected (from the Strscheletzky backflow criterion developed for free-vortex distributions).

The prescribed lift coefficient distribution of the airfoil blade sections is carefully selected such that the prescribed lift coefficient equals its maximum at the heavily loaded hub, while the lift coefficient prescribed at the tip is lower for better anti-stall characteristics.

For the fans thus obtained through the vortex distribution design method, CFD simulations have been performed (using a validated CFD simulation method for low-pressure axial fans with small HTR [50]) to investigate the aerodynamic performance of the fan blades designed by the current approach.

The CFD predictions show that all optimal designed vortex distributions satisfy the design duty (pressure coefficient ψ and total pressure coefficient ψ_{tt}), with significantly improved efficiencies η_{ts} and η_{tt}.

For the free vortex design, increased ψ and ψ_{tt} with improved efficiency η_{ts} and η_{tt} are obtained for all flow coefficients φ. However, for the linear, quadratic and cubic vortex distributions, reduced ψ and ψ_{tt} are found at low φ; at the design duty point and higher φ, higher or almost the same ψ and ψ_{tt} are obtained (in comparison to the baseline case). For $\eta_{ts.max}$, the free and linear vortex distribution designs give higher predictions than the quadratic and cubic vortex distribution designs. This can be explained by the lower HTR κ and consequent backflow region near the design duty point. For $\eta_{tt.max}$, a larger number of degrees freedoms in the vortex distribution gives higher efficiency. The $\eta_{tt.max}$ values of free and polynomial vortex distribution designs differ less than 1%.

Flow field investigations have shown that backflow is present for the quadratic and cubic vortex distribution designs for both low and medium flow coefficient φ around 0.10 and 0.15, but for linear vortex design, the backflow is only found at low φ (near 0.10). For all polynomial vortex designs, the backflow together with the low stagger angles result in unexpected flow separations near the suction side of blade sections near the hub, which leads to the drop in the ψ and ψ_{tt} at low φ. The CFD results indicate that the Strscheletzky criterion works well as a conservative preliminary estimate for the presence of backflow, even for non-free vortex distributions.

Although the vortex distribution design method is based on an (over)simplified two-dimensional description of the three-dimensional flow fields obtained from the CFD simulations, it contains sufficient aspects of the essential physics, since the CFD predictions show that the current vortex distribution design method provides designs that meet the specified design duty (required pressure rise at specified flow), and, importantly, increased efficiencies η_{ts} and η_{tt}.

For future studies, it is recommended to: (i) perform measurements of axial fan designs obtained with the reported approach to further validate the design method (besides the CFD validations considered here), (ii) perform designs for axial fans with different design duty points to investigate the generality of the current approach for axial fan design, (iii) apply cascade airfoil data (for example, data from MISES [22, 23] rather than isolated airfoil data from XFOIL) in the design approach to better account for blade interference effects near the hub region, (iv) consider other airfoil profiles, such as circular-arc profiles rather than the Wortmann profiles considered here (although according to [38] (p.142) the influence of blade shape is small at low Mach numbers), (v) combine the current (solely) aerodynamic design method with mechanical/structural and production design considerations, (vi) Investigate the effects of blade skew with current optimal designs on the aerodynamic performance of axial fans with small HTR and (vii) develop backflow criteria for polynomial vortex distributions that extend the Strscheletzky backflow criterion that has been developed for free-vortex designs.

Appendix A: Strscheletzky Backflow Criterion

The HTR κ not only determines the radius of the hub with known parameters of the casing (determined by the specific applied configuration), but also has significant influence on the flow field patterns. The well-known Strscheletzky criterion of backflow (or hub dead space) [8, 149] plays an important role in determining (for a specific hub diameter) whether backflow may happen downstream of the rotor, with associated increased secondary flow losses.

For free-vortex distributions, Strscheletzky [8, 149, 150] formulated a criterion for the critical HTR κ_{crit} for the backflow region for axisymmetric flows, based on a principle of least action, resulting in the minimisation with respect to R_{hub} of the integral J for his “axially unlimited" case

$$J = \frac{1}{\pi\left(R_{fan}^2 - R_{hub}^2\right)} \int_{R_{hub}}^{R_{fan}} \left(\frac{1}{2}\rho v_2^2\right) 2\pi r dr. \tag{8.13}$$

Here the free-vortex velocity components $v_{x2}(r)$ and $v_{\theta 2}(r)$ are determined by the flow rate and ideal total-pressure rise, respectively. After some algebra, it follows

that the solution of the equation $\frac{\partial J}{\partial R_{\text{hub}}} = 0$ corresponds to Eq. (8.11). This equation is given in [11] with minor typos.

Appendix B: Solution of Radial Equilibrium Equation

In this Appendix aspects are discussed of Eqs. (8.3) and (8.4) from which $v_{x2}(r)$, the axial velocity distribution downstream of the fan blades, can be determined. These aspects deal with: (i) the numerical solution of Eq. (8.3) for $v_{x2}(r)$ and (ii) a condition for the flow rate Q for which a solution exists. When an optimisation method is used in conjunction with the vortex distribution design method, these aspects are important for a robust numerical solution process for Eqs. (8.3) and (8.4).

For a concise notation, the vortex distribution is denoted here by S, so $S(r) \equiv r\,v_{\theta 2}(r)$. In terms of S, Eq. (8.3) can be rewritten as

$$\frac{d}{dr}\left(\frac{1}{2}v_{x2}^2\right) = \eta_h \Omega \frac{dS}{dr} - \frac{1}{r^2}\frac{d}{dr}\left(\frac{1}{2}S^2\right). \tag{8.14}$$

Integration of this equation from R_{hub} to r, and employing partial integration of the last term on the right-hand side, gives

$$\frac{1}{2}v_{x2}^2(r) - \frac{1}{2}v_{x2.\text{hub}}^2 = \eta_h \Omega\,[S(r) - S_{\text{hub}}] - \frac{1}{2}\left[\frac{S^2(r)}{r^2} - \frac{S_{\text{hub}}^2}{R_{\text{hub}}^2}\right] - \int_{R_{\text{hub}}}^{r} \frac{S^2(r')}{r'^3}\,dr' \equiv H(r). \tag{8.15}$$

Here $v_{x2.\text{hub}}$ is the downstream axial velocity at the hub and S_{hub} is the vortex distribution at the hub. This form of Eq. (8.3) is advantageous for numerical solution methods, since it gives the axial velocity distribution $v_{x2}(r)$ in terms of the vortex distribution $r\,v_{\theta 2}$, without requiring its derivatives with respect to r. Eq. (8.15) can be written as

$$v_{x2}(r) = \sqrt{v_{x2.\text{hub}}^2 + 2H(r)}. \tag{8.16}$$

Here $v_{x2.\text{hub}}$ must be determined such that the distribution of the axial velocity $v_{x2}(r)$ is consistent with the prescribed flow rate Q, i.e. the following equation must be satisfied

$$Q = \int_{R_{\text{hub}}}^{R_{\text{fan}}} 2\pi r \sqrt{v_{x2.\text{hub}}^2 + 2H(r)}\,dr. \tag{8.17}$$

The smallest real value of $v_{x2.\text{hub}}$ is given by $v_{x2.\text{hub.min}}^2 = \min(0, -2H_{\text{min}})$. Hence, the smallest flow rate Q_{min} for which a solution for $v_{x2}(r)$ exists (for a specified

vortex distribution) is given by

$$Q_{\min} = \int_{R_{\text{hub}}}^{R_{\text{fan}}} 2\pi r \sqrt{\min(0, -2H_{\min}) + 2H(r)}\, dr\,. \tag{8.18}$$

Thus, a solution of Eqs. (8.3) and (8.17) for $v_{x2}(r)$ only exists when $Q \geq Q_{\min}$. Note that this minimum flow rate $Q_{\min}$ depends on the vortex distribution $S(r)$ through the function $H(r)$ (defined in Eq. (8.15)). For a free-vortex distribution, a solution always exists, and hence then the minimum flow rate $Q_{\min} = 0$. When a solution exists, Eq. (8.17) can be numerically solved for $v^2_{x2.\text{hub}}$ with a standard root-finding procedure.

Chapter 9

Conclusions and Recommendations

9.1 Conclusions

Low-pressure axial fans are widely used in many industrial and domestic applications, especially for cooling and ventilation purposes. Such fans have already experienced a long-term development with the design principles, fundamental theories and optimization methods being reported quite a lot in detail. However, the attention of most literature has been limited to fans with medium to large hub-to-tip diameter ratio (*HTR* in short). For fans with a small *HTR*, the investigations about the CFD simulation strategy, aerodynamic performance optimizations and optimal design methods (for higher efficiency) are rarely reported.

In this thesis, the Computational Fluid Dynamics (CFD in short) simulation strategy for axial fans with small *HTR* is firstly investigated with focuses on a RANS CFD simulation strategy. Then sweep, dihedral and skew, as representative three-dimensional stacking methods, are investigated for their effects on the aerodynamic performance of axial fans with small *HTR*. The final optimization, with respect to total-to-static efficiency, is achieved by investigating the optimal vortex distributions and *HTR*s for the baseline fan configuration and operation duty point.

Computational Fluid Dynamics Simulation Strategy

Firstly, reliable measurements of the aerodynamic performance and the complete geometrical description of the baseline Howden fan with small *HTR* have been used to perform CFD simulations and analysis in order to investigate the influence of a number of parameters, ultimately aimed at formulating a strategy and guidelines for obtaining accurate CFD predictions of the aerodynamic performance (pressure coefficient ψ *and* total-to-static efficiency η_{ts}) for such machines.

The trailing edge shape (sharp vs. rounded) has a large influence on the predicted aerodynamic performance. The actual trailing edge geometry (rounded in this case) should be used in the CFD simulations for improved agreement with the experimental aerodynamic performance. The non-airfoil sections near the root have a minor influence on the pressure coefficient and hence on the total-to-static efficiency, due the formation of a vortex upstream from the blades near the hub. Overall, the “main blade" part well represents the aerodynamic performance. With increasing tip gap ratio, the pressure coefficient and the total-to-static efficiency decrease. The CFD simulations with the actual tip gap ratio present in the experiments do not adequately predict the influence of the tip gap on the aerodynamic performance. For use of CFD simulations within an industrial context, it is recommended not to take the tip gap into account, as then quantitatively good agreement is obtained between CFD predictions and experiments. For the turbulence model, the SST model significantly underpredicts the aerodynamic performance in comparison to the experiments, while those using the Spalart-Allmaras model yield much better agreement. Therefore, the use of the SA turbulence model is recommended for CFD simulations of axial fans with small hub-to-tip ratio.

Effects of Sweep, Dihedral and Skew on Aerodynamic Performance

Secondly, by using the validated CFD simulation method, simulations have been performed to investigate effects of (forward as well as backward) sweep, dihedral and skew on the aerodynamic performance of low pressure axial fans with small *HTR*, where the linear stacking line is employed.

In contrast to the flow patterns in medium to high *HTR* fans where radial migration occupies most of the suction side surface, the radial flow in the current study is more limited due to the chord of the blade sections being relatively smaller. The beneficial aerodynamic effects of skew (in the general sense) of the blades are therefore more limited here. In general, backward skew gives negative effects, while forward skew can (conditionally) give positive effects. Blades with sweep hardly lead to improvements in pressure coefficient and total-to-static efficiency. Only at large flow coefficient does forward sweep result in higher total-to-total efficiency. Forward dihedral gives some improvement in total-to-static and total-to-total efficiency near *BEP* and for large flow coefficient, but 25° forward dihedral and all blades with backward dihedral result in negative effects. Circumferential skew gives a performance similar to that with sweep, in both forward and backward direction, with higher total-to-total efficiency.

The similar performance in sweep and circumferential skew, as well as with

dihedral and axial skew, originate from the small stagger angle $\chi = 15°$. The benefits and disadvantages of sweep and dihedral can be traced to circumferential and axial skew. With different stagger angles, the proportion of circumferential and axial skew in sweep and dihedral is changed, and the consequent performance may also be changed.

Differently from wing aerodynamics where lift coefficients are reduced by factors $\cos\gamma$ and $\cos^2\gamma$ for sweep and dihedral respectively, the reduction of the pressure coefficients is much more limited (pressure rise is larger than expected). This is considered to be the result of the (much more) complex three-dimensional flow patterns in axial fans, involving backflow and hub corner stall that are absent in flows around wings. The highest η_{ts} is predicted for axial skew; only 5° forward axial skew gives positive effects on both pressure coefficient and efficiency. Forward axial skew as well as forward dihedral influence the backflow region significantly, where a larger forward angle helps to suppress the backflow. Although the improvements from sweep, dihedral and skew on fan aerodynamic performance are limited for the considered baseline fan with small *HTR*, for different optimization purposes, different blade shifts can be applied. Forward sweep and forward circumferential skew with large angles can be used for higher η_{tt}, while forward dihedral and forward axial skew can suppress backflow and give positive effects on η_{ts}.

Optimal Vortex Distribution Design Method

Thirdly, a vortex distribution design method is employed for low-pressure axial fan with small *HTR* for achieving higher total-to-static and total-to-total efficiency η_{ts} and η_{tt}. Free and general vortex distributions are investigated.

The achievable η_{ts} is analysed as function of design duty point (φ, ψ_{tt}), hub-to-tip ratio κ and vortex distribution $r\,v_{\theta 2}(r)$. By applying a constrained nonlinear multivariable function method, optimal κ and $r\,v_{\theta 2}(r)$ are obtained. Analytic solutions for optimal κ and expected achievable η_{ts} as function of (φ, ψ_{tt}) are formulated (*for the first time*) for free vortex designs with constant $r\,v_{\theta 2}(r)$, which is surprisingly the same as the Strscheletzky backflow criterion. For general (linear, quadratic and cubic) vortex distributions , the increased number of degrees of freedom results in decreased optimal κ, which means backflow may be expected for general vortex distribution designs.

The CFD predictions show that designs with all vortex distribution types are able to satisfy (and even exceed) the design duty pressure coefficient ψ and total pressure coefficient ψ_{tt} with significantly improved η_{ts} and η_{tt}. For the free vortex design, higher ψ and ψ_{tt} with improved efficiency η_{ts} and η_{tt} are found for all flow coefficients φ. However, for linear, quadratic and cubic vortex distributions, lower ψ and ψ_{tt} are found in low φ; at design duty point and for higher

φ, compared with the baseline case, higher or almost same ψ and ψ_{tt} are found. Different distribution freedoms give close predictions in $\eta_{ts,max}$ and $\eta_{tt,max}$. Flow field investigations show that backflow is present for quadratic and cubic vortex designs near the design duty and for lower flow coefficients; for the linear vortex design, backflow is only present at low φ. Differently from the baseline case, the backflow together with the low stagger angle near the hub result in unexpected flow separations near the suction side of the blade section, which leads to the drop in ψ and ψ_{tt} near low φ.

Therefore, the current vortex distribution design method is able to find optimal design parameters with respect to the specific design duty; high η_{ts} and η_{tt} can be achieved with the required pressure rise.

9.2 Recommendations

With respect to the subjects of this thesis, there are some lines of research that could be continued, as described in following.

Measurements All investigations in this thesis are based on CFD simulations. Although the validated simulation strategy makes the results reliable, it is interesting how the aerodynamic performance would be in measurements for small *HTR* fan with skewed (in the general sense) blades and blades designed by the vortex distribution design method. It is also recommended to perform measurements of detailed flow fields (for example the velocity distributions, visualization of backflow, etc.) for further validation of the current simulation strategy and results. This will provide better understanding of the aerodynamic performance of low-pressure axial fan with small *HTR*.

CFD Simulation For RANS CFD simulations, the effects of the shape of the computational domain on the predicted performance are not investigated in great detail in this thesis. With respect to the shape of test facility, the calculation domain downstream of the rotor may be substituted by cylindrical or spherical shape with larger radius ($> 4R_{fan}$). An example of such an investigation has been reported by Masi and Lazzaretto [76]. Also, the actual hub shape downstream of the fan (bulb-shaped; not extended to the outlet) present in the experiments may be accounted for in the simulation. The *SST* turbulence model underpredicts the aerodynamic performance in this thesis, with large extent of the backflow region, compared to that with the *SA* turbulence model. However, as reported in Chapter 3, the *SST* model has been applied successfully in simulations of axial fans. Therefore, it is interesting to investigate the effects of the combination of calculation domain and turbulence model on the predicted aerodynamic performance.

Another simplification is the absent tip gap. With tip gap present in the calculation domain, significant drops of RANS CFD predictions are found (as reported

in Chapter 6) which result in large deviations between CFD predictions and measurements of the baseline small HTR fan. The flow field investigations show that extensive vortices are present in tip leakage flow. However, the tip gap is present in the measurements, which means the effects of tip gap on the aerodynamic performance are not predicted adequately by the current RANS CFD strategy. Therefore, it is interesting to employ *LES* or *NLEVM* in the simulations of low-pressure axial fans with small *HTR* to investigate a (potentially) better simulation strategy with tip gap being studied in (much) more detail.

Blade Skew CFD simulations for other small *HTR* axial fans with sweep, skew and dihedral would help to consolidate the results in this thesis. The small stagger angle (with respect to the circumferential direction) of baseline fan in this thesis makes the aerodynamic performance of sweep and circumferential skew (or dihedral and axial skew) similar to each other. So it is recommended to investigate the effects on the aerodynamic performance of skew (in the general sense) together with different stagger angles.

The linear stacking line is employed in this thesis and the effects of sweep, dihedral and skew on the aerodynamic performance are found to be less significant. It is interesting to investigate skewed blades with a non-linear stacking line and the combination of sweep, skew and dihedral in a single blade with respect to their advantages. For example, dihedral or axial skew could be applied near the hub for decreasing the backflow region; sweep or circumferential skew could be applied near the tip for shortening the radial migration path. More detailed descriptions and an overview of their benefits are given in Ref. [84].

Vortex Distribution Design Method Two main simplifications in the vortex distribution design method reported in Chapter 8 are: (i) No correction is considered with respect to the cascade blade interference effect near the hub, (ii) A linear distribution of the lift coefficient is employed from hub to tip.

For axial fans with small *HTR*, the solidity at the hub may easily be larger than one. For a more accurate design method, it is recommended to consider the correction of the lift coefficient near the hub due to interference effects by applying correction factors like Weinig's coefficient [139] or cascade airfoil data (for example data from MISES [22, 23] or measured cascade data).

For the lift coefficient distribution $C_l(r)$, the linear distribution is applied in this thesis. Different $C_l(r)$ will give different distributions of chord length and stagger angle, eventually resulting in various blade shapes. Although the inflow and outflow velocities are the same under two-dimensional design assumption, different blade shapes are not likely to have the same aerodynamic performances in three-dimensional flow. Therefore, it is interesting to investigate the effects of $C_l(r)$ distributions on the aerodynamic performance of low-pressure axial fans with small HTR based on the known optimal $r v_{\theta 2}(r)$ through a parametric study and CFD simulations.

In this thesis, the lift coefficient near the tip is considered to be conservative for better anti-stall characteristic. A phenomenon named “stall delay" has been reported in wind turbine research [153], where the maximum lift coefficient of blade sections in three-dimensional flow is significantly increased compared to the corresponding two-dimensional case. Therefore, the occurrence of flow separation is delayed to a higher angle of attack. The master theses of Ling Zheng [154] and Vinith Mohan [155] reported a similar phenomenon in axial fans. However, it is still not clear how stall delay can be described for axial fans. It is interesting to further investigate this effect and apply it in the design of axial fans.

Backflow The backflow region, or the recirculation zone downstream of fan rotor, is the key characteristic of small *HTR* axial fans. The appearance of backflow could be related to an observation called “vortex breakdown" where a recirculation zone is generated at a sufficient degree of swirl [156]. Such observations are found from laminar flow to turbulent flow (Reynolds number ranging from less than 1000 to greater than 10^5). It is interesting to investigate the effects of backflow on the aerodynamic performance of axial fans together with the ideas from vortex breakdown studies.

The Strscheletzky backflow criterion (Eq. (8.11)) is based on free vortex considerations. Following the main idea of Strscheletzky’s formulation (Eq. (8.13)), it is possible and recommended to obtain a backflow criterion of general vortex distribution for understanding of the aerodynamic performance of axial with small HTR.

Aeroacoustics Although not studied and reported in this thesis, the aeroacoustic performance of axial fans is of high importance and has attracted the attention of many researchers. One of the main advantages of blade sweep is the reduced noise. Hence, it is recommended to take aeroacoustic evaluations into account in further study of the vortex distribution design method.

Mechanical/Structural Consideration In this thesis, only the aerodynamic performance is considered. For further steps of axial fan designs, the mechanical/structural and production design considerations should be involved. With these considerations, the large twists of blade may not be desirable. Therefore, the combination of the current (solely) aerodynamic design method with mechanical/structural considerations is recommended.

Bibliography

[1] Axair Newsletter, *Forward curved centrifugal fans - single inlet - external rotor motor*, Website, https://www.axair-fans.co.uk/industrial-fans/centrifugal-fans/forward-curved-centrifugal-fans-single-inlet-external-rotor-motor/, 2019.

[2] AC MAROC Tanger, *Extracteurs hélicoïdes*, Website, https://www.facebook.com/pg/ACmaroctanger/photos/?tab=album&album_id=757086117773671/, 2019.

[3] Pinterest, *Free fan example*, Website, https://id.pinterest.com/pin/704743-041682976183/, 2019.

[4] NGS, *Industrial cooling fans – howden*, Website, http://ngs-hab.ru/ENG/hw_cooling.php, 2019.

[5] European Commission (2009), "Directive 2009/125/EC of the European parliament and of the council of 21 October 2009", *Official Journal of the European Union*, vol. L285, pp. 10–35,

[6] European Commission (2011), "Commission regulation (EU) No. 327/2011", *Official Journal of the European Union*, vol. L90, pp. 8–21,

[7] Howden, *Howden industrial cooling fans*, Website, https://www.howden.com/en-gb/products/fans/cooling-fan, 2021.

[8] B Eck, *Fans: design and operation of centrifugal, axial-flow, and cross-flow fans*. Pergamon Press, 1973.

[9] S. Dixon and C. Hall, *Fluid mechanics and thermodynamics of turbomachinery*. Butterworth-Heinemann, 2014.

[10] O Cordier, "Ähnlichkeitsbedingungen für Strömungsmaschinen", *BWK Bd*, vol. 6, no. 10, 1953.

[11] S Castegnaro, "Aerodynamic design of low-speed axial-flow fans: A historical overview", *Designs*, vol. 2, no. 3, p. 20, 2018, ISSN: 2411-9660.

[12] G. Csanady, *Theory of Turbomachines*. McGraw-Hill, 1964.

[13] K Bamberger and T Carolus, "Achievable total-to-static efficiencies of low-pressure axial fans", in *Proceedings of the Fan 2015 Conference*, 2015.

[14] P. Pelz and M Metzler, "Optimization of power-specific investment costs for small hydropower", in *17th International Seminar on Hydropower Plants, Vienna, Austria, Nov*, 2012, pp. 21–23.

[15] H Marcinowski, "Optimalprobleme bei axialventilatoren", PhD thesis, Technischen Hochsehule, Berlin, Germany, 1956.

[16] H Glauert, *The elements of aerofoil and airscrew theory*. Cambridge University Press, 1983.

[17] V Bertram, *Practical ship hydrodynamics*. Elsevier, 2012.

[18] W. Durand, *Aerodynamic Theory: A General Review of Progress Under a Grant of the Guggenheim Fund for the Promotion of Aeronautics*. Springer Verlag, 2013.

[19] M Drela, "Xfoil: An analysis and design system for low Reynolds number airfoils", in *Low Reynolds number aerodynamics*, Springer, 1989, pp. 1–12.

[20] R. Turner, *Notes on ducted fan design*. Ministry of Aviation, Aeronautical Research Council, 1964.

[21] R. Wallis, *Axial Flow Fans: Design and Practice*. Academic Press, 1961.

[22] H Youngren and M Drela, "Viscous/inviscid method for preliminary design of transonic cascades", in *27th Joint Propulsion Conference*, 1991, p. 2364.

[23] M Drela and M. Giles, "Viscous-inviscid analysis of transonic and low reynolds number airfoils", *AIAA journal*, vol. 25, no. 10, pp. 1347–1355, 1987.

[24] J. Jung and W. Joo, "Effect of tip clearance, winglets, and shroud height on the tip leakage in axial flow fans", *International Journal of Refrigeration*, vol. 93, pp. 195–204, 2018.

[25] F Krömer, F Czwielong, and S Becker, "Experimental investigation of the sound emission of skewed axial fans with leading-edge serrations", *AIAA Journal*, vol. 57, no. 12, pp. 5182–5196, 2019.

[26] H. Lee, K. Lim, and H. Lee, "Reduction of ceiling fan noise by serrated trailing edge", *Fluctuation and noise letters*, vol. 17, no. 03, p. 1 850 026, 2018.

[27] T Carolus, *Ventilatoren: Aerodynamischer Entwurf, Schallvorhersage, Konstruktion (in German)*. Springer Verlag, 2003.

[28] A Busemann, "Aerodynamischer auftrieb bei überschallgeschwindigkeit", *Luftfahrtforschung*, vol. 12, no. 6, pp. 210–220, 1935.

[29] J. Anderson, *Introduction to Flight*. McGraw-Hill Education, 2016.

[30] yKirone, *Fixed-wing aircraft airplane swept wing variable-sweep wing*, Website, `https://imgbin.com/png/BUMNFZC1/fixed-wing-aircraft-airplane-swept-wing-variable-sweep-wing-png`, 2017.

[31] S. Gallimore, J. Bolger, N. Cumpsty, M. Taylor, P. Wright, and J. Place, "The use of sweep and dihedral in multistage axial flow compressor blading—Part I: University research and methods development", *Journal of Turbomachinery*, vol. 124, no. 4, pp. 521–532, 2002.

[32] ——, "The use of sweep and dihedral in multistage axial flow compressor blading—Part II: Low and high-speed designs and test verification", *Journal of Turbomachinery*, vol. 124, no. 4, pp. 533–541, 2002.

[33] M. Beiler and T. Carolus, "Computation and measurement of the flow in axial flow fans with skewed blades", *Journal of Turbomachinery*, vol. 121, no. 1, pp. 59–66, 1999, ISSN: 0889-504X.

[34] J Hurault, S Kouidri, F Bakir, and R Rey, "Experimental and numerical study of the sweep effect on three-dimensional flow downstream of axial flow fans", *Flow Measurement and Instrumentation*, vol. 21, no. 2, pp. 155–165, 2010.

[35] A Corsini and F Rispoli, "Using sweep to extend the stall-free operational range in axial fan rotors", *Proceedings of the Institution of Mechanical Engineers, Part A: Journal of Power and Energy*, vol. 218, no. 3, pp. 129–139, 2004.

[36] J Vad, A. Kwedikha, and H Jaberg, "Effects of blade sweep on the performance characteristics of axial flow turbomachinery rotors", *Proceedings of the Institution of Mechanical Engineers, Part A: Journal of Power and Energy*, vol. 220, no. 7, pp. 737–749, 2006.

[37] C. Jang, A Samad, and K. Kim, "Optimal design of swept, leaned and skewed blades in a transonic axial compressor", in *Turbo Expo: Power for Land, Sea, and Air*, vol. 4241, 2006, pp. 1279–1288, ISBN: 079184241X.

[38] N. Cumpsty, *Compressor Aerodynamics*. Longman, 1989.

[39] Howden Netherlands, *Aerodynamic performance testing of howden cooling fans according AMCA210 - ISO 5801*, 2017.

[40] D Thévenin and G Janiga, *Optimization and Computational Fluid Dynamics*. Springer Science and Business Media, 2008.

[41] D Borello, A Corsini, G Delibra, M Fiorito, and A. Sheard, "Large-eddy simulation of a tunnel ventilation fan", *Journal of Fluids Engineering*, vol. 135, p. 071 102, 2013.

[42] S. M. A. Moghadam, M Meinke, and W Schroder, "Analysis of tip-leakage flow in an axial fan at varying tip-gap sizes and operating conditions", *Computers and Fluids*, vol. 183, pp. 107–120, 2019.

[43] S. Pope, *Turbulent Flows*. Cambridge University Press, 2000.

[44] P Bradshaw, "Turbulence modeling with application to turbomachinery", *Progress in Aerospace Sciences*, vol. 32, pp. 575–624, 1996.

[45] P. Tucker, "Trends in turbomachinery turbulence treatments", *Progress in Aerospace Sciences*, vol. 63, pp. 1–32, 2013.

[46] A Corsini, G Delibra, and A. Sheard, "A critical review of computational methods and their application in industrial fan design", *International Scholarly Research Notices*, vol. 2013, 2013.

[47] U.S. Department of Energy, "Energy conservation standards rulemaking framework for commercial and industrial fans and blowers", *U.S. Department of Energy*, 2013.

[48] P Spalart and S Allmaras, "A one-equation turbulence model for aerodynamic flows", *La Recherche Aérospatiale*, vol. 1, pp. 5–21, 1994.

[49] G. Jin, H Ouyang, Y. Wu, and Z. Du, "Experimental and numerical investigations of the tip leakage flow of axial fans with circumferential skewed blades under off-design conditions", *Proceedings of the Institution of Mechanical Engineers, Part C: Journal of Mechanical Engineering Science*, vol. 224, no. 6, pp. 1203–1216, 2010.

[50] J Wang and N. Kruyt, "CFD simulations of aerodynamic performance of low-pressure axial fans with small hub-to-tip diameter ratio", *Journal of Fluids Engineering*, 2020, ISSN: 0098-2202.

[51] G Rabai and J Vad, "Validation of a computational fluid dynamics method to be applied to linear cascades of twisted-swept blades", *Periodica Polytechnica Mechanical Engineering*, vol. 49, no. 2, pp. 163–180, 2005.

[52] W. Jones and B. Launder, "The prediction of laminarization with a two-equation model of turbulence", *International journal of heat and mass transfer*, vol. 15, no. 2, pp. 301–314, 1972.

[53] D. Wilcox, *Turbulence modeling for CFD*. Vol. 2. La Canada, CA: DCW industries, 1998.

[54] D. Wilcox, "Formulation of the $k-\omega$ turbulence model revisited", *AIAA journal*, vol. 46, no. 11, pp. 2823–2838, 2008.

[55] F Menter, "Zonal two equation $k-\omega$ turbulence models for aerodynamic flows", in *23rd fluid dynamics, plasmadynamics, and lasers conference*, 1993, p. 2906.

[56] F. Menter, "Two-equation eddy-viscosity turbulence models for engineering applications", *AIAA Journal*, vol. 32, pp. 1598–1605, 1994.

[57] J Vad, A. Kwedikha, C Horváth, M Balczó, M. Lohász, and T Régert, "Aerodynamic effects of forward blade skew in axial flow rotors of controlled vortex design", *Proceedings of the Institution of Mechanical Engineers, Part A: Journal of Power and Energy*, vol. 221, no. 7, pp. 1011–1023, 2007.

[58] J Vad, A Kwedikha, and C Horvath, "Combined effects of controlled vortex design and forward blade skew on the three-dimensional flow in axial flow rotors", in *Conference on Modelling Fluid Flow (CMFF'06)*, pp. 1139–1146.

[59] M. Wilkinson, S. van der Spuy, and T. von Backström, "Performance testing of an axial flow fan designed for air-cooled heat exchanger applications", *Journal of Engineering for Gas Turbines and Power*, vol. 141, p. 051 007, 2019.

[60] M Masi, M Piva, and A Lazzaretto, "Design guidelines to increase the performance of a rotor-only axial fan with constant-swirl blading", in *ASME Turbo Expo 2014: Turbine Technical Conference and Exposition*, vol. 1A, V01AT10A033.

[61] T Zhu and T. Carolus, "Experimental and numerical investigation of the tip clearance noise of an axial fan", in *ASME Turbo Expo 2013: Turbine Technical Conference and Exposition*, vol. 4, V004T10A001.

[62] T. Carolus, T Zhu, and M Sturm, "A low pressure axial fan for benchmarking prediction methods for aerodynamic performance and sound", *Noise Control Engineering Journal*, vol. 63, pp. 537–545, 2015.

[63] Numeca International, *Fine/turbo 12.2 theory guide*, 2018.

[64] T. Craft, B. Launder, and K Suga, "Development and application of a cubic eddy-viscosity model of turbulence", *International Journal of Heat and Fluid Flow*, vol. 17, no. 2, pp. 108–115, 1996.

[65] F. Menter, A. Garbaruk, and Y Egorov, "Explicit algebraic reynolds stress models for anisotropic wall-bounded flows", *Progress in flight physics*, vol. 3, pp. 89–104, 2012.

[66] W. Chen, F. Lien, and M. Leschziner, "Computational prediction of flow around highly loaded compressor-cascade blades with non-linear eddy-viscosity models", *International Journal of Heat and Fluid Flow*, vol. 19, no. 4, pp. 307–319, 1998.

[67] A Corsini and F Rispoli, "Flow analyses in a high-pressure axial ventilation fan with a non-linear eddy-viscosity closure", *International Journal of Heat and Fluid Flow*, vol. 26, no. 3, pp. 349–361, 2005.

[68] D Borello, K Hanjalic, and F Rispoli, "Prediction of cascade flows with innovative second-moment closures", *Journal of Fluids Engineering*, vol. 127, pp. 1059–1070, 2005.

[69] D Borello and K Hanjalic and F Rispoli, "Computation of tip-leakage flow in a linear compressor cascade with a second-moment turbulence closure", *International Journal of Heat and Fluid Flow*, vol. 28, no. 4, pp. 587–601, 2007.

[70] I. S. Organization, "Industrial fans - performance testing using standardized airways (iso 5801:2017)", 2017.

[71] C Sarraf, H Nouri, F Ravelet, and F Bakir, "Experimental study of blade thickness effects on the overall and local performances of a controlled vortex designed axial-flow fan", *Experimental Thermal and Fluid Science*, vol. 35, no. 4, pp. 684–693, 2011.

[72] L Chen, H Xie, J Xu, R Dai, and J Chen, "Experimental and numerical study on the performance of an axial fan with a Gurney flap", *Advances in Mechanical Engineering*, vol. 10, no. 10, pp. 1–17, 2018.

[73] S. Courty-Audren, A Ortolan, X Carbonneau, N Binder, and F Challas, "Numerical analysis of secondary flow topologies of low-speed axial fans from compressor to load-controlled windmill", in *12th European Conference on Turbomachinery Fluid dynamics and Thermodynamics (ETC12)*, Stockholm, SE, 2017, pp. 1–12.

[74] A Corsini and F Rispoli, "Flow analyses in a high-pressure axial ventilation fan with a non-linear eddy-viscosity closure", *International Journal of Heat and Fluid Flow*, vol. 26, no. 3, pp. 349–361, 2005.

[75] G Angelini, T Bonanni, A Corsini, G Delibra, L Tieghi, and D Volponi, "Optimization of an axial fan for air cooled condensers", *Energy Procedia*, vol. 126, pp. 754–761, 2017, ISSN: 1876-6102.

[76] M Masi and A Lazzaretto, "CFD models for the analysis of rotor-only industrial axial-flow fans", in *Fan2012 International Conference on Fan Noise, Technology and Numerical Methods*, 2012.

[77] G Dufour, N. G. Rosa, and S Duplaa, "Validation and flow structure analysis in a turbofan stage at windmill", *Proceedings of the Institution of Mechanical Engineers, Part A: Journal of Power and Energy*, vol. 229, no. 6, pp. 571–583, 2015.

[78] Numeca International, *FINE/Turbo 12.2 User Guide*, 2018.

[79] I. Celik, U Ghia, P. Roache, and C. Freitas, "Procedure for estimation and reporting of uncertainty due to discretization in CFD applications", *Journal of Fluids Engineering*, vol. 130, no. 7, Jul. 2008, ISSN: 0098-2202.

[80] T. Carolus, T Zhu, and M Sturm, "A low pressure axial fan for benchmarking prediction methods for aerodynamic performance and sound", in *Fan2015 International Conference on Fan Noise, Technology and Numerical Methods*, 2015.

[81] Z Li and X Zheng, "Review of design optimization methods for turbomachinery aerodynamics", *Progress in Aerospace Sciences*, vol. 93, pp. 1–23, 2017.

[82] W. Godwin, *Effect of sweep on performance of compressor blade sections as indicated by swept-blade rotor, unswept-blade rotor, and cascade tests*. NACA Technical Notes 4062, 1957.

[83] K. Mohammed and D. Raj, "Investigations on axial flow fan impellers with forward swept blades", *Journal of Fluids Engineering*, vol. 99, no. 3, pp. 543–547, 1977, ISSN: 0098-2202.

[84] J Vad, "Aerodynamic effects of blade sweep and skew in low-speed axial flow rotors at the design flow rate: An overview", *Proceedings of the Institution of Mechanical Engineers, Part A: Journal of Power and Energy*, vol. 222, no. 1, pp. 69–85, 2008.

[85] J Vad, "Forward blade sweep applied to low-speed axial fan rotors of controlled vortex design: An overview", *Journal of Engineering for Gas Turbines and Power*, vol. 135, no. 1, Nov. 2012, ISSN: 0742-4795.

[86] S. Seo, S. Choi, and K. Kim, "Design optimization of a low-speed fan blade with sweep and lean", *Proceedings of the Institution of Mechanical Engineers, Part A: Journal of Power and Energy*, vol. 222, no. 1, pp. 87–92, 2008.

[87] J Vad, A. Kwedikha, and H Jaberg, "Influence of blade sweep on the energetic behavior of axial flow turbomachinery rotors at design flow rate", in *Turbo Expo: Power for Land, Sea, and Air*, vol. 41707, 2004, pp. 447–456.

[88] J. Denton and L Xu, "The exploitation of three-dimensional flow in turbomachinery design", *Proceedings of the Institution of Mechanical Engineers, Part C: Journal of Mechanical Engineering Science*, vol. 213, no. 2, pp. 125–137, 1998.

[89] M Masi and A Lazzaretto, "A simplified theory to justify forward sweep in low hub-to-tip ratio axial fan", in *Proceedings of the ASME Turbo Expo*, vol. 1, 2015.

[90] A. Wadia, P. Szucs, and D. Crall, "Inner workings of aerodynamic sweep", *Journal of Turbomachinery*, vol. 120, no. 4, pp. 671–682, 1998.

[91] P. Ramakrishna and M Govardhan, "Combined effects of forward sweep and tip clearance on the performance of axial flow compressor stage", in *Turbo Expo: Power for Land, Sea, and Air*, vol. 48883, 2009, pp. 273–282, ISBN: 0791848884.

[92] N Yamaguchi, "Performance improvement by forward-skewed blading of axial fan moving blades", *ISABE*, vol. 93, no. 7055, pp. 580–589, 1993.

[93] J Wang and N. Kruyt, "Effects of sweep, dihedral and skew on aerodynamic performance of low-pressure axial fans with small hub-to-tip diameter ratio", *Journal of Fluids Engineering*, 2021, ISSN: 0098-2202.

[94] T Sasaki and F Breugelmans, "Comparison of sweep and dihedral effects on compressor cascade performance", *Journal of Turbomachinery*, vol. 120, no. 3, pp. 454–463, 1998, ISSN: 0889-504X.

[95] F. Breugelmans, Y Carels, and M Demuth, "Influence of dihedral on the secondary flow in a two-dimensional compressor cascade", *Journal of Engineering for Gas Turbines and Power*, vol. 106, no. 3, pp. 578–584, 1984, ISSN: 0742-4795.

[96] A. N. İlikan and E Ayder, "Influence of dihedral stacking on the performance of an axial fan", *Engineering Applications of Computational Fluid Mechanics*, vol. 8, no. 4, pp. 518–529, 2014, ISSN: 1994-2060.

[97] C Clemen, V Gümmer, M Goller, H Rohkamm, U Stark, and H Saathoff, "Tip-aerodynamics of forward-swept rotor blades in a highly-loaded single-stage axial-flow low-speed compressor", in *10th International Symposium on Transport phenomena and dynamics of rotating machinery (ISROMAC10), Honolulu*, 2004.

[98] K Bamberger and T Carolus, "Aerodynamic optimization of axial fans using the adjoint method", in *Turbo Expo: Power for Land, Sea, and Air*, vol. 50985, 2018, V001T09A014.

[99] J. Nelder and R Mead, "A simplex method for function minimization", *The computer journal*, vol. 7, no. 4, pp. 308–313, 1965.

[100] J Li, H Chen, Y Liu, J Wang, and X Yang, "Aerodynamic design and optimization of a high-loaded axial fan stage using a curvature control method", *Journal of Mechanical Science and Technology*, vol. 33, no. 8, pp. 3871–3883, 2019.

[101] J. Kim, J. Choi, A Husain, and K. Kim, "Performance enhancement of axial fan blade through multi-objective optimization techniques", *Journal of mechanical science and technology*, vol. 24, no. 10, pp. 2059–2066, 2010.

[102] C. Jang and K. Kim, "Optimization of a stator blade using response surface method in a single-stage transonic axial compressor", *Proceedings of the Institution of Mechanical Engineers, Part A: Journal of Power and Energy*, vol. 219, no. 8, pp. 595–603, 2005.

[103] B Chen and X Yuan, "Advanced aerodynamic optimization system for turbomachinery", *Journal of Turbomachinery*, vol. 130, no. 2, 2008, ISSN: 0889-504X.

[104] T. Carolus and R Starzmann, "An aerodynamic design methodology for low pressure axial fans with integrated airfoil polar prediction", in *ASME 2011 Turbo Expo: Turbine Technical Conference and Exposition*, vol. 4, pp. 335–342.

[105] B. Lin, C. Hung, and E. Tang, "An optimal design of axial-flow fan blades by the machining method and an artificial neural network", *Proceedings of the Institution of Mechanical Engineers, Part C: Journal of Mechanical Engineering Science*, vol. 216, no. 3, pp. 367–376, 2002.

[106] K Bamberger and T Carolus, "Performance prediction of axial fans by CFD-trained meta-models", in *ASME Turbo Expo: Power for Land, Sea, and Air*, vol. 45578, 2014, V01AT10A028.

[107] K Bamberger and T Carolus, "Design guidelines for low pressure axial fans based on CFD-trained meta-models", in *Proc. European Turbomachinery Conference*, vol. 11, 2015.

[108] X Tang, J Luo, and F Liu, "Adjoint aerodynamic optimization of a transonic fan rotor blade with a localized two-level mesh deformation method", *Aerospace Science and Technology*, vol. 72, pp. 267–277, 2018.

[109] N. Kruyt and R. Westra, "On the inverse problem of blade design for centrifugal pumps and fans", *Inverse problems*, vol. 30, no. 6, p. 065 003, 2014.

[110] H Liu and B Jiang and W Wang and X Yang and J Wang, "Redesign of axial fan using viscous inverse design method based on boundary vorticity flux diagnosis", *Journal of Turbomachinery*, vol. 143, no. 5, p. 051 006, 2021.

[111] G Peng, S Cao, M Ishizuka, and S Hayama, "Design optimization of axial flow hydraulic turbine runner: Part I—an improved q3d inverse method", *International journal for numerical methods in fluids*, vol. 39, no. 6, pp. 517–531, 2002.

[112] G Peng and S Cao and M Ishizuka and S Hayama, "Design optimization of axial flow hydraulic turbine runner: Part II—multi-objective constrained optimization method", *International journal for numerical methods in fluids*, vol. 39, no. 6, pp. 533–548, 2002.

[113] R. Westra, "Inverse-design and optimization methods for centrifugal pump impellers", PhD thesis, University of Twente, Enschede, The Netherlands, 2008.

[114] W.R. Hawthorne and C Wang and C.S Tan and J.E. McCune, "Theory of blade design for large deflections: Part I—Two-dimensional cascade", *Journal of Engineering for Gas Turbines and Power*, vol. 106, no. 2, pp. 346–353, Apr. 1984, ISSN: 0742-4795.

[115] C. Tan, W. Hawthorne, J. McCune, and C Wang, "Theory of Blade Design for Large Deflections: Part II—Annular Cascades", *Journal of Engineering for Gas Turbines and Power*, vol. 106, no. 2, pp. 354–365, Apr. 1984, ISSN: 0742-4795.

[116] M Zangeneh, "A compressible three-dimensional design method for radial and mixed flow turbomachinery blades", *International Journal for Numerical Methods in Fluids*, vol. 13, no. 5, pp. 599–624, 1991.

[117] M Zangeneh, "Inverse Design of Centrifugal Compressor Vaned Diffusers in Inlet Shear Flows", *Journal of Turbomachinery*, vol. 118, no. 2, pp. 385–393, Apr. 1996.

[118] M Zangeneh, A Goto, and T Takemura, "Suppression of secondary flows in a mixed-flow pump impeller by application of three-dimensional inverse design method: Part 1-design and numerical validation", *Journal of Turbomachinery*, vol. 118, no. 3, pp. 536–543, 1996.

[119] M Zangeneh, M Schleer, F Pløger, S. Hong, C Roduner, B Ribi, and R. Abhari, "Investigation of an inversely designed centrifugal compressor stage—part I: Design and numerical verification", *Journal of Turbomachinery*, vol. 126, no. 1, pp. 73–81, 2004.

[120] G. Patterson, *Ducted fans: design for high efficiency*. Australian Council for Aeronautics, 1944.

[121] R. Downie, M.C.Thompson, and R. Wallis, "An engineering approach to blade designs for low to medium pressure rise rotor-only axial fans", *Experimental thermal and fluid science*, vol. 6, no. 4, pp. 376–401, 1993.

[122] J Vad, "Incorporation of forward blade sweep in preliminary controlled vortex design of axial flow rotors", *Proceedings of the Institution of Mechanical Engineers, Part A: Journal of Power and Energy*, vol. 226, no. 4, pp. 462–478, 2012.

[123] M Masi and A Lazzaretto, "A new practical approach to the design of industrial axial fans: Tube-axial fans with very low hub-to-tip ratio", *Journal of Engineering for Gas Turbines and Power*, vol. 141, GTP–19–1340, 2019.

[124] M Masi, S Castegnaro, and A Lazzaretto, "A criterion for the preliminary design of high-efficiency tube-axial fans", in *ASME Turbo Expo: Power for Land, Sea, and Air*, vol. 49682, 2016, V001T09A006.

[125] S Castegnaro, M Masi, and A Lazzaretto, "Preliminary experimental assessment of the performance of rotor-only axial fans designed with different vortex criteria", in *12 th European Conference on Turbomachinery Fluid dynamics and Thermodynamics*, ISBN: 2410-4833.

[126] L He and P Shan, "Three-dimensional aerodynamic optimization for axial-flow compressors based on the inverse design and the aerodynamic parameters", *Journal of Turbomachinery*, vol. 134, no. 3, 2012.

[127] D Bonaiuti and M Zangeneh, "On the coupling of inverse design and optimization techniques for the multiobjective, multipoint design of turbomachinery blades", *Journal of Turbomachinery*, vol. 131, no. 2, 2009.

[128] N. Kruyt, P. Pennings, and R Faasen, "Optimisation of efficiency of axial fans", in *12th European Fluid Machienry Congress: Proceedings 12th European Fluid Machinery Congress*, Woodhead Publishing, 2014, pp. 13–20.

[129] Airfoil Tools, *Wortmann airfoil*, `http://airfoiltools.com`, Web Page, Accessed July 8, 2019, 2019.

[130] W. Hughes, J. Brighton, and N Winowich, *Schaum's outline of fluid dynamics*. McGraw Hill Professional, 1999.

[131] R. Bilger, "A note on favre averaging in variable density flows", *Combustion Science and Technology*, vol. 11, no. 5-6, pp. 215–217, 1975.

[132] J. Ferziger, M Perić, and R. Street, *Computational methods for fluid dynamics*. Springer, 2002, vol. 3.

[133] Y. Choi and C. Merkle, "The application of preconditioning in viscous flows", *Journal of Computational Physics*, vol. 105, no. 2, pp. 207–223, 1993, ISSN: 0021-9991.

[134] Numeca International, *Igg 12.2 user guide*, 2018.

[135] T. Lindemann, J Friedrichs, and U Stark, "Development of a new design method for high efficiency swept low pressure axial fans with small hub/tip ratio", in *ASME Turbo Expo 2014: Turbine Technical Conference and Exposition*, vol. 1A, V01AT10A017.

[136] R van de Vondervoort, "Prediction of aerodynamic performance and noise production of axial fans", University of Twente, The Netherlands, M.Sc. Thesis, 2015.

[137] A Corsini, G Delibra, and A. Sheard, "The application of sinusoidal blade-leading edges in a fan-design methodology to improve stall resistance", *Proceedings of the Institution of Mechanical Engineers, Part A: Journal of Power and Energy*, vol. 228, pp. 255–271, 2013.

[138] J. Denton, "Loss mechanisms in turbomachines", *Journal of Turbomachinery*, vol. 115, no. 4, pp. 621–656, 1993, ISSN: 0889-504X.

[139] B Lakshminarayana, *Fluid Dynamics and Heat Transfer of Turbomachinery*. John Wiley & Sons, 1995.

[140] J. Adamczyk, M. Celestina, and E. Greitzer, "The role of tip clearance in high-speed fan stall", *Journal of Turbomachinery*, vol. 115, no. 1, pp. 28–38, 1993, ISSN: 0889-504X.

[141] M Inoue, M Kuroumaru, S Yoshida, T Minami, K Yamada, and M Furukawa, "Effect of tip clearance on stall evolution process in a low-speed axial compressor stage", in *ASME Turbo Expo 2004: Power for Land, Sea, and Air*, 2004.

[142] R. Jones and T Robert, "Effects of sweepback on boundary layer and separation", *NACA Technical Notes 1402*, 1947.

[143] B Maggin and R. Shanks, "The effect of geometric dihedral on the aerodynamic characteristics of a 40 deg swept-back wing of aspect ratio 3", NASA Langley Research Centre, Report, 1946.

[144] L. S. Jr and H Yeh, "Sweep and dihedral effects in axial-flow turbomachinery", *Journal of Fluids Engineering*, vol. 85, no. 3, pp. 401–414, 1963, ISSN: 0098-2202.

[145] K Bamberger and T Carolus, "Efficiency limits of fans", *Proceedings IMechE Part A: Journal of Power and Energy*, vol. 234, pp. 739–748, 2020.

[146] P Ruden, "Investigation of single stage axial fans", *NACA Technical Memorandum 1062*, 1944.

[147] D. Sörensen and J. Sörensen, "Toward improved rotor-only axial fans—part I: A numerically efficient aerodynamic model for arbitrary vortex flow", *Journal of Fluids Engineering*, vol. 122, no. 2, pp. 318–323, 2000.

[148] D. Sörensen, M. Thompson, and J. Sörensen, "Toward improved rotor-only axial fans—part II: Design optimization for maximum efficiency", *Journal of Fluids Engineering*, vol. 122, no. 2, pp. 324–329, 2000.

[149] M Strscheletzky, "Gleichgewichtsformen der rotationssymmetrischen Strömungen mit konstantem Drall in geraden, zylindrischen Rotationshohlräumen", *Voith Forschung und Konstruktion*, vol. 5, pp. 1–1, 1959.

[150] H Marcinowski, "Optimalprobleme bei Axialventilatoren (in German)", *Voith-Forschung und Konstruktion*, vol. 1, 1959.

[151] J. Horlock, *Axial Flow Turbines: Fluid Mechanics and Thermodynamics*. Krieger Publishing Company, 1966.

[152] R Storn and K Price, "Differential Evolution – a simple and efficient heuristic for global optimization over continuous spaces", *Journal of Global Optimization*, vol. 11, no. 4, pp. 341–359, 1997.

[153] D Hu, O Hua, and Z Du, "A study on stall-delay for horizontal axis wind turbine", *Renewable Energy*, vol. 31, no. 6, pp. 821–836, 2006.

[154] L Zheng, "Effects of 3d flow and rotation on aerodynamics of axial fans", University of Twente, The Netherlands, M.Sc. Thesis, 2019.

[155] V Mohan, "Stall delay for axial fans with medium hub-to-tip ratio", University of Twente, The Netherlands, M.Sc. Thesis, 2021.

[156] O Lucca-Negro and T O'doherty, "Vortex breakdown: A review", *Progress in energy and combustion science*, vol. 27, no. 4, pp. 431–481, 2001.

Publications

[1] Jie Wang, N.P. Kruyt. “Validation of CFD simulations of aerodynamic performance of low speed axial fans with low hub-to-tip ratio." In AIAA Scitech 2020 Forum 2020 (p. 0345).

[2] Jie Wang, N.P. Kruyt. (May 25, 2020). “Computational Fluid Dynamics Simulations of Aerodynamic Performance of Low-Pressure Axial Fans With Small Hub-to-Tip Diameter Ratio." ASME. J. Fluids Eng. September 2020; 142(9): 091202.

[3] Jie Wang, N.P. Kruyt. (July 28, 2021). “Effects of Sweep, Dihedral and Skew on Aerodynamic Performance of Low-Pressure Axial Fans With Small Hub-to-Tip Diameter Ratio." ASME. J. Fluids Eng. January 2022; 144(1): 011203.

[4] Jie Wang, N.P. Kruyt. “Design for High Efficiency of Low-pressure Axial Fans with Small Hub-to-tip Diameter Ratio by the Vortex Distribution Method." (Submitted to Journal of Fluids Engineering).

Acknowledgments

The start and end of this thesis witness my life in the Netherlands which begins from 12.Sept 2017. On that day, a flight took me from Beijing to Amsterdam, where I arrived at Schiphol Airport in the morning. At 8:44 am, a train stopped at the Enschede station, where I met Dr. Niels Kruyt for the first time and he wore a sweater with white and red stripes for the early autumn season. Four years passed by, it is time to express my gratitude to all the people who have supported, assisted and accompanied me through the PhD study.

First and foremost, I would like to express my greatest gratitude to my supervisor Niels Kruyt and my promotor Kees Venner for their continuous support and patience in every step of my study and growth.

It is hard to fully express my gratitude to you Niels, from the proposal stage of this project to now, you always inspire me to learn, practice and think more, to creatively study and apply and to establish connections between individual research topics. You are patient to my “stupid" questions and mistakes and open to all discussions. I feel that you are very much like Gandalf for a young hobbit who thirsts for knowledge, your rich knowledge and research experience have encouraged me to be self-motivated and optimistic in all the time. Beyond the scope of study, you are a very good friend with lots of wisdom, the best example should be “sit back for the whole picture" and “be patient with learning curve". These help me to have a balanced and enjoyable life.

It is my great pleasure to have Kees Venner as promotor in these years. I always remember my nervous feeling in the first talk with you, but you relaxed me a lot by very kind words. I am very grateful for your suggestions on my research and supports in many administrative tasks. I have learned a lot from your wealth of knowledge and management arts.

This thesis is a culmination of work at the Engineering Fluid Dynamics group of the University of Twente and Howden Netherlands. I would like to thank Sander Venema and Bastiaan Holm for your support in this long-term collaboration. I would be remiss not to mention the support of Peter Holkers and Jacques Muiyser, those valuable discussions with you in progress meetings contribute a lot to the final exciting achievement in this project.

I would like to thank NUMECA International for the support on software licenses, detailed user guides and discussions.

The China Scholarship Council is specially acknowledged for the financial support of this research.

Manys thanks to my committee members for reviewing my work and offering suggestions.

Many thanks to the staff of EFD and TFE at the University of Twente for offering help in these years. In particular, thanks to Wouter for your kind help with software and cluster issues, thanks to group secretaries Brenda, Susan, Sylvia and Sally for your help in many work-related aspects. These make working atmosphere in our group excellent .

I would like to thank Chaofa Zhao and Hao Shi in particular, you guide me a lot in good manner of scientific research and show good researcher examples to the young PhD candidates. As best friends, I really enjoy talking, discussing and drinking with you.

I would like to express my appreciation to my friends from TFE group. Marijn and Edmond, we encouraged each other to overcome the challenges in daily work. Plenty warm hand-sketches have been drawn by you Edmond, thanks very much. It is great to experience happy work time with my office mate, Shubham, Keerthi and Umair, please always ask yourself “How is life". Together with Timm, Sara, Harsha, Balan and Alireza, thank you all for sharing nice snacks and coffee, I enjoy the happy party time with you, hope everything good in your future. Let’s GanBei or surely PengBei!

I would like to thank Rui Yang for guiding me through the beginning of learning MATLAB. My special thanks are offered to my Chinese friends met here, Binbin, Dameng, Hao, Juan, Kun, Long, Mada, Minsi, Shiyu, Tao, Quanliang, Yan and Ye. Your appearance make life in the Netherlands joyful. For the following names, Panfei, Peipei, Ruosha, Weiqiu, Zhen and Zhiguo, I would like to quote a dialogue in The Fast and the Furious 7, “I don’t have friends, I got family". I am so lucky to meet you here, we witness each other’s growth, all the pain and joy make it what we are today. I also want to thank all my friends who played basketball and badminton with me.

It is impossible to experience all of these without the unconditional support and care of my parents and relatives, I would like to express my deepest gratitude to them. My ideal has always been to be a better man than my father, hope I could achieve this in future.

感谢父母和亲人对我的关心支持与爱，让我可以自由地度过人生求学时光。此文与你们一同见证我的成长，共同为我的学生时代画上句号，感谢你们。

Jie Wang
Enschede, November 2021

Bouns Page! The hand-sketches from Edmond, hope these can encourage more PhD candidates.